RECONFIGURABLE INTEGRATED PHOTONIC CIRCUITS ON SILICON

A Dissertation
Presented to
The Academic Faculty

by

Payam Alipour

In Partial Fulfillment
of the Requirements for the Degree
Doctor of Philosophy in
Electrical and Computer Engineering

Georgia Institute of Technology
May 2014

RECONFIGURABLE
INTEGRATED PHOTONIC CIRCUITS
ON SILICON

Approved by:

Dr. Ali Adibi, Advisor
School of Electrical and Computer Engineering
Georgia Institute of Technology

Dr. Gee-Kung Chang
School of Electrical and Computer Engineering
Georgia Institute of Technology

Dr. John A. Buck
School of Electrical and Computer Engineering
Georgia Institute of Technology

Dr. Joseph W. Perry
School of Chemistry and Biochemistry
Georgia Institute of Technology

Dr. Stephen E. Ralph
School of Electrical and Computer Engineering
Georgia Institute of Technology

Date Approved: 12/5/2013

To my parents,

Farideh & Reza.

ACKNOWLEGMENTS

First and foremost, I would like to thank my advisor, Prof. Ali Adibi, for his support and guidance throughout my PhD years, and for giving me the chance to be a part of the Georgia Tech community.

I am indebted to Dr. Mohammad Soltani, Dr. Reza Eftekhar, Dr. Siva Yegnanarayanan, and Dr. Babak Momeni, from whom I learned a great deal during my time at the Photonics Research Group.

I would like to express my deepest gratitude to my dear friends, Dr. Ehsan Shah Hosseini and Dr. Amir Hossein Atabaki, for their mentorship and companionship over the past six years.

I would like to thank the committee members, Prof. Stephen Ralph, Prof. John Buck, Prof. Gee-Kung Chang, and Prof. Joseph Perry, for their kind efforts in reviewing the present dissertation, and for honoring me with their presence at my doctoral defense session.

I would also like to thank Dr. Qing Li, Dr. Maysam Chamanzar, Majid Sodagar, Farshid Ghasemi, Reza Pourabolghasem, Hesam Moradinejad, and the IEN staff, especially Devin Brown and Gary Spinner, for helping me through the various stages of the research presented in this dissertation.

Finally, I would like to acknowledge the love and support that I have always received from my parents, without which none of my professional achievements would have been possible. I hope that one day I will prove worthy of all the sacrifices that they have made for me.

TABLE OF CONTENTS

LIST OF TABLES

Page

LIST OF FIGURES

Page

SUMMARY

Integrated optics as a platform for signal processing offers significant benefits such as large bandwidth, low loss, and a potentially high degree of reconfigurability. Silicon (Si) has unique advantages as a material platform for integration, as well as properties such as a strong thermo-optic mechanism that allows for the realization of highly reconfigurable photonic systems. Chapter 1 is devoted to the discussion of these advantages, and Chapter 2 provides the theoretical background for the analysis of integrated Si-photonic devices. The thermo-optic property of Si, while proving extremely useful in facilitating reconfiguration, can turn into a nuisance when there is a need for thermally stable devices on the photonic chip. Chapter 3 presents a technique for resolving this issue without relying on a dynamic temperature stabilization process. Temperature-insensitive (or "athermal") Si microdisk resonators with low optical loss are realized by using a polymer overlayer whose thermo-optic property is opposite to that of Si, and TiO_2 is introduced as an alternative to polymer to deal with potential CMOS-compatibility issues. Chapter 4 demonstrates an ultra-compact, low-loss, fully reconfigurable, and high-finesse integrated photonic filter implemented on a Si chip, which can be used for RF-photonic as well as purely optical signal processing purposes. A novel, thermally reconfigurable reflection suppressor is presented in Chapter 5 for on-chip feedback elimination which can be critical for mitigating spurious interferences and protecting lasers from disturbance. Chapter 6 demonstrates a novel device for on-chip control of optical fiber polarization. Chapter 7 deals with select issues in the implementation of Si integrated photonic circuits. Chapter 8 concludes the dissertation.

CHAPTER 1

INTRODUCTION

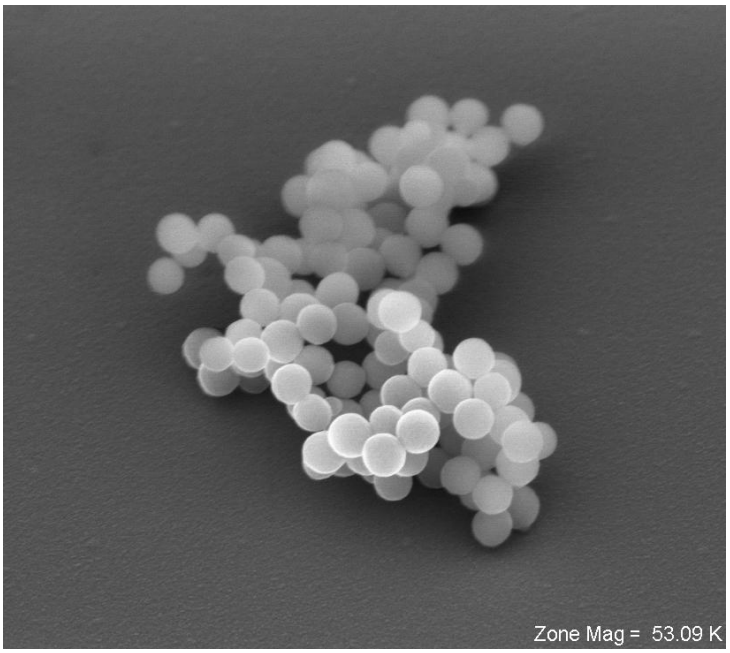

Figure 1.1. “Nano-grape” cluster. Each particle has an approximate diameter of 200 nm.

Digital information processing systems have come to occupy a central and growing role in many areas of modern life. These systems rely on fundamental electronic components to store and process the information, as well as interconnects to carry it from one place to another. Advances in the electronics technology have lead to an exponential decrease in the component feature size. Because of the inverse relation between the device capacitance and its size, this has resulted in the realization of an ever larger number of ever faster devices per chip, thus giving rise to what is commonly known as the “Moore's Law” [1]. However, a series of challenges collectively known as the “interconnect bottleneck” are preventing dense electrical interconnects from keeping pace with this trend, thereby limiting the bandwidth of the corresponding electronic signal

processors to several gigahertz. Among these problems are high and frequency-dependent loss, high latency, and high crosstalk through capacitive or inductive coupling [2]. With the growing demand for wideband systems coming from multiple sources (such as wireless communication and ranging), the development of an alternative platform is increasingly urgent.

With its large bandwidth resulting from high carrier frequency, low loss, and immunity to electromagnetic interference, photonics offers one such alternative [2,3]. In addition, the potentially high degree of tunability achievable in photonics makes it an especially attractive platform for implementing highly flexible front-ends such as those needed in signal processing [3]. Optical fibers have already replaced other media in long-haul data transmission; however, in order to keep their competitive edge in smaller scales and new functionalities, photonic systems have to rely on the benefits of integration. As with all other platforms, integration is a key step in reducing implementation costs and increasing system reliability. These integrated systems will take the form of planar lightwave circuits (PLCs): a configuration that allows for their fabrication using the readily available and mature microfabrication processes based on lithography and plasma etching. Several different material platforms have been proposed for this purpose; they can be broadly divided into low-index-contrast (LIC) and high-index-contrast (HIC) categories, with silica (SiO_2) and polymer being examples of the former, while silicon-on-insulator (SOI), silicon nitride (SiN), and III-V materials such as indium phosphide (InP) are examples of the latter [4–8].

HIC devices have tighter light confinement and therefore can have smaller bend radii, which means they can be fabricated with higher densities of integration. However,

higher index contrast also results in higher sensitivity to device dimensions and fabrication imperfections such as sidewall roughness [9]. With ongoing advances in lithography resolution and etching quality resulting in better dimension control [10] and smoother sidewalls [11–13], the trend is increasingly in favor of HIC devices.

The greatest advantage of III-V materials is their direct-bandgap property that enables efficient light generation and amplification. However, this comes with the downside of high costs. In contrast, silicon (Si), despite being an indirect-bandgap material, is a highly attractive option because of its extremely low cost, as well as compatibility with the highly developed CMOS process used in microelectronics, an advantage that allows for the direct integration of electronic and photonic devices on a single chip. Si can be used to implement the backbone of the photonic circuit, while III-V devices performing light generation and amplification can be integrated onto the Si substrate in selected locations using flip-chip bonding [14].

Another important property of Si is the existence of multiple physical mechanisms for manipulating its refractive index, which can be exploited for implementing tunable phase shifters used for the purpose of reconfiguring Si-based photonic devices and systems. This gives Si a tremendous advantage over SiN (another low-cost, CMOS-compatible material) in applications where flexibility and reconfigurability are important. The strongest available mechanisms are the free-carrier-plasma dispersion ($\Delta n = \pm\ 2.1\times10^{-3}$ for a depletion/injection of 10^{18} carriers per cm^3 at the 1550 nm wavelength [15]) and the thermo-optic effect ($dn/dT = +1.8\times10^{-4}$ /°C at 1550 nm [16]). Reconfiguration using free-carrier injection/depletion has the advantage of high speed (typical response time < 1 ns) which makes it especially suitable for ultrafast

modulation [17,18] and switching [19]. However, this comes at the expense of a high and phase-dependent insertion loss (> 1 dB per π phase shift) caused by free-carrier absorption [20], which limits the maximum tuning range of the photonic device. If the final output of the photonic system is to be converted to an electrical signal using a photodetector, the relation between the electrical loss and the optical loss will be quadratic, thereby doubling the importance of optical loss.

On the other hand, thermo-optic effect, while not being as fast as the free-carrier effect, is inherently lossless. Successful efforts have been made to reduce the response time of this method from several μs to less than 100 ns [21]. Since high speed is a key requirement for high-bandwidth modulators, free-carrier-based methods still have a clear advantage in implementing those devices. However, thermal tuning is a more suitable option for cases where the desired reconfiguration speed is not too high, especially when the number of reconfigurable elements is large enough to make the cumulative insertion loss of free-carrier-based phase shifters intolerable. Both mechanisms can be employed simultaneously on a single chip, in a manner that will result in the best trade-off between speed and signal strength for the overall system.

The above-mentioned factors have resulted in an explosion of research in the field of Si photonics over the past decade. With the demonstration of continuous-wave (CW) lasing [14,22], high-performance optical modulators [17,18], and optical detectors [23], the entire Si-photonic component toolbox is now available. Using such a toolbox, several academic and industrial groups are pursuing the development of Si-based optical interconnects [24,25] and signal processing systems [3].

Chapter 2 of this dissertation provides the theoretical background for the analysis of integrated Si waveguides, microresonators, and their interactions.

The thermo-optic property of Si, while proving extremely useful in facilitating reconfiguration, can turn into a burden when there are devices in the photonic system whose properties need to be stable with temperature. Unwanted variations in temperature can be caused by the surrounding environment, as well as on-chip sources such as electronic power dissipation or crosstalk from reconfigurable optical elements. Chapter 3 presents a method to resolve this issue without having to rely on a dynamic temperature stabilization system. Temperature-insensitive (or "athermal") microdisk resonators on SOI with low optical loss are experimentally realized by using a polymer overlayer whose thermo-optic property is opposite to that of Si [26]. The possibility of using titanium dioxide instead of polymer in order to realize CMOS-compatible athermal microresonators is also investigated in this chapter.

Chapter 4 demonstrates an ultra-compact and fully reconfigurable integrated photonic filter implemented on SOI [27], which can be used for both RF-photonic and purely optical signal processing purposes. This was the first demonstration of such filters using ultra-low-loss and compact Si microdisk resonators.

Elimination of unwanted feedback can be a necessary function in optical networks for various reasons. This function has traditionally been performed by optical isolators. However, the realization of on-chip isolators has been a challenge. Chapter 5 demonstrates a thermally reconfigurable, on-chip reflection suppressor on SOI without reliance on non-reciprocal mechanisms such as magneto-optics or nonlinear optics. This device is not a true optical isolator in the sense of showing complete unidirectional

transmission; however, in applications that require a high level of reflection suppression and/or low loss, with limited bandwidth and limited variability of reflection, it has a better performance compared to the existing alternatives.

Chapter 6 demonstrates a novel integrated fiber-polarization controller on SOI that is based on a fully reconfigurable 2×2 cell used in conjunction with a pair of two-dimensional grating couplers at the input/output for polarization splitting/combining. This device can be used for the compensation of polarization rotation in fibers for polarization-mode multiplexing systems, as well as on-chip ellipsometry solutions.

In Chapter 7, we present solutions to several practical challenges that are faced in the implementation of SOI PLCs. These challenges are the prevention of undesired polarization-mode mixing, quality-factor improvement, and the reduction of coupling loss. Each of these topics will be discussed in a separate section.

Finally, Chapter 8 presents the conclusion and lays out the potentials for future research in this area.

CHAPTER 2

THEORETICAL BACKGROUND

In this chapter, we discuss the fundamentals of electromagnetic modal analysis as it applies to the basic building blocks of integrated photonic circuits (i.e., waveguides and resonators). In addition, coupled-mode theory is introduced as a basic tool for the analysis of the interactions between those components.

2.1. Electromagnetic Modal Analysis

The main building blocks of the many photonic circuits are waveguides and resonators. The modes of these devices, which are the solutions to the wave propagation equation, are of great importance as the energy propagating in any particular mode of these devices remains in the same mode in the absence of perturbation.

The propagation of electromagnetic waves is governed by Maxwell's equations. Maxwell's curl equations for fields with the harmonic time dependence exp($j\omega t$) inside a non-magnetic medium are expressed as

$$\nabla \times \mathbf{H} = j\omega\varepsilon_0 \mathbf{E} + j\omega \mathbf{P}, \tag{2.1}$$

and

$$\nabla \times \mathbf{E} = -j\omega\mu_0 \mathbf{H}, \tag{2.2}$$

where ε_0 and μ_0 are, respectively, the permittivity and permeability of the vacuum, and **E**, **H**, and **P** represent the electric, magnetic, and polarization fields, respectively. The polarization field inside a linear material is given by

$$\mathbf{P} = \varepsilon_0 \left(n^2 - 1\right) \mathbf{E}, \tag{2.3}$$

where n is the refractive index of the material. Combining Equations (2.1), (2.2), and (2.3) yields the following Helmholtz equations that govern the propagation of electric and magnetic fields:

$$\nabla \times \nabla \times \mathbf{E} = \left(\frac{\omega}{c}\right)^2 n^2 \mathbf{E}, \tag{2.4}$$

and

$$\nabla \times \left(\frac{1}{n^2} \nabla \times \mathbf{H}\right) = \left(\frac{\omega}{c}\right)^2 \mathbf{H}, \tag{2.5}$$

where $c = (\varepsilon_0 \mu_0)^{-1/2}$ is the speed of light in the vacuum. Modes of different structures can be obtained by solving Equations (2.4) and (2.5) with the appropriate boundary conditions.

2.1.1. Modal Analysis of Optical Waveguides

The most basic structure in integrated optics is the waveguide. Different types of waveguides have been used in different integrated optical platforms. In Si photonics, rib and ridge waveguides (schematically shown in Figures 2.1(a) and 2.1(b), respectively) are the two most commonly used due to their ease of fabrication.

Because of the translational symmetry of the waveguide in the z direction (normal to the cross-sectional plane shown in Figures 2.1(a) and 2.1(b)), the electric and magnetic fields can be assumed to have an $\exp(-j\beta z)$ dependence on z, as in

$$\mathbf{E} = \tilde{\mathbf{E}}(x, y)\exp(-j\beta z), \tag{2.6}$$

and

$$\mathbf{H} = \tilde{\mathbf{H}}(x, y)\exp(-j\beta z), \tag{2.7}$$

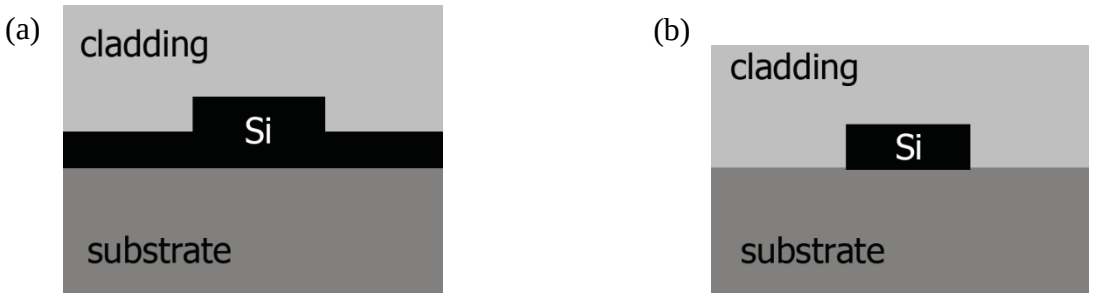

Figure 2.1. Cross-sectional schematics of (a) rib, and (b) ridge waveguides on SOI platform. The substrate is SiO_2 and is commonly called the buried oxide (BOX) layer. The Si part is typically referred to as "the core."

where β is the propagation constant of the mode in the z direction, while $\tilde{\mathbf{E}}$ and $\tilde{\mathbf{H}}$ are the cross-sectional profiles of the electric and magnetic fields in the x-y plane, respectively. Plugging Equation (2.7) into Equation (2.5) (or Equation (2.6) into Equation (2.4), alternatively) yields the wave propagation equation for the waveguide. In order for this equation to have any non-trivial non-zero solution, the eigenvalue problem needs to be solved, which will in turn determine the allowable values for β. Each β will correspond to a distinct eigenmode mode of the structure. For the numerical solution of the eigenvalue problem, we rely on the finite-element method (FEM) using the PDE module of the COMSOL software package. Figures 2.2(a) and 2.2(b) show the profile of the Poynting vector in the direction of propagation for the first two fundamental modes of a typical SiO_2-clad SOI ridge waveguide with a height of 220 nm and a width of 450 nm. These modes are found using the above-mentioned FEM mode solver.

The effective index, N_{eff}, of an eigenmode is defined as

$$N_{eff} = \frac{\beta}{k_0}, \tag{2.8}$$

where $k_0 = 2\pi/\lambda$ is the free-space wavenumber. For guided modes, the effective index is always below the refractive index of the core material, and above that of the cladding or

the substrate material, whichever is greater [28]. A larger effective index corresponds to a mode with a higher confinement in the core region. Conversely, the lower the confinement of a mode is, the smaller its effective index will be, pushing it closer to the "cut-off" condition [28]. The imaginary part of N_{eff}, if existent, is indicative of propagation loss. The effective indices of the modes in Figures 2.2(a) and 2.2(b) are 2.35 and 1.74, respectively. It is evident that the TM mode, which has the smaller effective index, has more of its power propagating through the substrate and the cladding, and therefore, is less confined to the waveguide core.

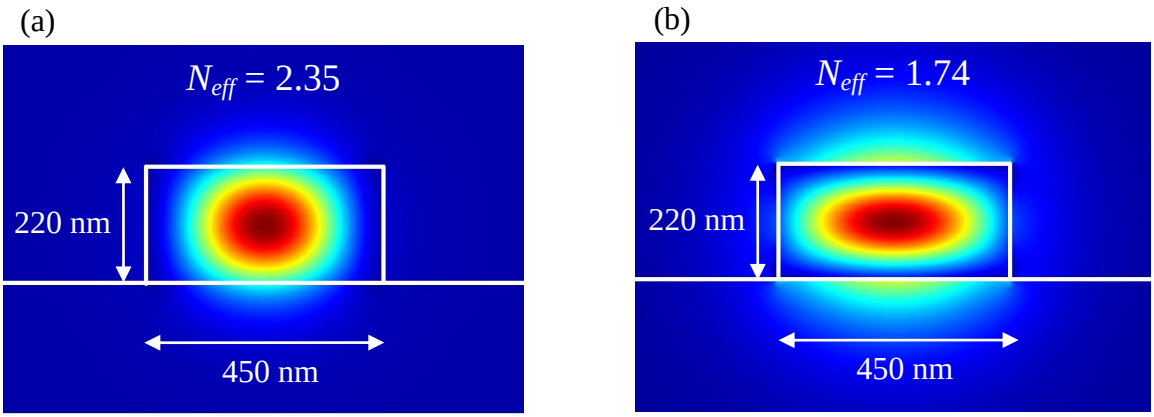

Figure 2.2. Profiles of the Poynting vector in the direction of propagation for the (a) fundamental TE, and (b) fundamental TM modes of an SiO_2-clad SOI ridge waveguide. The width and the height of the waveguide are 450 nm and 220 nm, respectively.

The relative power in each of the field components of these modes determines the polarization type of the mode. For example, the energy of the E_x component (i.e., the component perpendicular to the propagation direction and parallel to the substrate) of the mode shown in Figure 2.2(a) is almost three times larger than that of its E_z component, meaning that the electric field of this mode mainly lies in the *x*-*y* plane. Thus, the mode resembles a transverse electric (TE) mode, and is therefore called "TE-like." Similarly, it can be shown that the mode in Figure 2.2 (b) is "TM-like." From this point forward, we will refer to the TE-like and TM-like modes as simply TE and TM, respectively.

The higher-order modes of this waveguide are leaky, which makes the waveguide single-mode (There is one TE mode and one TM mode, but by appropriate excitation, it is possible to excite only one of these modes at a time, hence giving rise to single-mode operation.). As the dimensions of the waveguide are increased beyond single-mode operation, more and more modes become guided. Single-mode waveguides are generally preferred to multimode ones, as the presence of multiple modes can unnecessarily complicate the operation of the device.

Because Si is transparent for $\lambda > 1.1$ μm (which includes the optical communication wavelength $\lambda = 1.55$ μm), waveguide modes do not suffer from material absorption loss. In practice, however, fabrication imperfections result in the presence of roughness on the sidewalls of these waveguides, which causes the optical power to couple from the guided mode into radiation modes, and therefore, the waveguide becomes lossy [9] (In the ray tracing picture, this phenomenon can be viewed as local violations of the total internal reflection condition, which result in the leakage of power into the surrounding medium.). Figure 2.3(a) shows a 3D schematic of a waveguide with sidewall roughness. The roughness that results from fabrication imperfections typically does not show a significant variation in the *y* direction, and therefore, can be analyzed as a function $f(z)$ (see Figure 2.3(b)) with the proper statistical distribution, as done in Ref. [9]. Figure 2.3(c) is a scanning electron microscope (SEM) image of a fabricated device sidewall, which confirms the above-discussed nature of the roughness. With our present fabrication capabilities, sidewall roughness scattering results in a propagation loss of ~ 5 dB/cm at $\lambda = 1.55$ μm for a 450×220 nm^2 SOI ridge waveguide.

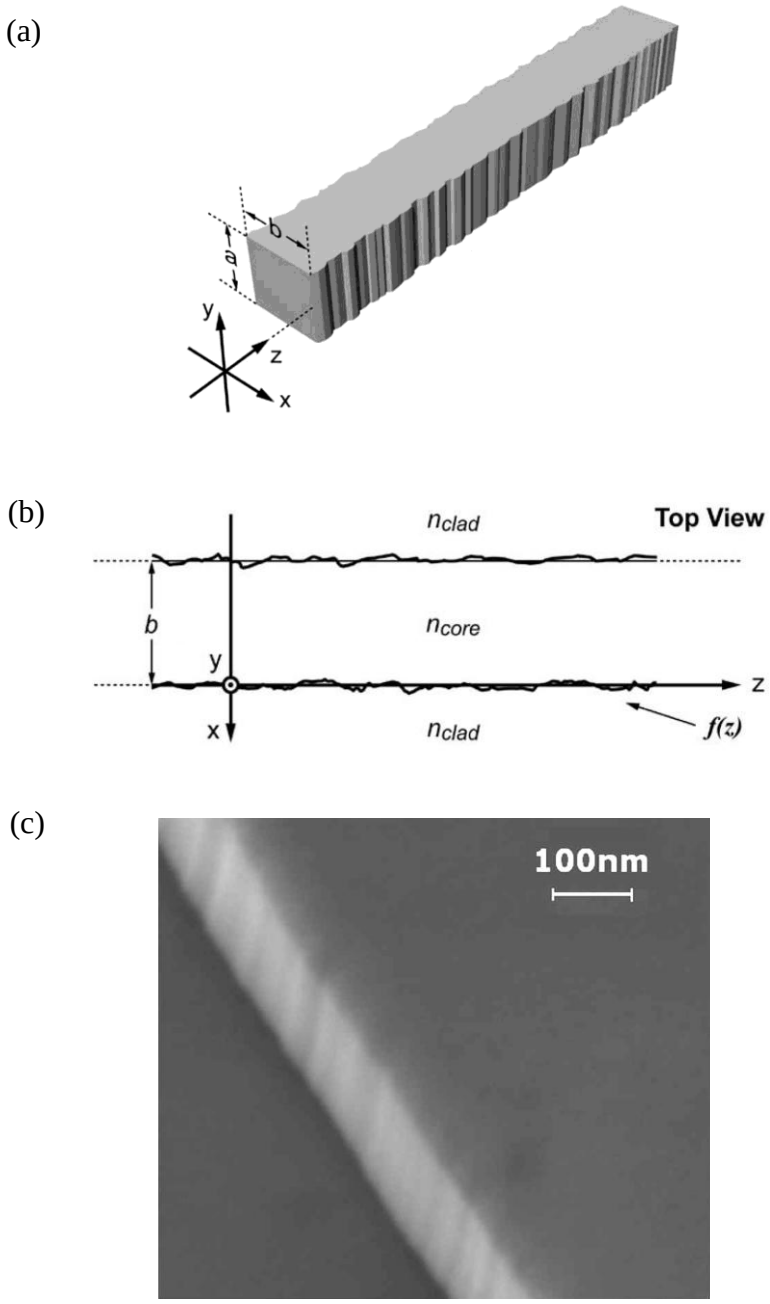

Figure 2.3. (a) 3D schematic of a waveguide with sidewall roughness [9]. (b) Top-view schematic of the waveguide in (a). The roughness can be analyzed as a function *f*(*z*) with a certain statistical distribution [9]. (c) SEM image of a fabricated device sidewall, which confirms the above-discussed nature of the roughness.

2.1.2. Modal Analysis of Optical Resonators

Optical resonators are structures that can trap and localize optical energy in a wavelength-selective fashion. The localization effect results in an enhancement of the optical field, which leads to stronger light-matter interaction achievable with smaller device footprints. These qualities enable numerous integrated optics applications, such as filters, spectrometers, low-power-tunable devices in general, efficient nonlinear processes, and compact sensors with high sensitivity.

Resonators can be broadly classified into traveling-wave and standing-wave categories. In traveling-wave resonators (TWRs), optical field travels around the resonator in one direction. If the field interferes constructively with itself after one roundtrip, the resonance condition is satisfied and energy build-up becomes possible. In standing-wave resonators (SWRs), on the other hand, two fields propagate in the opposite direction to each other, and their superposition generates a standing wave inside the resonator. Throughout this thesis, we will confine the discussion to TWRs only.

Figure 2.4 shows some commonly used types of TWRs. Microring and racetrack resonators (shown in Figures 2.4(a–d)) are basically waveguides that are looped in the form of a ring or a racetrack. The racetrack design is typically used if there is need for a long coupling region between the microresonator and a straight waveguide. If the bending radii of these two resonator types are not too small, they can be analyzed by studying their corresponding waveguides (For Si-based resonators at λ = 1.55 μm, the effect of bending is negligible for radii larger than 3 μm.). If the total length of the resonator is L, and the effective index of its corresponding waveguide is N_{eff}, the resonance condition can be written as

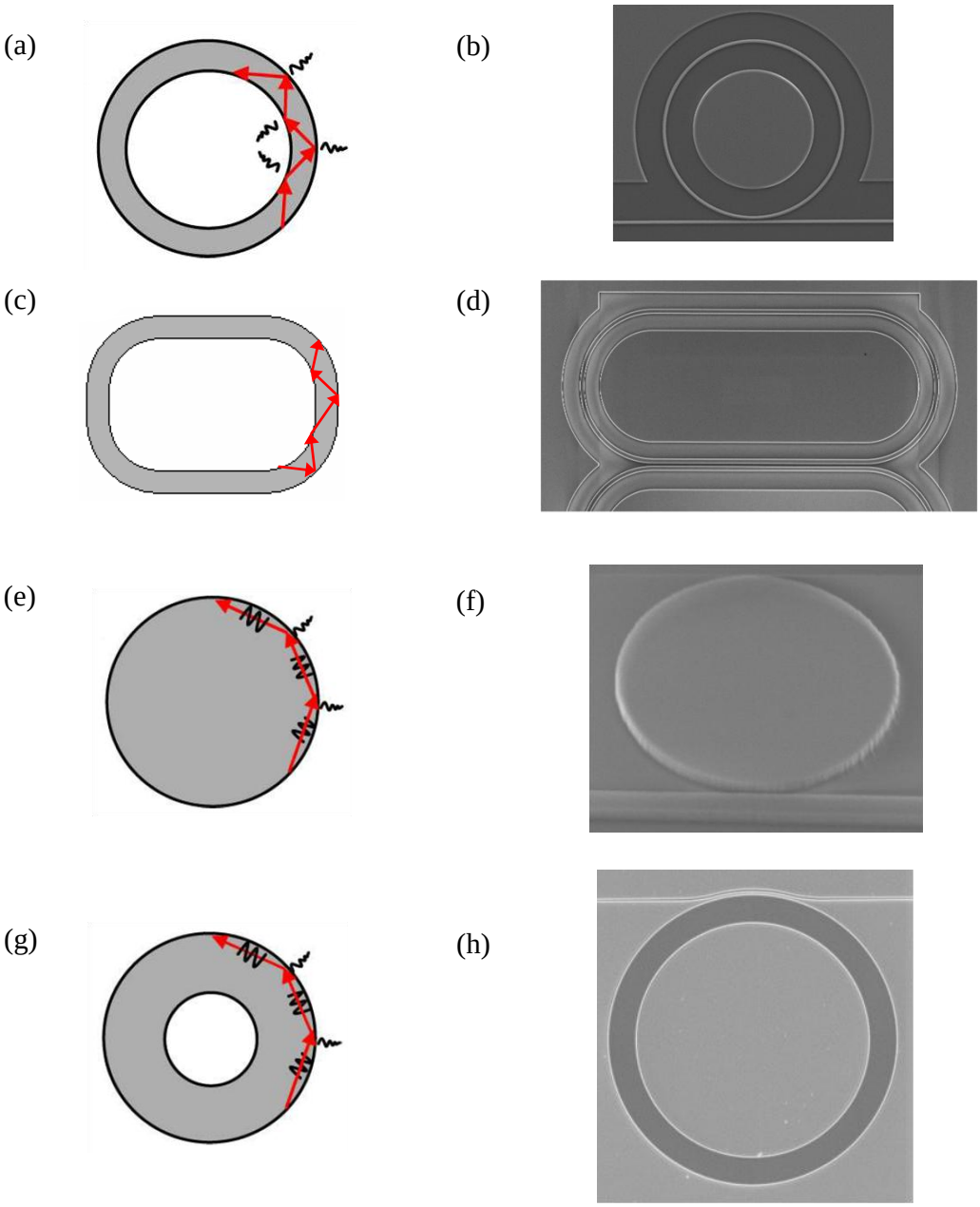

Figure 2.4. (a) Ray-tracing schematic, and (b) SEM image of a microring resonator. (c) Ray-tracing schematic, and (d) SEM image of a racetrack microresonator. (e) Ray-tracing schematic, and (f) SEM image of a microdisk resonator. (g) Ray-tracing schematic, and (h) SEM image of a microdonut resonator. The width of the microdonut in (h) is 4 μm.

$$k_0 N_{eff} L = 2m\pi \Leftrightarrow m\frac{\lambda}{N_{eff}} = L, \tag{2.9}$$

where m is the azimuthal mode number. Two modes with consecutive m-numbers are therefore separated by a fixed interval in frequency ($f = \omega/2\pi$) known as the free spectral range (FSR), which is given by

$$\text{FSR} = \frac{c}{N_g L}, \tag{2.10}$$

where N_g is the group index of the waveguide and is derived by

$$N_g = N_{eff} - \lambda\frac{\partial N_{eff}}{\partial \lambda}. \tag{2.11}$$

Microdisk resonators (shown in Figures 2.4(e) and (f)) are different from microrings and racetracks for the reason that the resonant mode interacts with only one sidewall, and therefore cannot be analyzed as a waveguide mode. Such resonators are commonly referred to as "whispering-gallery mode" (WGM) resonators. The WGM effect is present as long as the inner edge of the resonator is far enough not to be "felt" by the optical mode; such wide rings (seen in Figures 2.4(g) and (h)) are called microdonut resonators, and their basic physics are similar to microdisks. Since in practice, the most important source of optical loss is usually scattering from rough sidewalls, it follows that other things being equal, microdisk and microdonut resonators will be less lossy than microring and racetrack resonators.

In order to study the modes of WGM resonators (as well as microrings with small radii), the Helmholtz equations should be solved directly. As microrings, microdisks, and microdonuts all have cylindrical symmetry, the azimuthal dependence of their electromagnetic fields will take the form of $\exp(-jm\phi)$ as in

$$\mathbf{E} = \tilde{\mathbf{E}}(r, z)\exp(-jm\phi), \tag{2.12}$$

and

$$\mathbf{H} = \tilde{\mathbf{H}}(r, z)\exp(-jm\phi), \tag{2.13}$$

where the *r*, *z*, and ϕ are the standard cylindrical coordinates shown in Figure 2.5(a). By substituting the above equations into Equations (2.4) and (2.5), the eigenmode equations for a resonator with cylindrical symmetry are obtained, which can be solved numerically using the PDE module of the COMSOL software package. It must be noted that in the case of the simulation tool for the waveguide, the frequency was given as an input, and the output of the simulation was β, along with the corresponding eigenmode. However, the resonance frequencies of a resonator are not known a priori; therefore, the m-number is selected as an input, and the eigenmodes and their respective frequencies are then derived. Figures 2.5(b) and (c) respectively show the cross-sectional profiles of H_z and the Poynting vector for the fundamental TE mode of a 10-μm-radius, 220-nm-thick, air-clad microdisk, derived using COMSOL. Figures 2.5(d) and (e) show the same parameters for the 2nd-order TE mode. It can be seen that the higher-order modes move away from the sidewall and toward the center. The m-number for both modes is 105, but the resonance wavelength for the 2nd-order mode is smaller than that of the fundamental mode (1.49 μm compared to 1.56 μm). This can be interpreted as a shorter optical path length for the higher-order mode, which can be attributed to a smaller effective index, a smaller effective radius, or both (see Equation (2.9)). In either case, the result is lower confinement and higher radiation loss for the higher-order mode. Another result is larger FSRs for higher-order modes around the same resonance frequency, which can be used to distinguish the different modes when the measurements exhibit a multi-mode signature.

One possible use for microdonut resonators is to limit the multimode nature of WGM resonators, which may complicate the design and operation of WGM-resonator-based devices. Figures 2.5(f) and (g) are snapshot views from the top showing H_z for the fundamental and 2nd-order TE modes of a microdisk with m = 28. It must be noted that because of the traveling-wave nature of the resonator, the locations of the peaks and valleys are not fixed; hence, these pictures are snapshots in time.

The quality factor (Q) of a resonator is defined as

$$Q = \omega_0 \frac{U_c}{P_{loss}} = \omega_0 \tau_{rt} \frac{U_c}{E_{loss}}, \tag{2.14}$$

where ω_0 is the resonance frequency, U_c is the energy stored in the resonator, P_{loss} is the power dissipated by the resonator, E_{loss} is the energy dissipated per roundtrip, and τ_{rt} is the roundtrip time. Q is basically an inverse measure of how lossy a resonator is. Other things being equal, microdisk and microdonut resonators will have higher Qs than microring and racetrack resonators.

Another important metric is the mode volume, which is a measure of how confined a resonator (or waveguide) mode is. It is defined as

$$V_m = \frac{\int \varepsilon(\mathbf{r})|\mathbf{E}(\mathbf{r})|^2 dV}{\max[\varepsilon(\mathbf{r})|\mathbf{E}(\mathbf{r})|^2]}, \tag{2.15}$$

with the volume integration performed over the entire space. In applications such as sensing and nonlinear optics, the highest possible Q/V_m is desired.

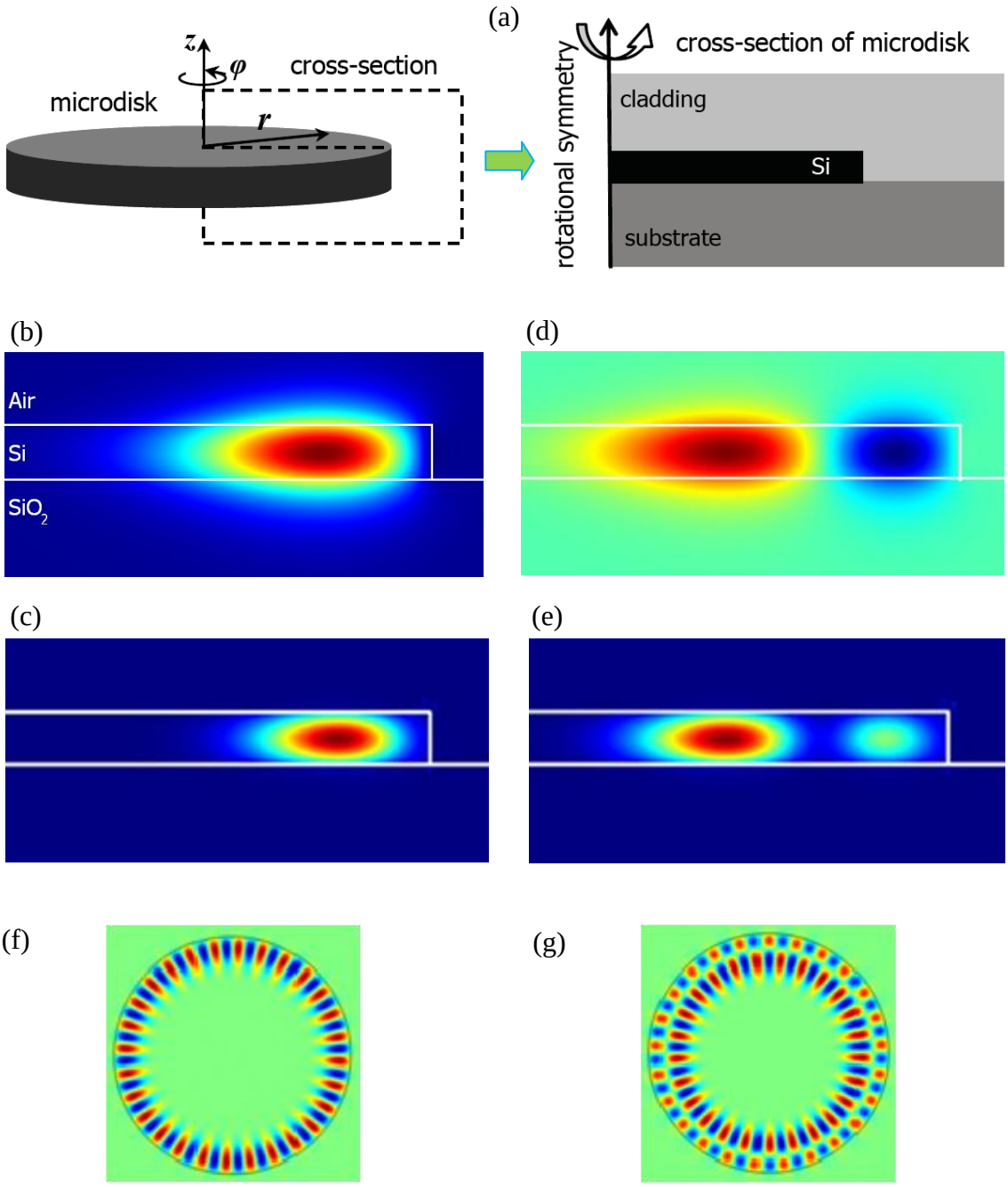

Figure 2.5. (a) Schematic of a microdisk resonator in cylindrical coordinates (left), along with its 2D cross section (right). Cross-sectional profiles of (b) H_z, and (c) the Poynting vector for the fundamental TE mode of a 10-μm-radius, 220-nm-thick, air-clad microdisk with m = 105 (λ = 1.56 μm). Cross-sectional profiles of (d) H_z, and (e) the Poynting vector for the 2nd-order TE mode of the same microdisk with m = 105 (λ = 1.49 μm). Snapshot views from the top showing H_z for the (f) fundamental, and (g) 2nd-order TE modes of a microdisk with m = 28.

2.2. Coupled-Mode Theory

The design of integrated photonic circuits usually involves the coupling of various components such as waveguides and resonators, which were individually analyzed in Subsections 2.1.1 and 2.1.2. In this section, we discuss the coupled-mode theory (CMT) as a simple tool for studying the interactions between these components.

Figure 2.6 shows a configuration in which a bus waveguide is brought into the proximity of a microdisk resonator. As the distance between them becomes smaller and smaller, each device "feels" the presence of the other, and they interact. The input and output fields in the waveguide are denoted by S_{in} and S_{out}, which are normalized such that $|S_{in}|^2$ and $|S_{out}|^2$ are the respective optical powers. The amplitude of the circulating field inside the resonator is denoted by a, which is normalized such that $|a|^2$ represents the resonator energy. Under 1st-oder approximation, the time-domain coupling of the waveguide and resonator fields in this structure can be described by

$$\frac{da}{dt} = \left(j\omega_0 - 1/\tau_0 - 1/\tau_c\right)a + \kappa S_{in}, \tag{2.16}$$

and

$$S_{out} = S_{in} - \kappa^* a, \tag{2.17}$$

where ω_0 is the resonance frequency, κ is the coupling coefficient between the waveguide and resonator modes, and $1/\tau_0$ and $1/\tau_c$ are field amplitude decay rates resulting from losses intrinsic to the resonator (such as material and scattering losses), and the loss resulting from coupling to the adjacent waveguide, respectively. It can be shown that

$$\tau_c = \frac{2}{|\kappa|^2}. \tag{2.18}$$

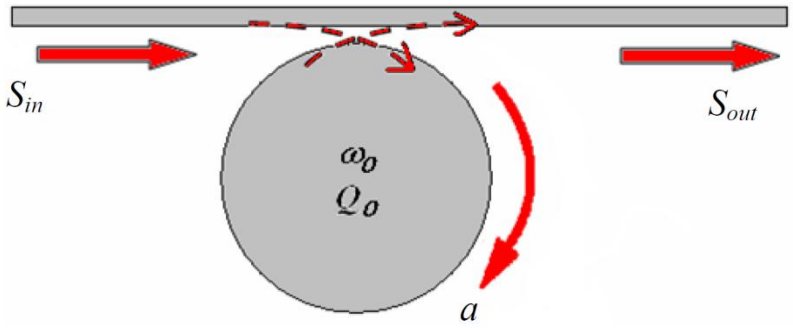

Figure 2.6. Schematic of a waveguide-resonator coupling.

The frequency dependence of field amplitudes is found by taking the Fourier transforms of Equations (2.16) and (2.17), which leads to

$$a(\omega) = \frac{\kappa S_{in}(\omega)}{j(\omega - \omega_0) + 1/\tau_0 + 1/\tau_c}, \tag{2.19}$$

and

$$T(\omega) = \frac{S_{out}(\omega)}{S_{in}(\omega)} = \frac{j(\omega - \omega_0) + 1/\tau_0 - 1/\tau_c}{j(\omega - \omega_0) + 1/\tau_0 + 1/\tau_c}, \tag{2.20}$$

where $T(\omega)$ is the waveguide transmission function. Also, it can be shown using Equation (2.14) that the intrinsic quality factor (Q_0) can be derived from

$$Q_0 = \frac{\omega_0 \tau_0}{2} \cong \frac{2\pi N_g}{\alpha \lambda_0}, \tag{2.21}$$

while the coupling (extrinsic) quality factor (Q_c) will be given by

$$Q_c = \frac{\omega_0 \tau_c}{2} = \frac{\omega_0}{|\kappa|^2}, \tag{2.22}$$

where α is the power propagation loss per unit length. $\tau_0/2$ and $\tau_c/2$ are respectively the intrinsic and extrinsic photon lifetimes inside the cavity. The approximation in Equation (2.21) holds for $\alpha L << 1$. It can be seen from Equation (2.22) that Q_c is an inverse

measure of the coupling strength between the waveguide and the resonator. By combining Equations (2.20) through (2.22), waveguide transmission can be rewritten as

$$T(\omega) = \frac{j\,2(\omega - \omega_0)/\omega_0 + 1/Q_0 - 1/Q_c}{j\,2(\omega - \omega_0)/\omega_0 + 1/Q_0 + 1/Q_c}, \tag{2.23}$$

which means that power transmission at the center of resonance ($\omega = \omega_0$) will be given by

$$\left|T(\omega_0)\right|^2 = \left|\frac{Q_c - Q_0}{Q_c + Q_0}\right|^2 = \left|\frac{1 - Q_0/Q_c}{1 + Q_0/Q_c}\right|^2, \tag{2.24}$$

which depends only on the relative ratio of Q_c and Q_0.

There are three possible coupling regimes in the waveguide-resonator structure: (1) critical coupling, under which $Q_c = Q_0$; (2) over-coupling, for which coupling is stronger than the critical coupling $Q_c < Q_0$; and (3) under-coupling, in which coupling is weaker than the critical coupling $Q_c > Q_0$. The transmission amplitude and phase for each of these cases are shown in Figure 2.7. Under critical coupling, power is fully transferred from the waveguide to the resonator. This is the only case in which a transmission zero is achieved. If the coupling is stronger (i.e., over-coupling), the power will be coupled back to the waveguide. In the extreme case that $Q_c << Q_0$, the transmission amplitude is almost constant and equal to unity, while the phase changes linearly with ω within the bandwidth of the resonator (as for $Q_0/Q_c = 10$ shown in Figure 2.7). Such a structure is a equivalent to a constant time delay (within the resonator bandwidth), and therefore can be used to implement low-loss delay lines and all-pass filters, as will be done later in this thesis.

(a)

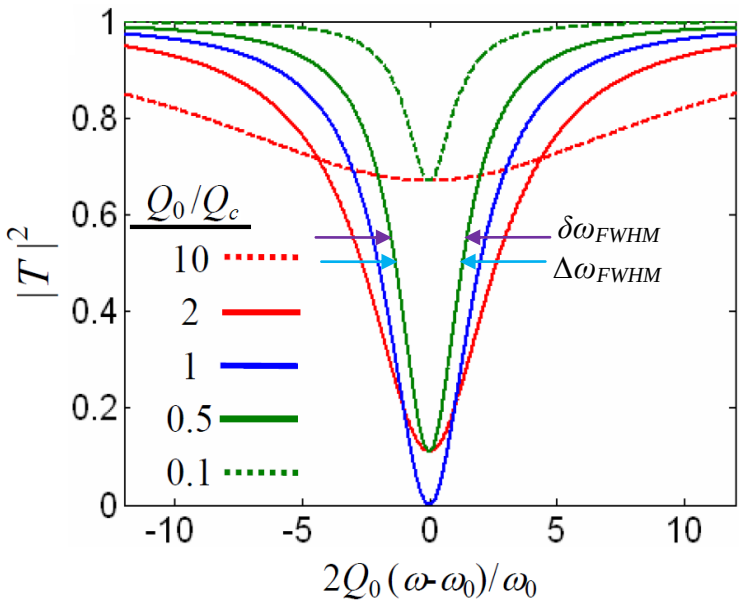

(b)

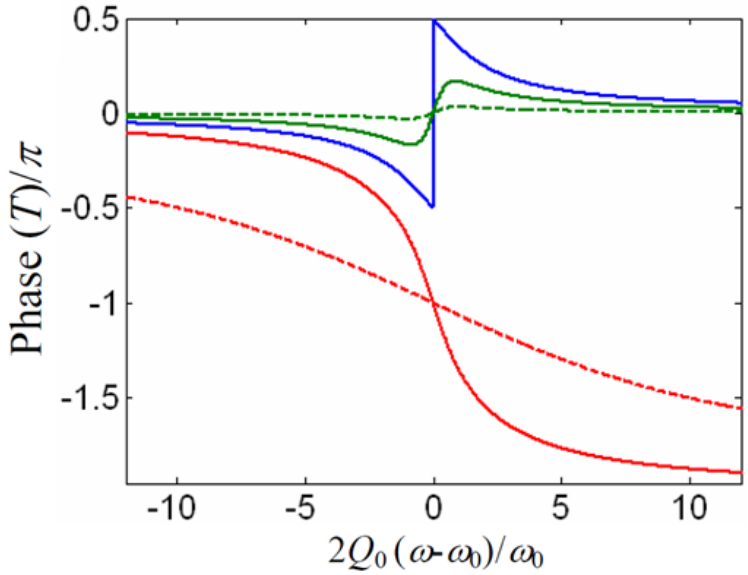

Figure 2.7. (a) Amplitude, and (b) phase characteristics of the waveguide transmission as a function of normalized frequency detuning under various resonator coupling regimes.

It can be shown using Equation (2.19) that the full-width half-maximum (FWHM) $\delta\omega$ of resonator energy (i.e., $|a(\omega)|^2$) around ω_0 is equal to $\omega_0(1/Q_0 + 1/Q_c)$. The term $(1/Q_0 + 1/Q_c)^{-1}$ is typically referred to as the "loaded quality factor" (Q_L). The following relation holds between these variables:

$$Q_L = \frac{1}{1/Q_0 + 1/Q_c} = \frac{\omega_0}{\delta\omega_{FWHM}} = \frac{\lambda_0}{\delta\lambda_{FWHM}}. \tag{2.25}$$

If the values of Q_L and $|T(\omega_0)|^2$ are known, Equations (2.24) and (2.25) will form a two-equation system with two unknowns (Q_0 and Q_c). By solving this system, the value of Q_0 can be calculated from

$$Q_0 = \frac{2Q_L}{1 \pm |T(\omega_0)|}. \tag{2.26}$$

with (+) used for under-coupling and (–) for over-coupling. However, it must be noted that the value of $\Delta\omega_{FWHM}$ for the easily measurable waveguide power transmission $|T(\omega)|^2$ (shown on Figure 2.7(a) for the $Q_0/Q_c = 0.5$ curve) is not equal to $\delta\omega_{FWHM}$ of resonator energy unless under critical coupling. If we define a new parameter named Q_{3dB} based on $\Delta\omega_{FWHM}$, it can be shown that

$$Q_{3dB} = \frac{\omega_0}{\Delta\omega_{FWHM}} = \frac{1}{\sqrt{(1/Q_0 + 1/Q_c)^2 - 2(1/Q_0 - 1/Q_c)^2}}, \tag{2.27}$$

and

$$Q_0 = \frac{2Q_{3dB}\sqrt{1 - 2|T(\omega_0)|^2}}{1 \pm |T(\omega_0)|}. \tag{2.28}$$

with (+) used for under-coupling and (–) for over-coupling. Figure 2.8 shows the Q_0/Q_{3dB} ratio as a function of the power transmission $|T(\omega)|^2$. This graph is easy to use with logarithmic plots, but it has a drawback in that it does not provide an answer for

extinctions smaller than 3dB. An alternative approach is based on the fact that the resonator $\delta\omega_{FWHM}$ is the frequency deviation (from ω_0) that gives us the middle points between the minimum of waveguide power transmission (i.e., $|T(\omega_0)|^2$) and its maximum (i.e., unity). For example, for the Q_0/Q_c = 0.5 curve in Figure 2.7(a), this would be the 0.55 transmission bandwidth instead of 0.5. After measuring the correct value of $\delta\omega_{FWHM}$, we can use it to calculate Q_L from Equation (2.25) and then use Equation (2.26) to find Q_0.

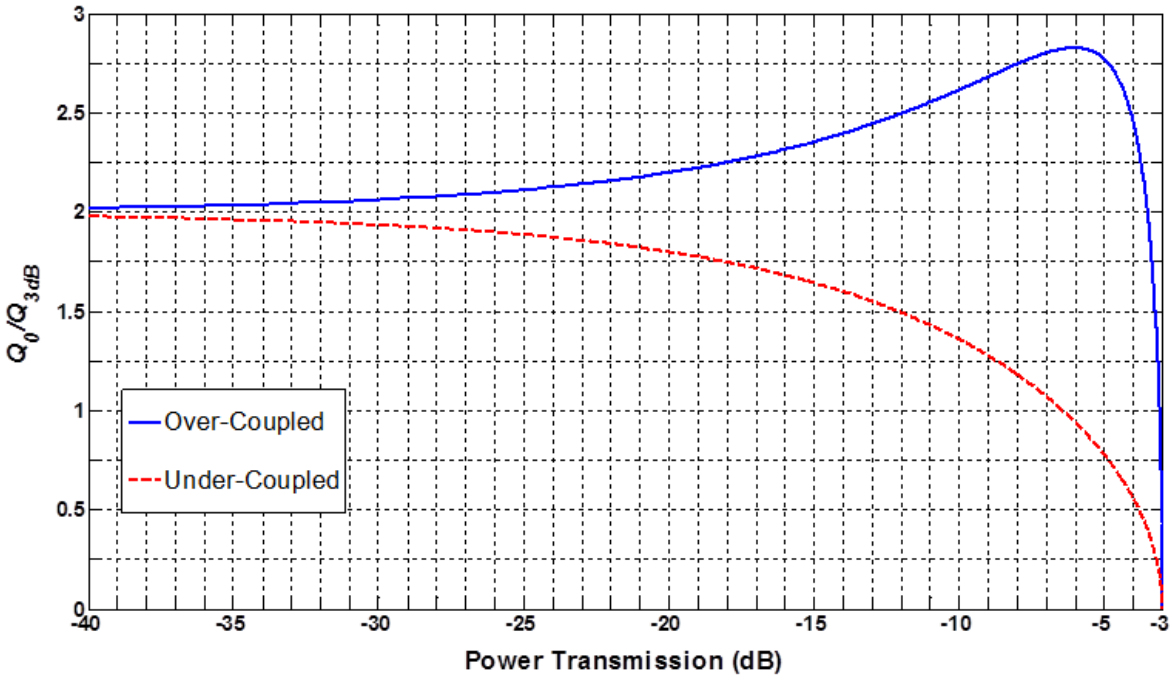

Figure 2.8. The ratio of Q_0/Q_{3dB} as a function of power transmission $|T(\omega)|^2$ in over-coupled and under-coupled regimes.

As mentioned earlier in this section, the intrinsic quality factor Q_0 is determined by losses intrinsic to the resonator, which generally include the radiation loss, the material absorption loss, the surface scattering loss, and the surface absorption loss [12]. A separate Q factor can be defined for each of these types of loss, with the following identity holding among them:

$$1/Q_0 = 1/Q_{rad} + 1/Q_m + 1/Q_{ss} + 1/Q_{sa}, \tag{2.29}$$

where Q_{rad}, Q_m, Q_{ss}, and Q_{sa} are the radiation, material absorption, surface scattering, and surface absorption Qs, respectively. Each of these Qs is an upper bound for the total Q_0. There is a straightforward method for direct calculation of Q_{rad} using the COMSOL mode solver. As mentioned in Subsection 2.1.2, resonance frequencies are the eigenvalue outputs of our resonator simulation tool in COMSOL. Similar to that of β (or N_{eff}), the imaginary part of the eigenfrequency is an indication of loss. It can be shown that in the absence of other sources of loss, this can be used to derive the value of Q_{rad} from

$$Q_{rad} = \frac{\omega_r}{2\omega_i}, \tag{2.30}$$

where ω_r and ω_i are the real and imaginary parts of the eigenfrequency in COMSOL, respectively.

CHAPTER 3

ATHERMAL MICRORESONATORS ON SOI PLATFORM

3.1. Introduction

TWRs on SOI platform are a key building block in Si photonics, owing to their high quality factors and small mode volumes, as well as mechanical stability and simple design. The most common planar TWR architectures were introduced in Figure 2.4. The highest intrinsic *Q*s are in the 10^6 range and exhibited by microdisk and microdonut resonators [12,29], which is typically one order of magnitude higher than those exhibited by microrings and racetracks [30]. One of the drawbacks of using Si-based resonators is their extreme sensitivity to temperature change, resulting from the strong dependence of Si refractive index on temperature. The thermo-optic coefficient (TOC) of Si, defined as dn/dT (with n and T being the refractive index and the temperature, respectively), is $+1.8\times10^{-4}$ /˚C. For the fundamental TE mode of a typical air-clad SOI microdisk with a radius of 10 μm and a Si thickness of 220 nm, the resulting thermo-optic resonance shift (TORS) is about +78 pm/˚C around the 1550 nm wavelength, which is equivalent to ~ 10 GHz/˚C. For an SOI microring with the same radius and a cross-section of 450×220 nm^2, the TE-mode TORS is about 75 pm/˚C at the same wavelength. This degree of thermal variation is not acceptable in many applications that rely on stable resonance properties, such as delay lines and narrow-band filters. Unwanted thermal shifts can be caused by fluctuations in the ambient temperature, as well as on-chip sources such as electronic power dissipation or crosstalk from thermally reconfigurable optical elements.

One solution to this problem is active thermal stabilization with feedback, using thermo-electric coolers (TECs), local microheaters [31], or both. However, this approach

adds to the complexity and the power consumption of the system. A passive alternative is to coat the resonator with a negative-TOC material in order to compensate the positive TOC of the core material and reduce the temperature sensitivity of the photonic device. To explore this possibility, we need to take a closer look at the origins of the thermo-optic effect.

There are two competing mechanisms that give rise to the thermo-optic effect [16]: (1) an increase in polarizability with temperature, which results in a higher refractive index (see Equation (2.3)); and (2) thermal expansion, which leads to a decrease in the number of dipoles per unit volume, and therefore, a decrease in the refractive index. These effects can be summarized in the following equation:

$$\frac{dn}{dT} = \left(\frac{\partial n}{\partial T}\right)_{\rho} + \left(\frac{\partial n}{\partial \rho}\right)_{T} = \left(\frac{\partial n}{\partial T}\right)_{\rho} - 3\rho\left(\frac{\partial n}{\partial \rho}\right)_{T} \alpha , \tag{3.1}$$

where α is the linear thermal expansion coefficient, and ρ is the material density. The first term describes the polarizability effect, while the second one describes the expansion effect. In inorganic materials, the thermo-optic effect is generally dominated by the first term, which leads to a positive TOC [16]. Polymers, on the other hand, have large thermal expansion coefficients (usually in the 10^{-4} range, compared to $\alpha_{Si} = 2.6\times10^{-6}$ /˚C/m) that generally result in large negative TOCs [32]. For this reason, polymers have been successfully employed to make athermal waveguides in silica (TOC $\cong$ 10^{-5} /˚C) [33]. As we will see later in this chapter, it is more challenging to achieve this result for Si-based devices because of their larger TOCs and higher mode confinements. The theoretical possibility of athermal Si-based waveguides and microring resonators was investigated in [34,35], and a resonance shift smaller than 5 pm/˚C was experimentally demonstrated in [36] using a polymer-clad 350-nm-wide microring with a 220-nm-thick

Si device layer. However, narrowing the microring causes a substantial reduction in resonator Q (Q_0 ~ 15,000 reported in Ref. [36]). In this chapter, after an introduction to the theory of athermal resonance, we first demonstrate an alternative device configuration based on polymer-clad microdisks to realize high-Q athermal resonators. Then, we use TiO_2, a rare negative-TOC inorganic material widely used in optics, as an alternative cladding material for athermalization, which can address the drawbacks of using polymers. Athermal TiO_2-clad microresonators are demonstrated in the end.

3.2. Theory of Athermal Resonance

By taking the temperature derivative of Equation (2.9) and taking into account the effect of wavelength dispersion, the temperature dependence of the resonance wavelength in a TWR can be expressed as:

$$m\frac{d\lambda}{dT} = N_{eff}\frac{dL}{dT} + L\frac{dN_{eff}}{dT} = N_{eff}\frac{dL}{dT} + L\frac{\partial N_{eff}}{\partial T} + L\frac{\partial N_{eff}}{\partial \lambda}\frac{d\lambda}{dT}, \tag{3.2}$$

where m is the azimuthal mode number, λ is the free-space resonance wavelength, N_{eff} is the effective refractive index seen by the resonant mode, and L is the resonator length. After substituting $m = LN_{eff}/\lambda$ from Equation (2.9), we have

$$\frac{d\lambda}{dT}\left(\frac{LN_{eff}}{\lambda} - L\frac{\partial N_{eff}}{\partial \lambda}\right) = N_{eff}\frac{dL}{dT} + L\frac{\partial N_{eff}}{\partial T}, \tag{3.3}$$

and then

$$\frac{d\lambda}{dT} = \frac{\lambda}{N_{eff} - \lambda\dfrac{\partial N_{eff}}{\partial \lambda}}\left(N_{eff}\frac{dL/dT}{L} + \frac{\partial N_{eff}}{\partial T}\right), \tag{3.4}$$

which reduces to

$$\frac{d\lambda}{dT} = \frac{\lambda}{N_g}\left(N_{eff}\alpha + \frac{\partial N_{eff}}{\partial T} \right) \cong \frac{\lambda}{N_g}\frac{\partial N_{eff}}{\partial T}, \tag{3.5}$$

where N_g is the group index and α is the linear thermal expansion coefficient of the resonator material [36]. For the approximation, we have neglected the effect of thermal expansion on the optical path length, since the $N_{eff}\alpha$ product for Si is two orders of magnitude smaller than its thermo-optic coefficient. Equation (3.5) means that athermal resonance can be achieved only with an athermal effective index. The temperature dependence of N_{eff} can be derived by using the perturbation method for the propagation constant [28]:

$$\frac{\partial N_{eff}}{\partial T} = \frac{c\varepsilon_0 \iint_{\infty} |\mathbf{E}|^2 \, dxdy}{2P}\left(\Gamma_{core} n_{core} \frac{dn_{core}}{dT} + \Gamma_{clad} n_{clad} \frac{dn_{clad}}{dT} + \Gamma_{sub} n_{sub} \frac{dn_{sub}}{dT} \right), \tag{3.6}$$

where P is the total circulating power, and Γ_A is the field overlap factor in region A defined as:

$$\Gamma_A = \iint_A |\mathbf{E}|^2 \, dxdy \Big/ \iint_{\infty} |\mathbf{E}|^2 \, dxdy, \tag{3.7}$$

and the subscripts A = *core*, *clad*, and *sub* refer to the core, the cladding, and the SiO_2 substrate, respectively. The integrations in Equations (3.6) and (3.7) are performed over the cross section of the device (i.e., the *x*-*y* plane with propagation being along the *z* direction). We have assumed that the overlap factors do not change with temperature, which makes the TORS a linear effect provided that the TOCs themselves are constant. However, this assumption is not fully accurate, since mode confinement varies as the indices of the core and its surroundings change in different ways. We will investigate this issue in more detail later. Another assumption we have made is the independence of TOCs from temperature, which is investigated in detail in Ref. [37].

Athermal performance is achieved when $\partial N_{eff}/\partial T$ is zero. When the TOC of the substrate is negligible, as it is with 10^{-5} /°C for SiO_2, the athermal condition following from Equations (3.5) and (3.6) is

$$\frac{dn_{clad}}{dT} \cong -\left(\frac{\Gamma_{core} n_{core}}{\Gamma_{clad} n_{clad}}\right)\frac{dn_{core}}{dT}. \tag{3.8}$$

3.3. High-*Q* Athermal Microdisk Resonators on SOI with Polymer Cladding

3.3.1. Design and Simulation

It can be seen from Equation (3.8) that achieving athermal performance in a device with a large positive core TOC (dn_{core}/dT) and/or a high mode confinement (i.e., large Γ_{core}, which also means a small Γ_{clad}) demands a cladding material with a large negative TOC (i.e., large dn_{clad}/dT) and/or a high index (n_{clad}). A high n_{clad} has a secondary advantage in that it helps reduce the mode confinement.

As mentioned earlier, polymers usually have large negative TOCs; on the other hand, they are generally low-index materials, with 1.3–1.7 being their typical refractive index range. Therefore, if polymers are to be used in this line of work, one must look for those with the largest possible TOCs without much concern for the refractive index. Polymers have a characteristic temperature known as the "glass transition temperature" (T_g), at which they undergo an abrupt transition from a glassy and brittle phase to a rubbery and elastic phase [32]. The magnitude of the TOC also experiences an abrupt increase at T_g, as shown in Figure 3.1. Since the TOC data may not be readily available for many polymers, it is advisable to look for a low T_g as a proxy for a large TOC [32].

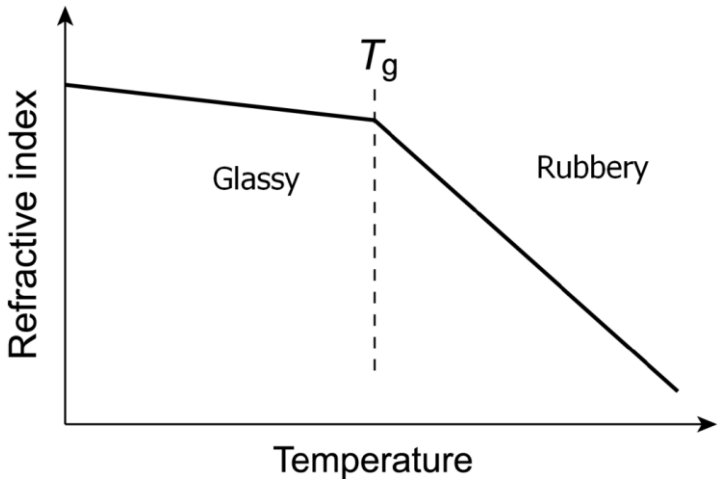

Figure 3.1. The general form of temperature dependence exhibited by the refractive indices of polymers [32].

In this work, we use an aliphatic polyester-based urethane diacrylate polymer (PUA) with a T_g of –37 ˚C, and a TOC of -4.5×10^{-4} /˚C, which is, to our knowledge, one of the largest TOCs among polymers. The refractive index of PUA is about 1.45 around the 1550 nm wavelength. We use the FEM mode solver provided in the COMSOL software package to analyze the temperature dependence of the resonance, and we assume the temperature to be uniform across the entire resonator device. Simulation shows that adding a PUA cladding to a 10-μm-radius and 220-nm-thick microdisk reduces its fundamental-TE-mode TORS only by about 15% (from 78.5 to 65.8 pm/˚C). As we will see later, this result is confirmed by experiment, and it means that, for the purpose of microdisk athermalization, using a large-TOC polymer is not adequate by itself.

It was mentioned earlier that Equation (3.6) involves an assumption regarding the constancy of field overlap factors, which is not fully accurate since mode confinement varies as the indices of the core and its surroundings change in different ways. The FEM mode solver provides a useful tool for the analysis of this 2nd-oder effect, as the field

profile is derived independently for each new index configuration resulting from temperature change. Figure 3.2 shows the successive shifts in the simulated resonance wavelength of a 10-µm-radius, 220-nm-thick air-clad microdisk, as the temperature is increased in consecutive steps of 10 ˚C each (totaling 100 ˚C). Theoretically, one can expect a slight increase in TORS with temperature, since mode confinement will increase with the rise in n_{core}, which is either not accompanied by comparable increases in n_{clad} or $n_{substrate}$, or amplified by a decrease in n_{clad} in the case of polymeric claddings. This is indeed the case according to simulation, which shows the TORS increasing from 78.47 to 78.48 pm/˚C. Curve-fitting results (also displayed in Figure 3.2) demonstrate that the linearity assumption is very accurate, and therefore, the 2nd-oder mode-confinement effect is practically negligible.

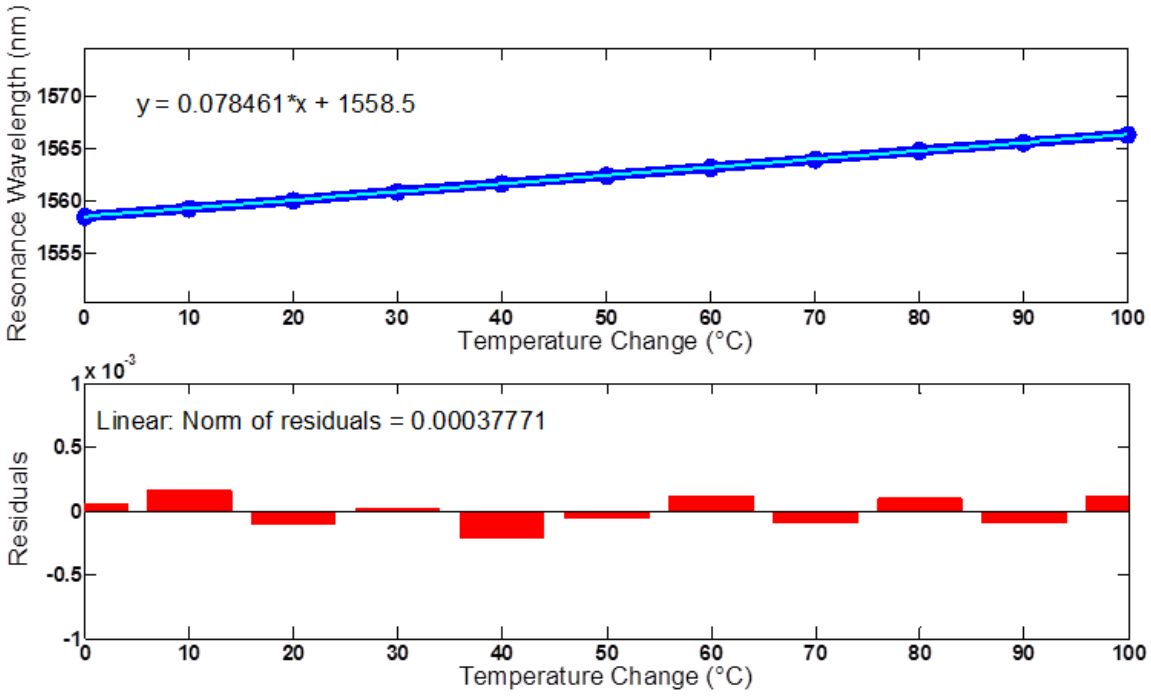

Figure 3.2. Top: Successive shifts in the simulated resonance wavelength of a 10-µm-radius, 220-nm-thick air-clad microdisk, as the temperature is increased in consecutive steps of 10 ˚C each (totaling 100 ˚C). Bottom: Curve-fitting results demonstrate the accuracy of the linearity assumption in Equation (3.6).

We concluded earlier that for the purpose of microdisk athermalization, using a large-TOC polymer is not adequate by itself. One solution to this problem is reducing the mode confinement in order to enhance the effect of the cladding. This can be achieved in several ways; one of them is to use the higher-order modes of the microdisk, which have lower confinement compared to the fundamental mode. In Figure 3.3, the value of TORS derived from simulation is plotted against the radial mode order for the first five modes of a PUA-clad, 10-μm-radius, 220-nm-thick microdisk. It must be noted that although different-order resonances in this simulation are all located around 1550 nm, they are generally not identical in wavelength, which gives rise to the irregularity seen in Figure 3.3. It can be observed that the gain from going to higher-order modes is quite small. Even for a mode order as high as m = 10, the TORS is still 60.6 pm/˚C. We conclude that changing the mode order is not an effective strategy for athermalization.

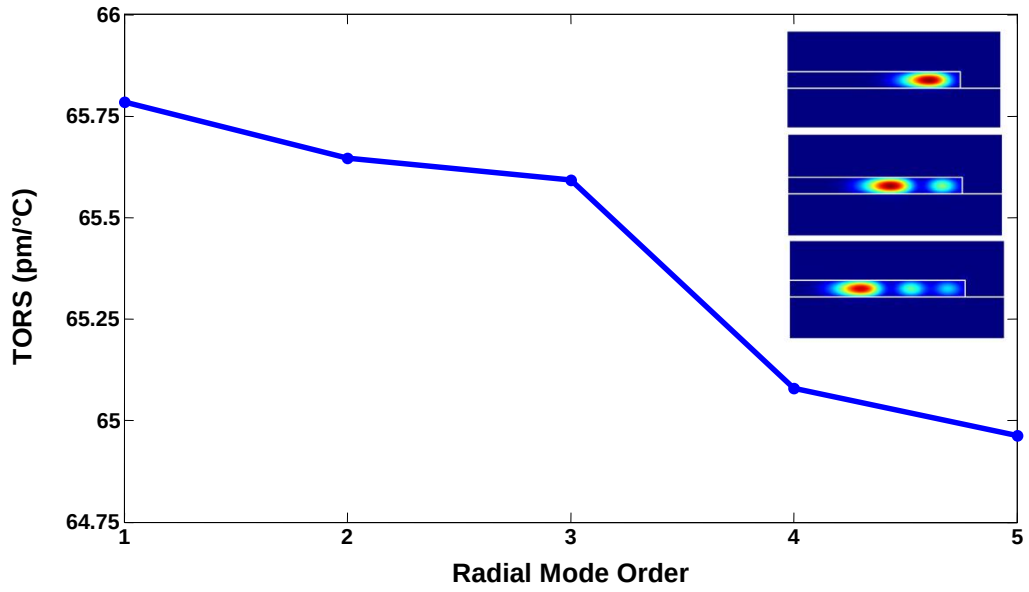

Figure 3.3. Simulation results for TORS plotted against the radial mode order for the first five modes of a PUA-clad, 10-μm-radius, 220-nm-thick microdisk. Inset shows the profiles of the three lowest-order modes.

Another way of reducing the mode confinement is through reducing the resonator size. For a microdisk resonator, this can be done by reducing the Si layer thickness and/or the resonator radius. For microring resonators, there is an extra degree of freedom usable by reducing the resonator width, as we will discuss later. It follows from equation (3.8) that with Si as the core and PUA as the cladding, the ratio $\Gamma_{core}/\Gamma_{clad}$ must equal 1.04 for athermal resonance to be realized. The TORS will be positive for larger ratios and negative for smaller ratios. Figures 3.4(a) and (b) respectively show the overlap factors Γ_{core} and Γ_{clad} as a function of Si thickness for three different resonator radii of 10, 5, and 2.5 μm. The data shown here are for the fundamental TE mode. The irregularities result from the fact that the corresponding resonance wavelengths are in general not identical. This effect is amplified with the increase in resonance FSR as the resonator radius is decreased.

Figure 3.5(a) shows the $\Gamma_{core}/\Gamma_{clad}$ ratio as a function of Si thickness for microdisk radii of 10, 5, and 2.5 μm. It can be seen that the athermal ratio 1.04 is achieved at thicknesses around 84.4, 90.7, and 118.25 nm, respectively, with radii of 10, 5, and 2.5 μm. Figure 3.5(b) is a similar graph that shows the simulated TORS value as the dependent variable. It can be seen that by reducing the resonator size, the TORS is also reduced. It is also clear that changing the Si layer thickness has a stronger effect on the TORS than changing the resonator radius. Zero TORS is achieved at thicknesses around 82.7, 90.6, and 114.2 nm, for resonator radii of 10, 5, and 2.5 μm, respectively. These results are very close to what is predicted by the athermal effective index theory. The slight deviations that existed are attributable to the neglected effect of the substrate TOC, 2^{nd}-order confinement effects, and interpolation errors.

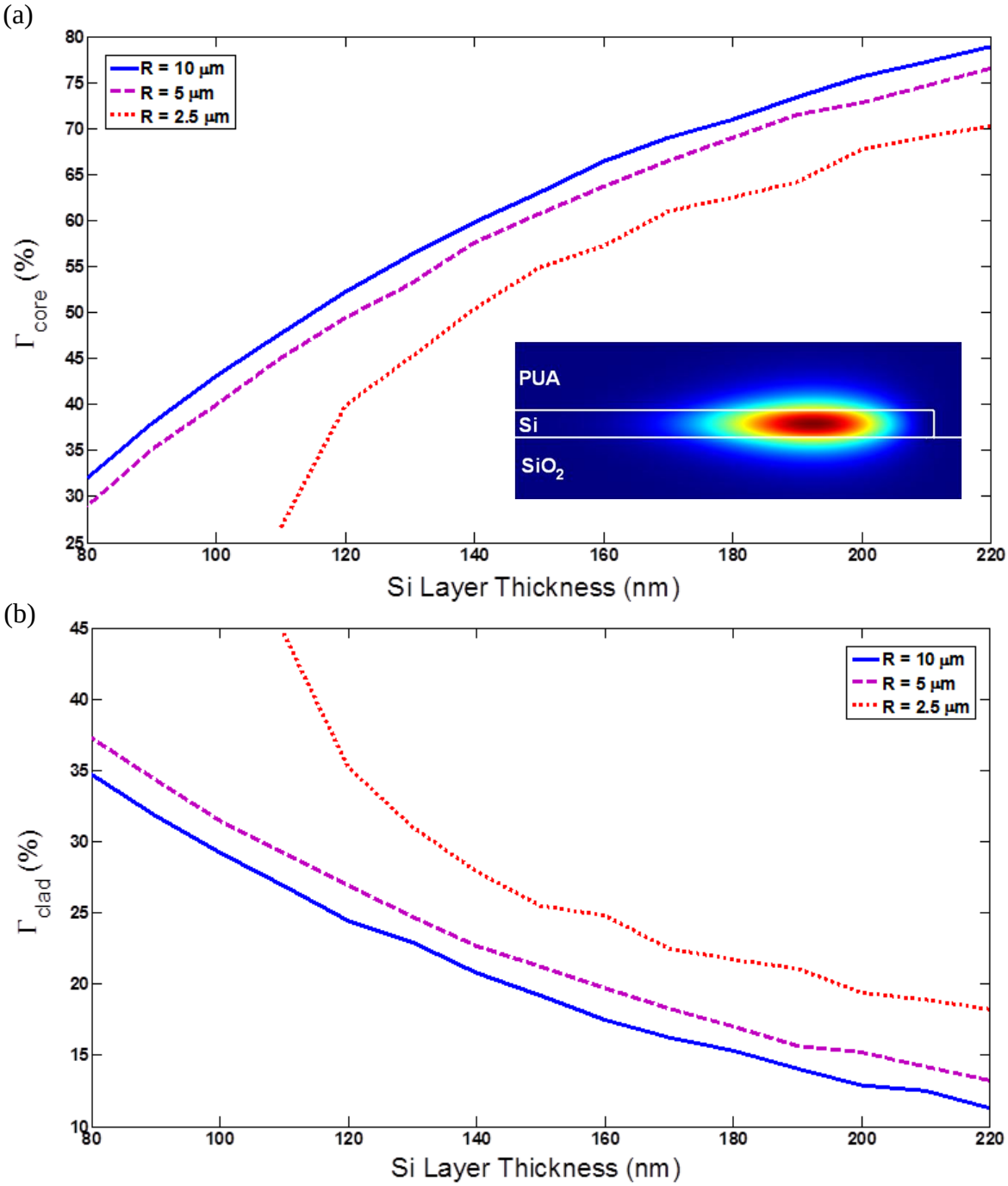

Figure 3.4. Simulation results for the overlap factors (a) Γ_{core} (i.e., mode confinement), and (b) Γ_{clad} as a function of Si thickness for three different resonator radii of 10, 5, and 2.5 μm. The results shown here are for the fundamental TE mode, whose cross-sectional H_z profile can be seen in the inset of (a).

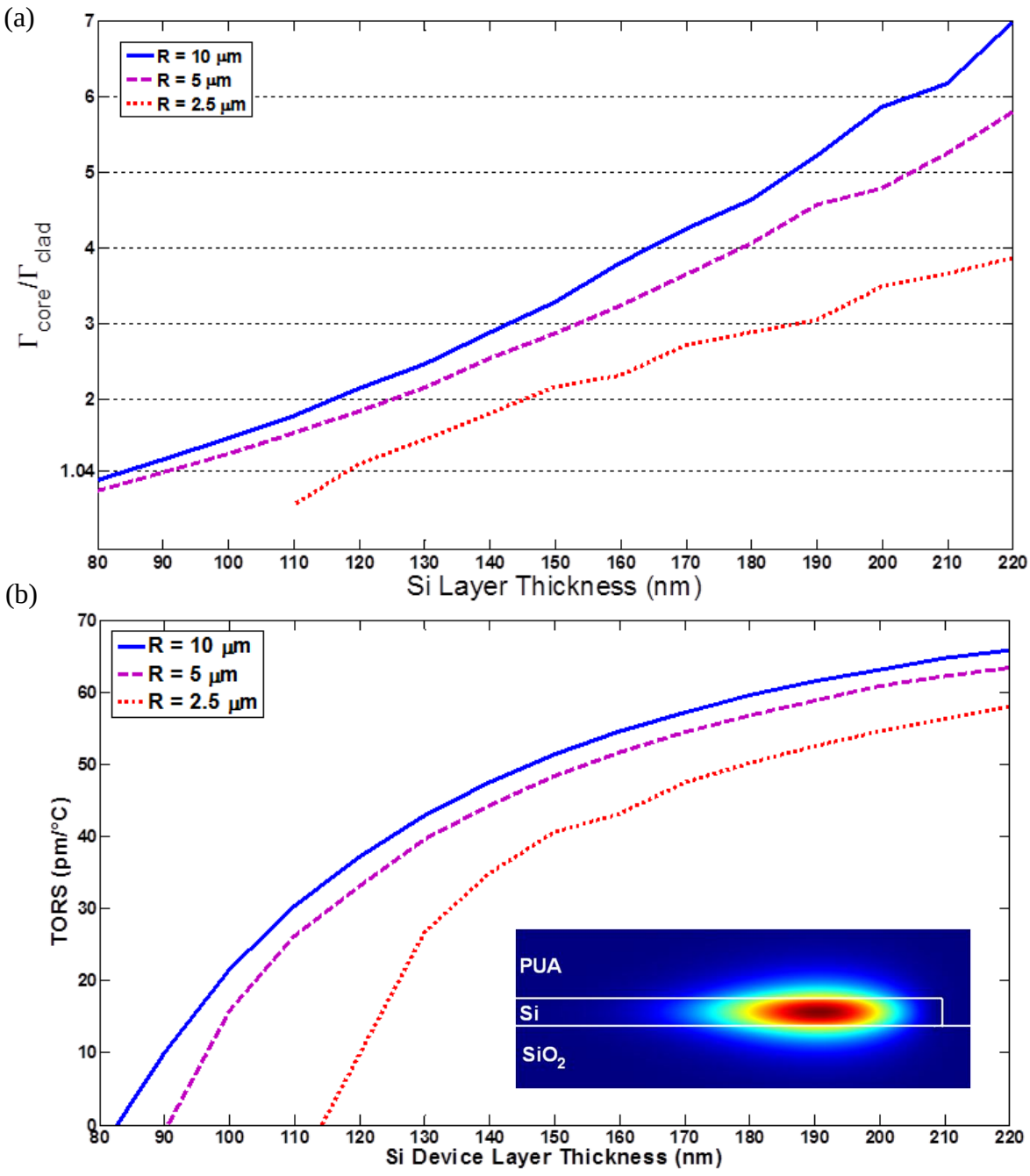

Figure 3.5. Simulation results for (a) the overlap-factor ratio $\Gamma_{core}/\Gamma_{clad}$, and (b) the thermo-optic resonance shift (TORS) for the resonance wavelength closest to 1550 nm, shown as a function of Si thickness for PUA-clad on-substrate microdisk resonators with various radii. The results shown here are for the fundamental TE mode, whose cross-sectional H_z profile can be seen in the inset of (b).

The *Q*s of microdisk resonators are typically limited by the surface scattering and the surface absorption losses [12]. As we reduce the size of the resonator, the resulting decrease in confinement leads to an increase in both of these losses [12]. In addition, the radiation loss also becomes increasingly significant at smaller radii. For example, the radiation *Q*s of three different athermal PUA-clad microdisks, derived using Equation (2.30), are displayed in the following table:

Radius (μm)	Si Thickness (nm)	m	λ_0 (nm)	Q_{rad}
2.5	114	18	1574.23	3,240
5	90	37	1540.18	300,000
10	83	75	1552.34	7.85×10^9

Table 3.1. Radiation *Q*s of three different athermal PUA-clad microdisks for the resonance closest to 1550 nm.

It can be seen from Table 3.1 that while the *Q*s of the 2.5-μm- and 5-μm-radius disks are likely to be limited by radiation, the radiation *Q* of the 10-μm-radius disk is much larger than the typically measured *Q* of ~ 10^6 for the 220 nm thickness. Therefore, the *Q* of this resonator is limited by Q_{ss} and Q_{sa}, both of which also decrease with resonator size, as mentioned earlier. These factors lead to a trade-off between the *Q* and the thermal stability of the resonator. One way to overcome this constraint is to undercut the microdisk before adding the polymer cladding. Removing the BOX layer allows the polymer to fill up the space underneath the microdisk. With a polymer cladding with an index close to that of silica, the BOX layer contains almost half of the optical energy outside the core; therefore, the new configuration will almost double the effect of the polymer and move the athermal condition to larger thicknesses and radii that allow for higher *Q*s. For the undercut geometry, Equation (3.8) can be rewritten as

$$\frac{\Gamma_{core}}{1-\Gamma_{core}} = -\frac{n_{clad}\dfrac{dn_{clad}}{dT}}{n_{core}\dfrac{dn_{core}}{dT}}, \tag{3.9}$$

since $\Gamma_{core} + \Gamma_{clad} = 1$. From this equation, Γ_{core} for athermal performance can be directly calculated from the material properties. With a Si core and a PUA cladding, the result is $\Gamma_{core} \cong 51\%$. Simulation shows that for a 10-μm-radius PUA-clad undercut microdisk at a resonance wavelength around 1550 nm, this degree of confinement is achieved with a Si thickness of ~ 120 nm. Another way of interpreting this result is that, as it can be seen from Figure 3.5(a), the $\Gamma_{core}/\Gamma_{clad}$ ratio for the 10-μm-radius, 120-nm-thick PUA-clad disk is 2.14, which is almost double the athermal ratio of 1.04. By undercutting the resonator, Γ_{clad} (i.e., the denominator) will be almost doubled, which will bring $\Gamma_{core}/\Gamma_{clad}$ close to the athermal ratio. With other factors being equal, mode confinement is higher at shorter wavelengths, which means that with a Si layer thickness of 110 nm (which was available to us for microfabrication), the athermal condition will be achieved around the 1450 nm wavelength. Figure 3.6 shows the TORS as a function of Si thickness in a 10-μm-radius, PUA-clad undercut microdisk, for the resonance wavelength closest to 1450 nm. The data are for the fundamental TE mode, for which the cross-sectional H_z profile is shown in the figure inset. As expected, the TORS is close to zero for a thickness of 110 nm. Lower thicknesses result in overcompensation, and therefore, a negative TORS.

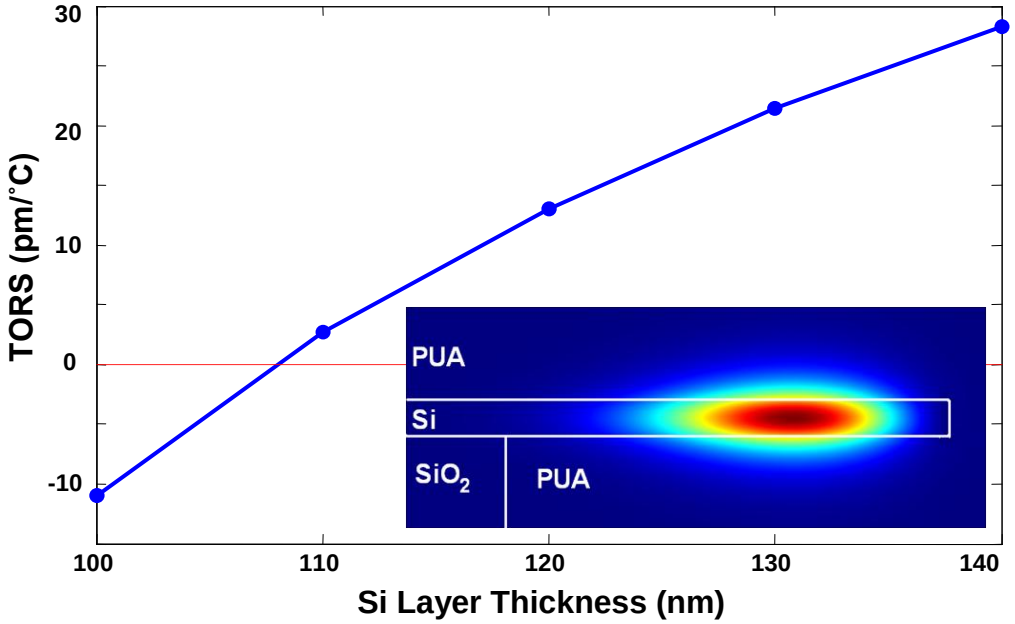

Figure 3.6. Simulation results for TORS versus the Si layer thickness in a 10-μm-radius, PUA-clad undercut microdisk, for the resonance wavelength closest to 1450 nm. The data shown here are for the fundamental TE mode, for which the cross-sectional H_z profile is shown in the figure inset.

3.3.2. Fabrication and Experimental Results

To experimentally verify the proposed design, we fabricated a series of microdisk resonators on SOI wafers from Soitec, Inc. The wafers were thinned down to the desired thickness through a controlled dry oxidation process and subsequent wet etching using buffered oxide etchant (BOE). The patterns were written with electron-beam lithography (EBL) on the ZEP e-beam resist and etched into Si with chlorine plasma in an inductively-coupled-plasma (ICP) machine. The devices were then covered with the 1827 photoresist, and small openings were created around each disk using optical lithography. The photoresist layer then acts as a mask for selective wet etching of the BOX layer using BOE. A schematic of this process is shown in Figure 3.7(a). The depth of undercutting can be adjusted by changing the wet-etch time, considering that the etch rate of SiO_2 using BOE is about 100 nm/min. The target depth must exceed the effective radial extent of the resonant mode, with 3 μm being sufficient for the four lowest-order modes in a 10-μm-radius disk. Finally, the photoresist was removed, and the devices were coated with PUA. An SEM image of an undercut microdisk coupled to a bus waveguide is shown in Figure 3.7(b). The mechanical stability of the suspended waveguide can be improved by adding supports, such as those shown in Figure 3.7(c).

In our measurements, samples are placed on a TEC-equipped stage, and light is coupled into and out of the bus waveguides using tapered lensed fibers. The input polarization state is controlled by a fiber polarization controller. The changes in temperature are monitored using a thermistor mounted on the stage. We measure the transmission spectra before and after increasing the temperature, by using a tunable laser as the input source. Figure 3.8 shows a schematic and a photo of the measurement setup.

(a)

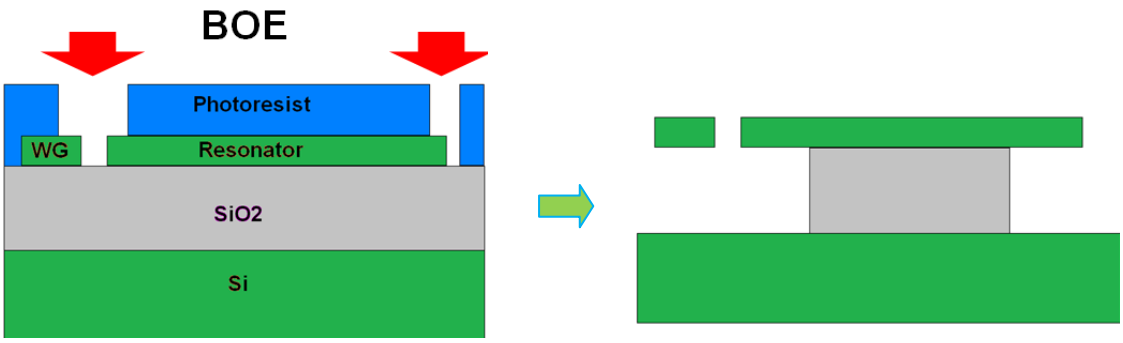

(b)

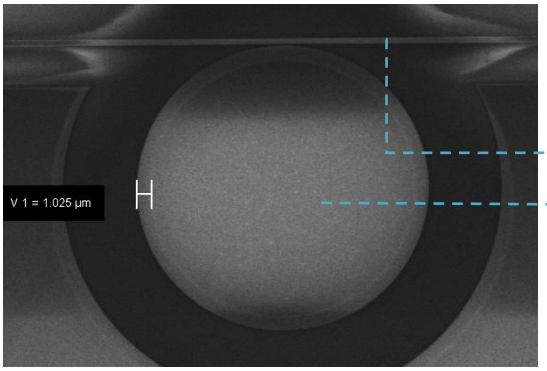

(c)

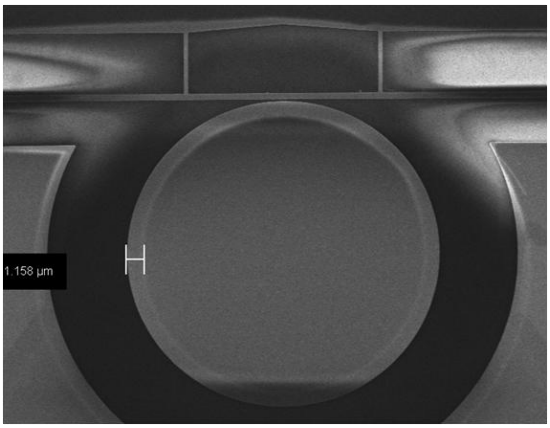

Figure 3.7. (a) A schematic of the selective undercut process. The devices are covered with the 1827 photoresist, and small openings are created around each disk using optical lithography. The photoresist layer acts as a mask for selective wet etching of the BOX layer using BOE. (b) SEM image of a 10-µm-radius undercut microdisk. Undercutting depth is about 1 µm, and the undercutting boundary beneath the disk is visible from the top and has been marked in the image. (c) SEM image of an undercut microdisk with supports for the suspended bus waveguide.

(a)

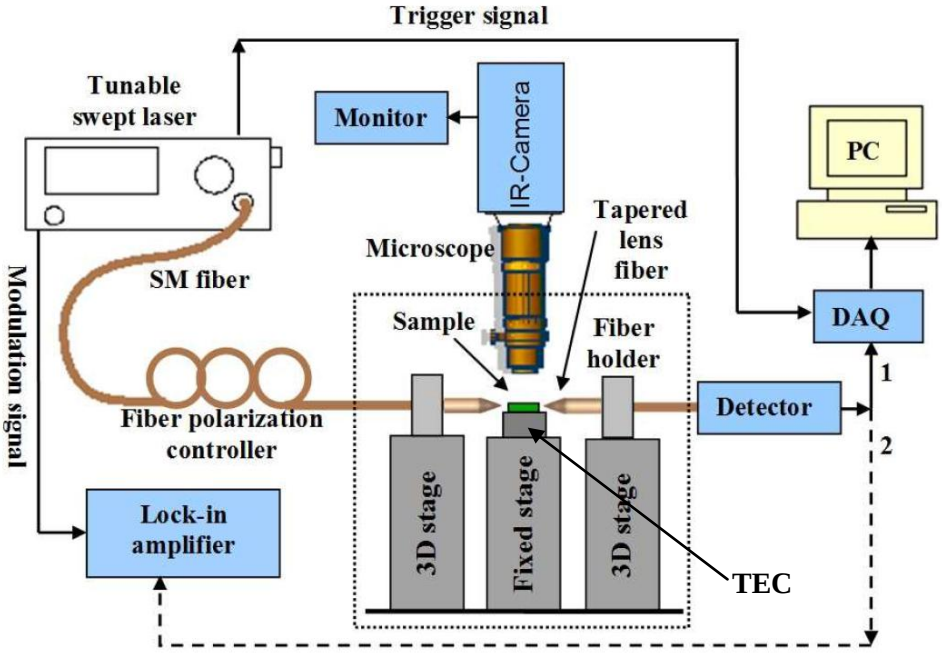

(b)

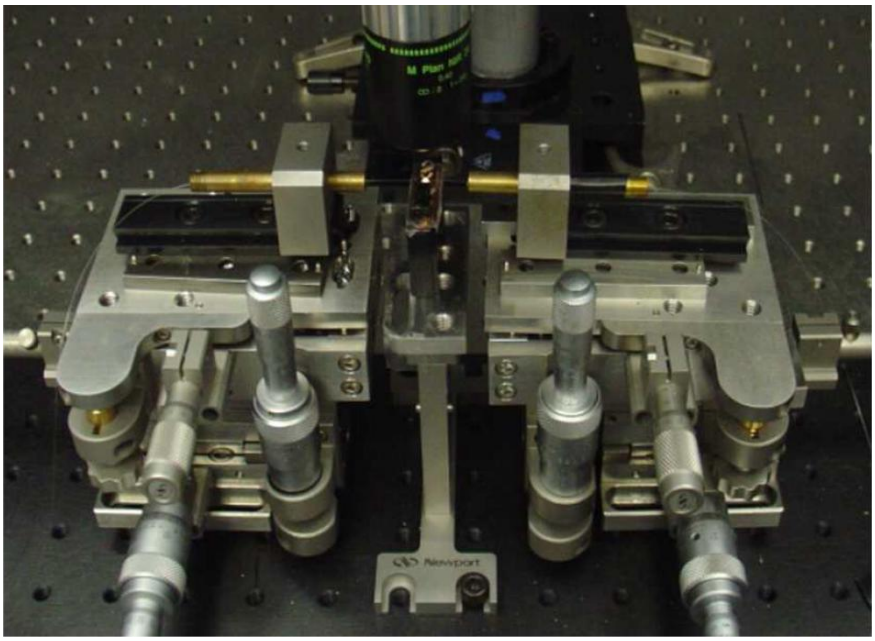

Figure 3.8. (a) Schematic, and (b) photo of the measurement setup.

A number of our TORS measurement results are shown in Figure 3.9. The case shown in Figure 3.9(a) belongs to a 10-μm-radius, 220-nm-thick on-substrate microdisk with air cladding, exhibiting a large TORS of about 78 pm/˚C. Figure 3.9(b) shows the measured TORS after the same microdisk has been covered by PUA, which has reduced its TORS by about 15%, as predicted by simulation. The change in resonance extinction results mainly from the dependence of the waveguide-resonator coupling on wavelength, as well as the change in material indices that affects the field perturbation pattern.

Figure 3.9(c) shows the measured TORS of a PUA-clad, 10-μm-radius, 110-nm-thick undercut microdisk around the 1450 nm wavelength. As predicted by simulation and theory, the resonator exhibits a nearly athermal behavior, with a TORS of about 0.2 pm/˚C. The nearly zero shift in resonance can be compared with the shift in the background Fabry-Perot, which results from reflection at the cleaved ends of the input and output bus waveguides. FSR comparisons reveal that the depicted mode has the smallest FSR, which means that it is the fundamental (1^{st}-order) mode.

(a)

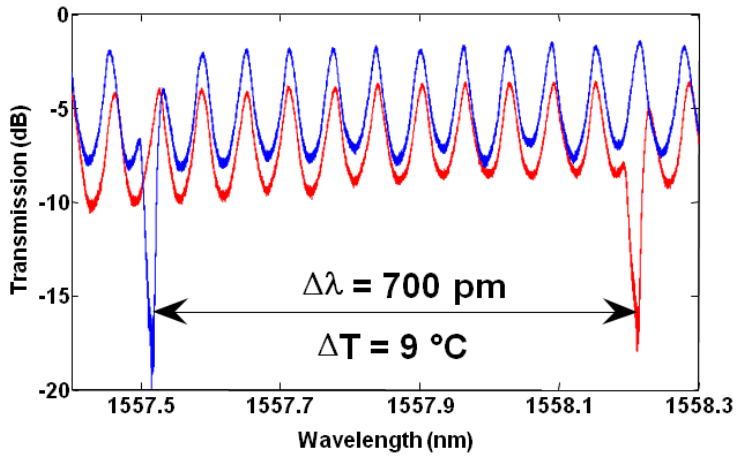

(b)

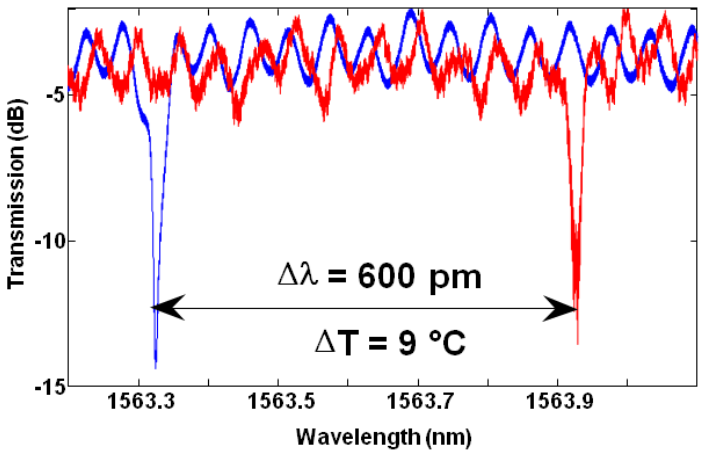

(c)

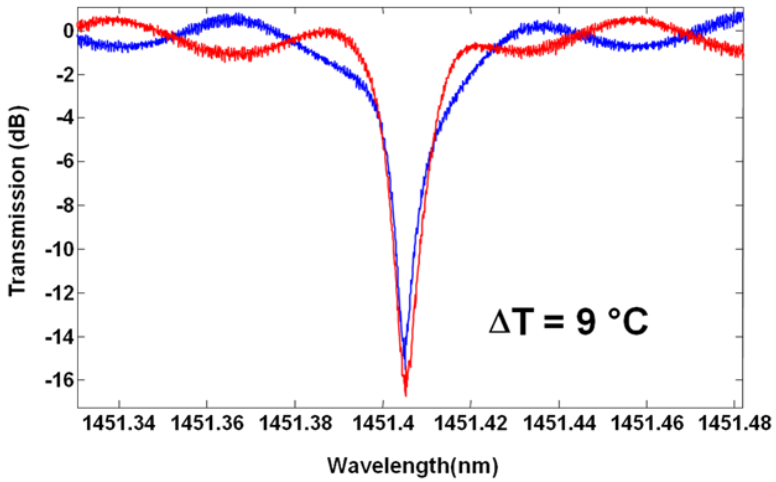

Figure 3.9. (a) TORS in a 10-μm-radius, 220-nm-thick on-substrate microdisk with air cladding. (b) TORS in the same microdisk after adding the PUA cladding, which reduces the shift by about 15%. (c) Athermal resonance in a 10-μm-radius, 110-nm-thick PUA-clad undercut microdisk. The blue and red curves in (a)–(c) correspond to measurements before and after a temperature increase of 9 ˚C, respectively.

Mode confinement is higher at shorter wavelengths, which means that the contribution of the Si core to the overall N_{eff} will be stronger. The TOCs can be assumed to be constant with wavelength, since Si and polymers show little dispersion in the near IR region [37]. These factors lead to a positive TORS for the same device at shorter wavelengths, as shown in Figure 3.10(a) for the 1406 nm wavelength. The resonance shown in this figure belongs to the fundamental TE mode and exhibits a TORS of +4.7 pm/˚C. The reverse is true at longer wavelengths, as shown in Figure 3.10(b) for the 1555 nm wavelength. The resonance has the same mode order and exhibits a TORS of –12.1 pm/˚C. The design process described in this work can be used to achieve athermal performance at any wavelength by proper selection of the device dimensions.

We conducted a series of parallel fabrication runs in order to assess the effects of thickness reduction and polymer addition on the resonator *Q*. The results of the subsequent measurements are displayed in Figure 3.11. Figure 3.11(a) shows an intrinsic *Q* of ~ 660,000 for a 10-µm-radius, 220-nm-thick air-clad on-substrate microdisk, and Figure 3.11(b) shows an intrinsic *Q* of ~ 330,000 for a similar microdisk with a 110-nm-thick Si layer. These measurements show a 50% reduction in the resonator *Q* as a result of a 50% reduction in the Si layer thickness. The addition of the polymer does not significantly change the *Q* of the 110-nm-thick microdisk, as demonstrated by Figure 3.11(c). The intrinsic *Q* of the resonant mode in Figure 3.9(c) is 180,000, which is one order of magnitude higher than the reported *Q*s for athermal microrings [36]. Since undercutting the resonator generally should not result in a reduction in the *Q* [12], we believe that the reduction in the *Q* of the athermal structure can be attributed to the omission of some cleaning steps, which was done in order to avoid damaging the

mechanically fragile undercut structure. This issue can be resolved by using alternative cleaning processes, or by adding more mechanical supports to the waveguide (see Figure 3.7(c)).

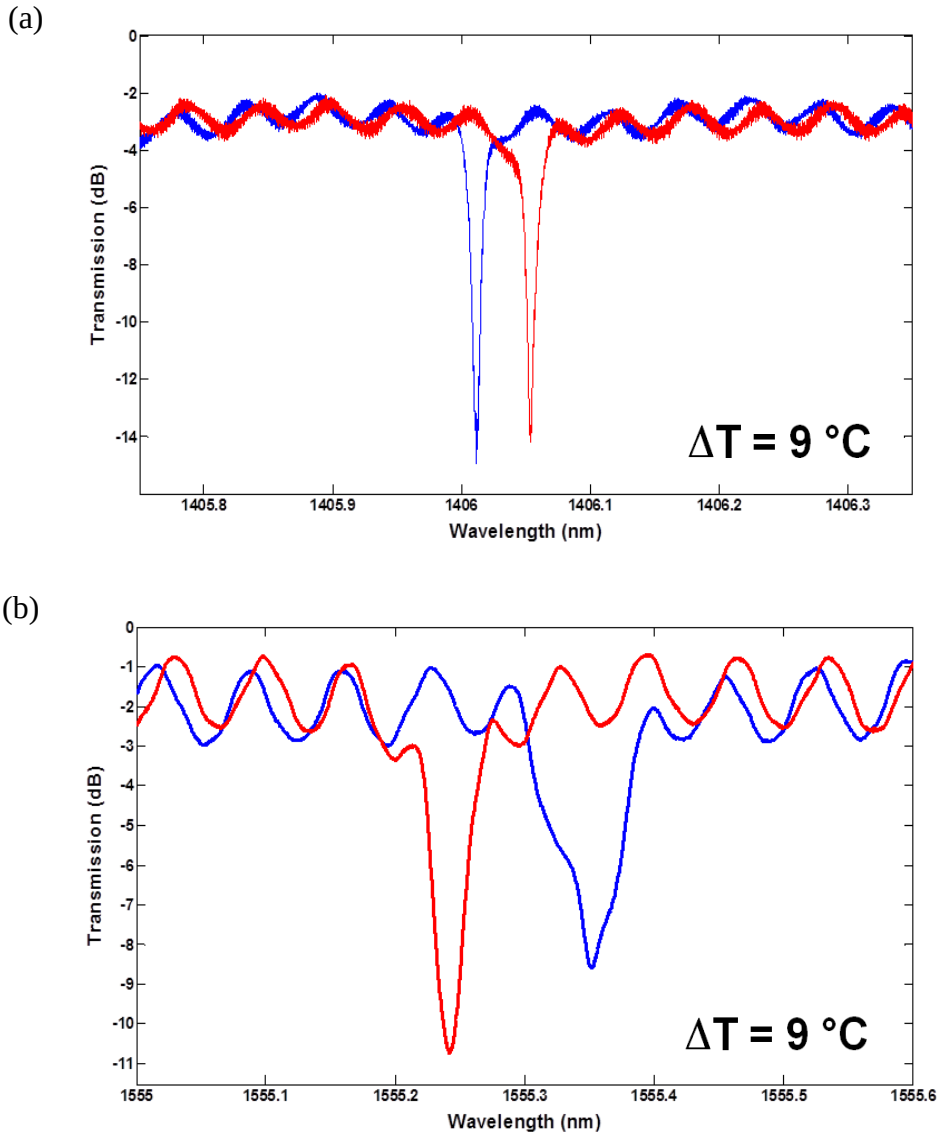

Figure 3.10. (a) Positive (redshift) TORS of +4.7 pm/˚C at 1406 nm, and (b) negative (blueshift) TORS of –12.1 pm/˚C at 1555 nm, for the same 10-µm-radius, 110-nm-thick PUA-clad undercut microdisk characterized in Figure 3.9(c). Mode order and temperature change are also identical.

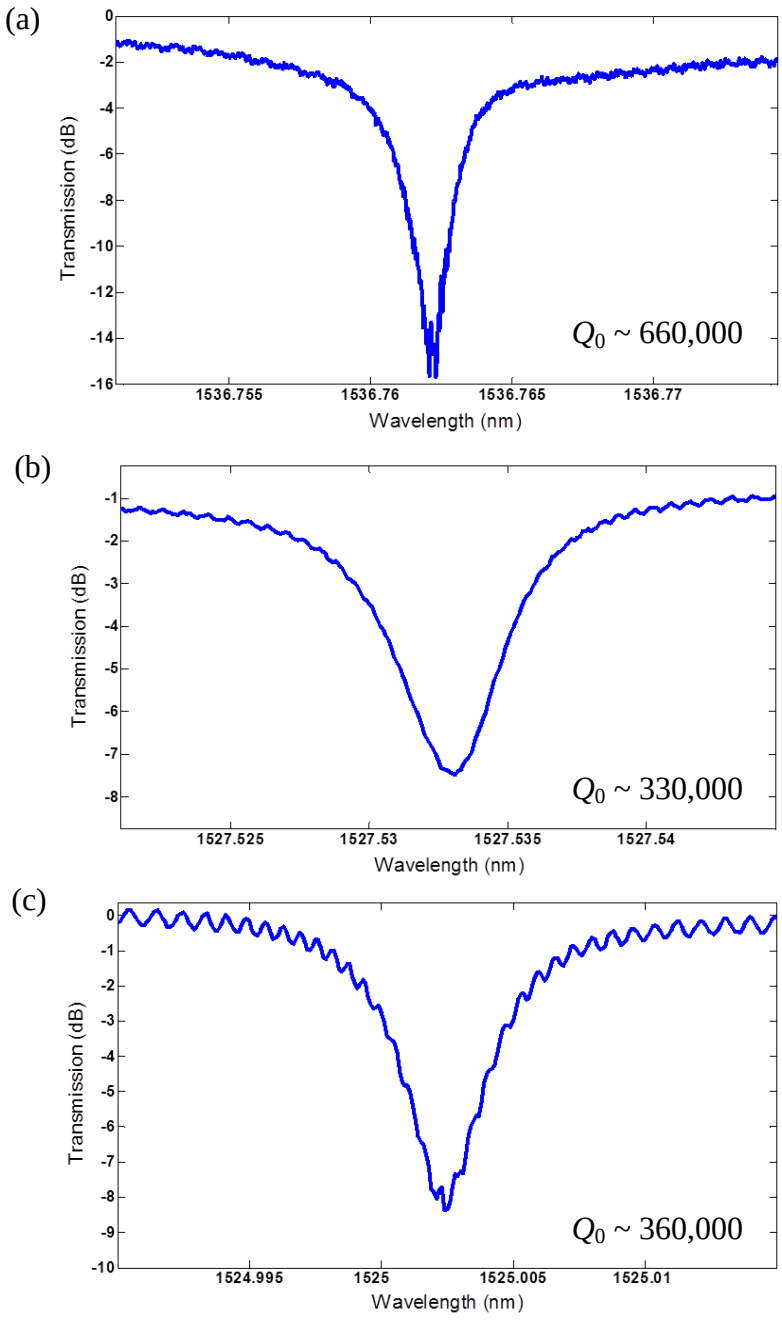

Figure 3.11. Resonance features and their corresponding intrinsic *Q*s in (a) a 10-μm-radius, 220-nm-thick air-clad on-substrate microdisk, (b) a 10-μm-radius, 110-nm-thick air-clad on-substrate microdisk, and (c) a 110-nm-thick PUA-clad on-substrate microdisk.

3.4. An Investigation of the Potential of TiO_2 Claddings for CMOS-Compatible Thermo-Optic Engineering of SOI Microresonators

In Section 3.3, we demonstrated a method to reduce the temperature sensitivity of Si-based TWRs by coating them with the proper polymer that can compensate the positive TOC of the Si core with its own negative TOC. Ultimately, the magnitude of the thermo-optic shift is a function of the core TOC, the cladding TOC, and the confinement of the resonant mode. Some polymers have negative TOCs as large as -5×10^{-4} /˚C, which is very useful for athermal design. However, one drawback of using polymers is that most of them cannot resist high temperatures, which means that they are not compatible with the CMOS fabrication process. Another consequence of this fact is that the athermal operation range of the polymer-clad device will be limited.

It was mentioned earlier that thermo-optic effect in inorganic materials is generally dominated by the increase in polarizability, which results in a positive TOC. However, titanium dioxide (TiO_2, also called titania) is a rare exception to this rule since titania films exhibit a relatively large negative TOC [38–40] whose magnitude depends strongly on the deposition process, as well as the conditions of post-deposition treatment. The negative TOC appears to be a result of film porosity and water adsorption/desorption rather than a property of bulk TiO_2 [40]. Films prepared by e-beam evaporation are reported to have the lowest density and the largest TOC [38].

Titania is the naturally occurring oxide of titanium. It is highly transparent for $\lambda >$ 400 nm ($E_g \sim 3.3$ eV) and has a high refractive index (also strongly dependent on the deposition process, but generally above 2.0 [41–43]) that pulls the optical energy out of the core and into the cladding. The combination of the large TOC and the high index can

significantly reduce the temperature sensitivity of a titania-clad Si device. Because of their high refractive index, transparency, and stability, titania thin films are extensively used in the optics industry. Titania has a melting point of 1840 ˚C, but undergoes other phase transitions at lower temperatures, which can be consequential with regard to the operation of optical devices. Bulk titania occurs in three natural crystalline state: anatase (tetragonal), rutile (tetragonal), and brookite (orthorhombic). Among them, brookite has not been observed in thin films, and rutile is the most common and the most stable [41]. Films that are deposited with a low substrate temperature (generally below 150 ˚C, though this threshold might be higher if particles reaching the substrate have lower levels of energy), whether the deposition is done by sputtering [41], e-beam evaporation [42], or atomic layer deposition (ALD) [43], exhibit an amorphous structure before annealing. Higher substrate temperatures result in crystallization, with anatase occurring first and rutile appearing at higher temperatures. Post-deposition annealing of amorphous films can also result in crystallization, with anatase starting to appear at 250–550 ˚C, and rutile starting to appear at 700–900 ˚C. Rutile has the highest density and the highest refractive index, followed by anatase and then amorphous titania. While a higher refractive index might be desirable for athermalization, the granular structure of polycrystalline claddings results in high optical scattering loss. For these reasons, we decide to perform low-temperature deposition without any post-deposition annealing in order to get amorphous TiO_2 films. We choose e-beam evaporation as our primary deposition method because of its larger negative TOC ($–3\times10^{-4}$ /˚C reported for amorphous, e-beam-evaporated titania [38]). We will also investigate the thermal behavior of microresonators clad with ALD-TiO_2, as ALD is the deposition method that results in the highest film quality.

3.4.1. Design and Simulation

For a typical air-clad SOI microring resonator with a radius of 10 μm and a cross-section of 450×220 nm^2, the TE-mode TORS is about 75 pm/˚C at the 1550 nm wavelength. The TORS of a TiO_2-clad microring will depend on the TOC of the cladding, as well as the confinement of the optical mode, which can be controlled by modifying the dimensions of the resonator. As demonstrated in Section 3.3, varying the radius does not have a significant impact on the TORS of a high-index-contrast SOI TWR, which led us to pursuing our goal by changing the thickness/height of the microdisk. Unlike microdisks, however, there is an additional degree of freedom in microring geometry (namely, the resonator width) that can be used in order to achieve the optimal mode confinement. This gives us the liberty to choose the configuration that results in the highest resonator *Q*, or any other desirable property that we might be aiming for. We used our FEM mode solver to simulate the thermo-optic shift of resonance in 220-nm-thick microrings with different widths, assuming the refractive index and the TOC of titania to be 2.0 and -3×10^{-4} /˚C, respectively. Figure 3.12(a) shows the cross-sectional profile of the resonant mode in a 10-μm-radius 450×220 nm^2 titania-clad SOI microring. Figure 3.12(b) shows the simulation results for TE-mode TORS at 1.55 μm as a function of the microring width. The results suggest the possibility of athermal operation with a width of about 360 nm.

Athermal operation is also achievable by holding the microring width constant and reducing its height (i.e., the Si device layer thickness). Figure 3.12(c) shows the simulations results for TORS as a function of ring height. With a constant width of 450 nm, TORS is reduced to zero when the height reaches 158 nm.

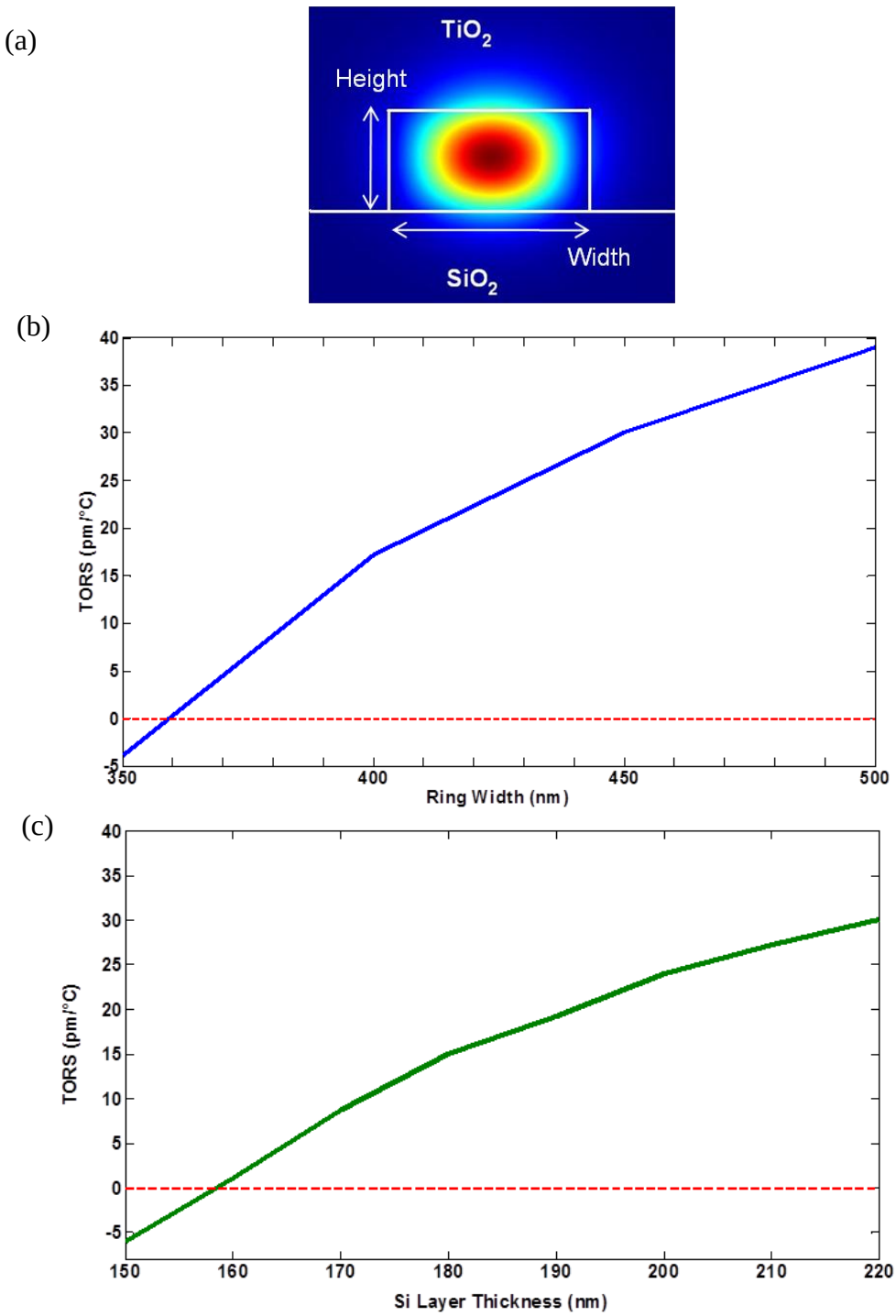

Figure 3.12. (a) Cross-sectional Poynting vector profile of the TE mode of a 10-μm-radius, 450×220 nm^2 titania-clad microring resonator. (b) Simulation results for TE-mode TORS at 1.55 μm in 10-μm-radius, 220-nm-tall titania-clad microrings with different widths. (c) Simulation results for TE-mode TORS at 1.55 μm in 10-μm-radius, 450-nm-wide titania-clad microrings with different heights. A TOC of -3×10^{-4} /°C is assumed for titania in both (b) and (c).

3.4.2. Slant-Sidewall Effect on Thermo-Optic Shift

To this point in our simulations, we have assumed the sidewalls of the resonators to make perfect 90-degree angles with the substrate. This is not the case with practical resists, with ZEP-fabricated waveguides having sidewall angles as low as 70 ˚ (see Figure 3.13(a)). As we saw in Chapter 2, the modes of a microdisk resonator extend toward the center of the disk and away from the edge, helping to reduce the effect of a slanted sidewall. In microrings, however, optical energy is concentrated near the sidewalls, and therefore, a closer examination of this phenomenon is required.

Using our FEM mode solver, we simulated the TE-mode TORS of a series of titania-clad, 10-μm-radius rings with trapezoidal cross sections that are all 220 nm tall and 450 nm wide in the middle, but have different sidewall angles. The sidewall angle was varied in 5-degree steps from 70 ˚ to 90 ˚, and the total temperature change was set to 50 ˚C in order to magnify the second-order effects of a slant sidewall. The refractive index and the TOC of titania were assumed to be 2.0 and -3×10^{-4} /˚C, respectively. Figure 3.13(b) shows the cross-sectional H_z profile of a simulated microring with 70 ˚ sidewalls. The TORS simulation results are shown in Figure 3.13(c). It can be seen that the TORS increases as the sidewalls become more tilted, which implies that the mode confinement goes up with the tilt. However, the magnitude of the effect is quite small, with the relative difference between the highest and lowest TORS values being about 3.4%.

(a)

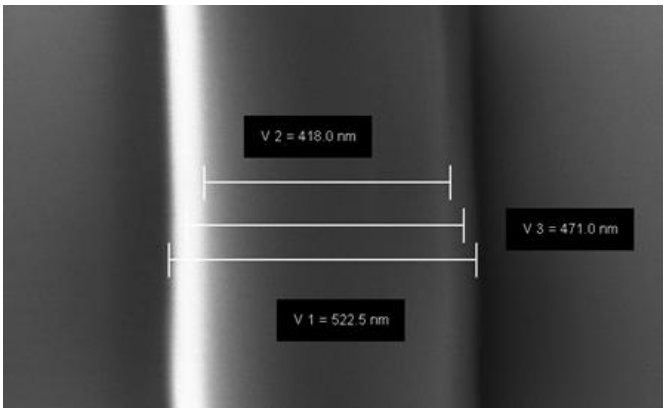

(b)

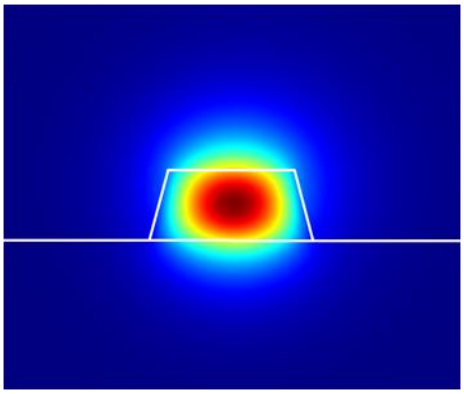

(c)

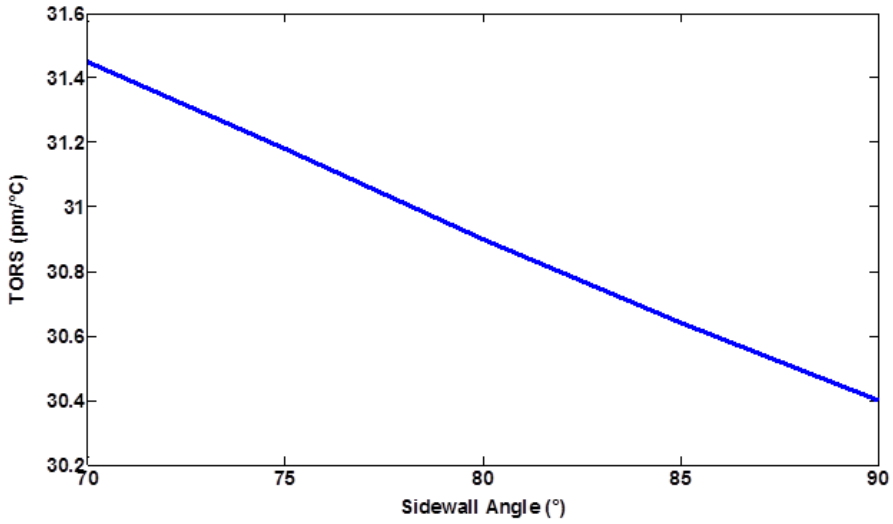

Figure 3.13. (a) Top-view SEM of a 450-nm-wide (CAD input) microring fabricated on a 150-nm-thick SOI. Comparison of the top and bottom widths implies a sidewall angle of ~ 70 ˚. Target width is achieved around the mid-point between the upper and lower values. (b) Cross-sectional H_z profile for the TE mode of a microring with 70 ˚ sidewalls. (c) Simulation results for TE-mode TORS as a function of sidewall angle for a titania-clad, 10-μm-radius microring that is 220 nm tall and 450 nm wide in the middle.

3.4.3. Fabrication and Experimental Results: E-Beam Evaporation

The TiO_2 e-beam-evaporation source used in our study was obtained from Kurt J. Lesker Co. In order for the deposited film to be stoichiometric (i.e., TiO_x with $x = 2$), O_2 flow during evaporation might be needed. The depositions were all performed without heating the substrate, and the stoichiometry was investigated using a Thermo Scientific K-Alpha X-ray photoelectron spectroscopy (XPS) system. It must be noted that there is a tendency for over-oxidation (i.e., Ti_2O_5) at and near the surface of the deposited film; therefore, in-depth XPS must be performed in order to investigate film composition at the vicinity of the optical mode. XPS results show that the O_2 flow required for achieving stoichiometry is dependent on the evaporation tool being used. For example, stoichiometric deposition with a CHA machine required an O_2 flow of 100 sccm, while achieving the same result with a CVC machine did not require any flow at all. Figure 3.14(a) shows the results of an XPS survey scan which confirmed the near stoichiometry ($x = 1.97$) of a TiO_x layer deposited in a CVC machine. The as-deposited stoichiometric TiO_2 films are amorphous, and we have measured their refractive indices to be in the 1.99–2.07 range at the 1.55 μm wavelength using a Woollam M2000 ellipsometer. Figure 3.14(b) shows an example of ellipsometry results for one of these films.

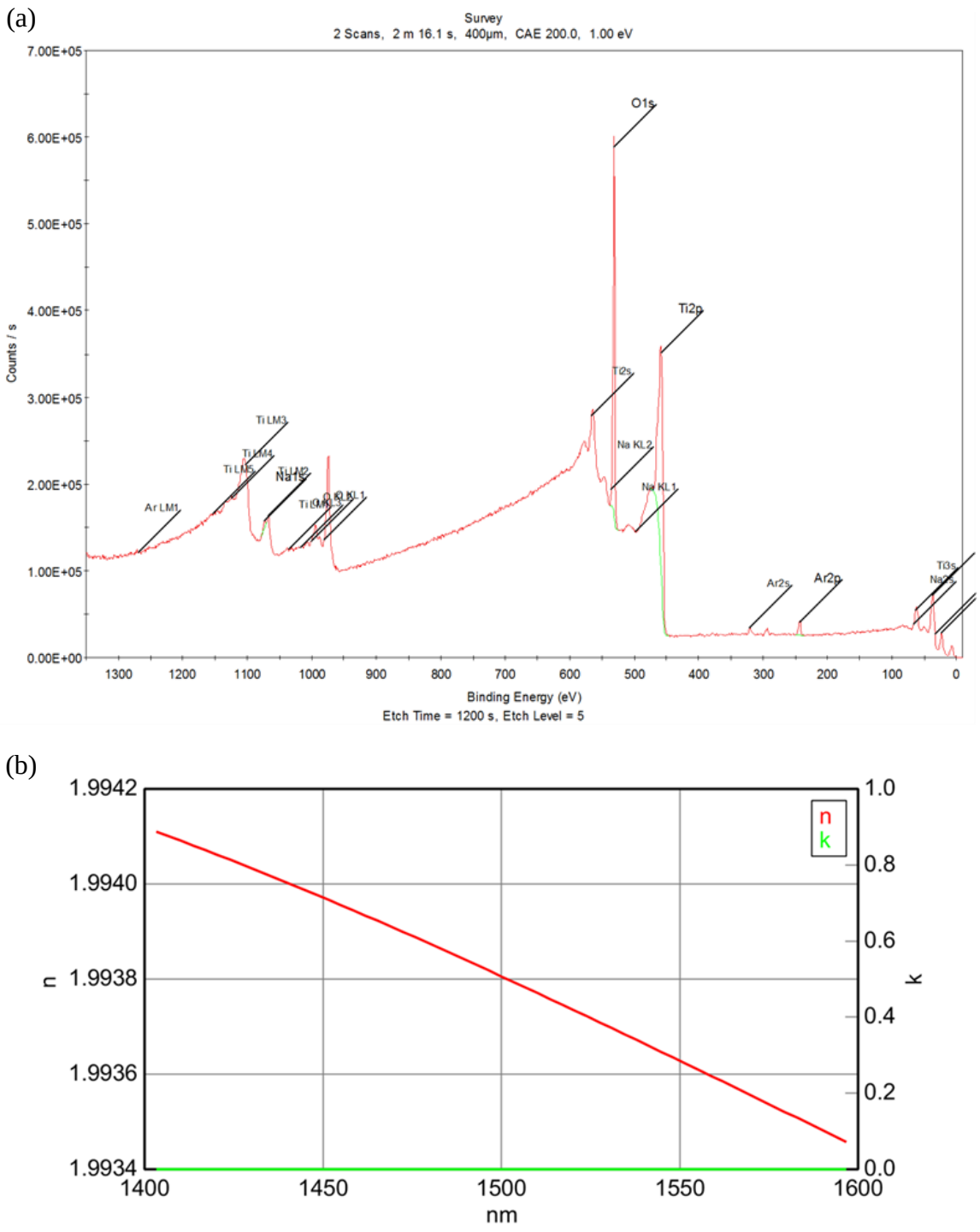

Figure 3.14. (a) XPS survey scan confirming the near stoichiometry (x = 1.97) of a TiO_x layer deposited by e-beam evaporation. (b) Ellipsometry results for an stoichiometric TiO_2 film deposited by e-beam evaporation.

Figure 3.15(a) is a top-view SEM of a 10-μm-radius, 220-nm-tall microring that was fabricated with ZEP-based EBL and Cl_2 plasma etching, and later covered with a 400-nm-thick layer of e-beam-evaporated TiO_2 deposited at a rate of 1 Å/s, as seen in Figure 3.15(b). Figure 3.15(c) shows the temperature-shifted spectra of a 500×220 nm^2 microring for a resonance close to the 1.55 μm wavelength. The TORS measured from this figure is 41.5 pm/˚C, which represents a 45% improvement over a similar air-clad resonator. With a TiO2 refractive index of 2.0 used in simulation, this result corresponds to a TiO_2 TOC of -2.8×10^{-4} /˚C, which is close to the value assumed in our previous simulations. The narrower microrings that are designed to be athermal (i.e., width ~ 360 nm) are currently too lossy to allow an accurate measurement of the TORS. However, resonator *Q* can be increased by improving the etching process and also the TiO_2 film quality. Therefore, our results demonstrate the possibility of realizing CMOS-compatible athermal resonators on SOI with e-beam-evaporated TiO_2 claddings.

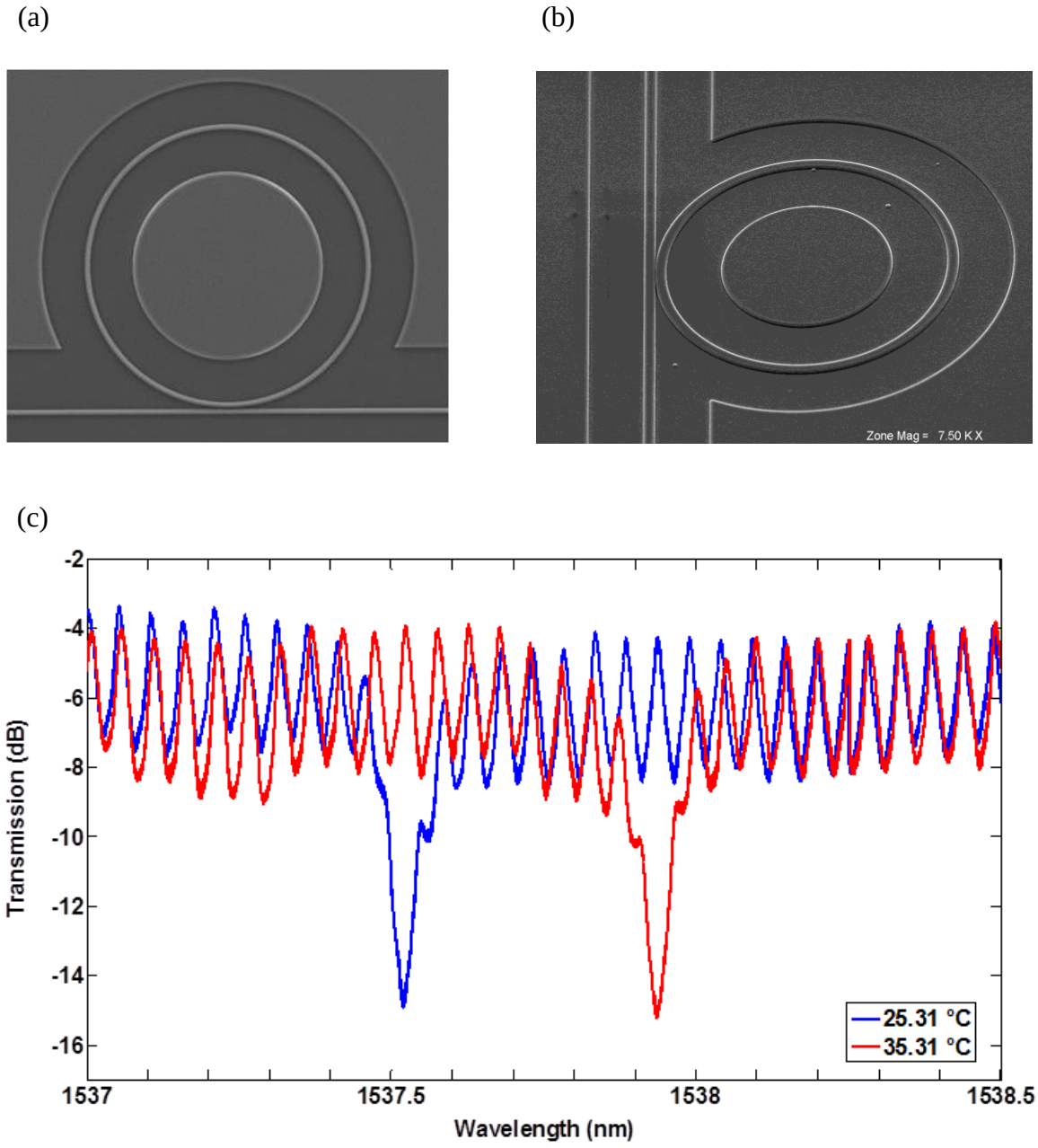

Figure 3.15. (a) Top-view SEM of a 10-μm-radius, 220-nm-tall microring fabricated with ZEP e-beam lithography and Cl_2 plasma etching. (b) Slanted SEM of a similar microring after being coated with a 400-nm-thick layer of e-beam-evaporated TiO_2. (c) Temperature-shifted spectra of a 10-μm-radius, 500×220 nm^2 titania-clad microring with a TORS of 41.5 pm/˚C.

3.4.4. Simulation, Fabrication and Experimental Results: ALD

Ref. [40] reports large negative TOCs for thin ALD-TiO_2 films (e.g., $–3.4\times10^{-4}$ /˚C at 1.55 μm for a 60-nm-thick film), which rapidly decrease in magnitude as film thickness is increased (e.g., $–1.8\times10^{-4}$ /˚C for 100 nm and $–6\times10^{-5}$ /˚C for 200 nm). The refractive index of these films is higher than that of e-beam-evaporated ones (2.27 at 1.55 μm), and so is the film quality. However, the larger TOC and refractive index do not lead to improvements in TORS reduction over e-beam-evaporated films, because the slightly larger TOC is achievable only with very thin films that can contain only a small portion of the mode energy. Figure 3.16(a) shows the cross-sectional TE mode profile of a simulated 10-μm-radius, 450×220 nm^2 microring resonator covered with a 40-nm layer of ALD-TiO_2. Simulation shows that with a TiO_2 TOC of $–3.4\times10^{-4}$ /˚C, this resonator will have a TORS of 53.8 pm/˚C at 1.55 μm, which is about 80% larger than the e-beam-evaporated counterpart. Reducing the resonator width to 350 nm merely reduces the TORS to 39.3 pm/˚C, while the e-beam-evaporated counterpart shows a negative TORS.

We fabricated a set of microring resonators similar to those discussed in the previous subsection, and in collaboration with Prof. Seppo Honkanen's group at Aalto University in Finland, coated them with 40 nm of ALD-TiO_2. Figure 3.16(b) shows the temperature-shifted spectra of a 10-μm-radius, 450×220 nm^2 microring for a resonance close to the 1.55 μm wavelength. The TORS measured from this figure is 68.1 pm/˚C, which is even larger than the value predicted by simulation. We conclude that, despite their high quality, ALD-TiO_2 claddings are not useful for TORS compensation.

(a)

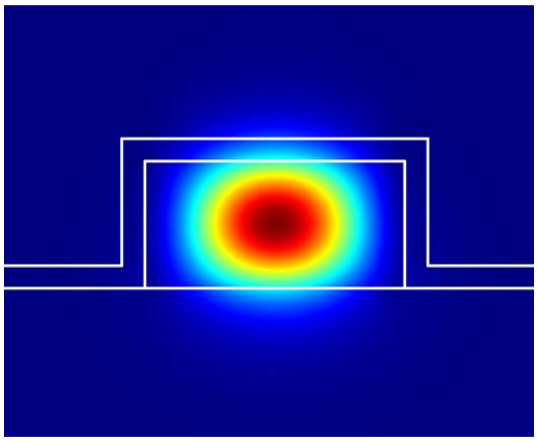

(b)

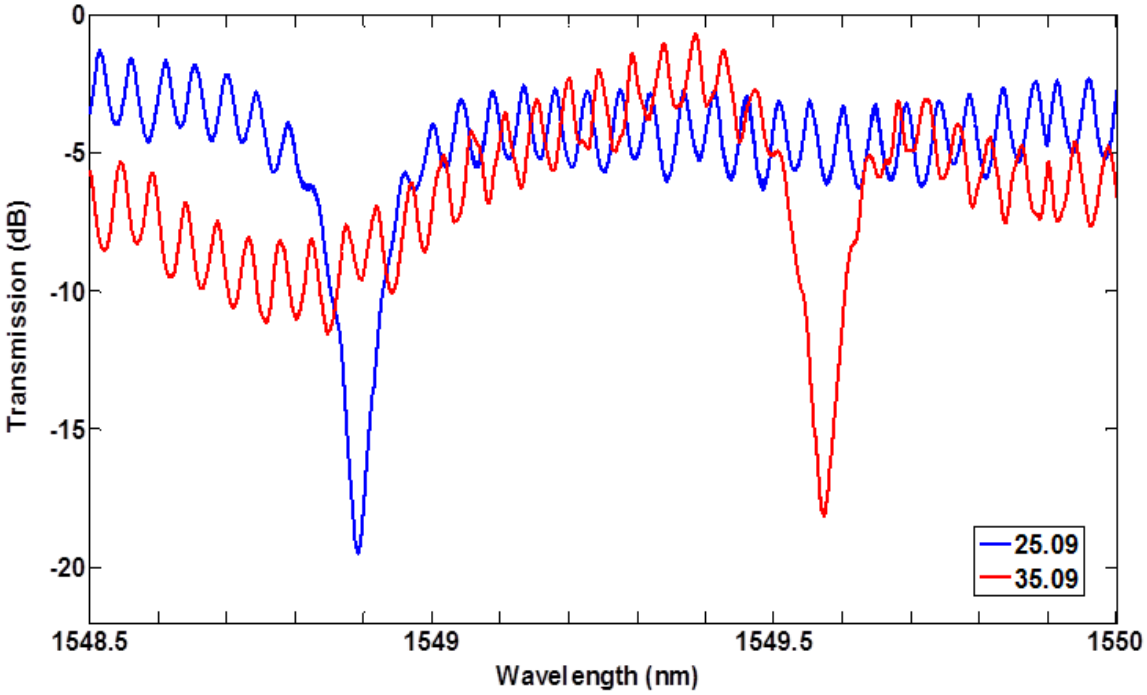

Figure 3.16. (a) Cross-sectional Poynting vector profile of the TE mode of a 10-μm-radius, 450×220 nm^2 microring resonator coated with 40 nm of ALD-TiO_2. (b) Temperature-shifted spectra of the device described in (a), showing a TORS of 68.1 pm/˚C.

CHAPTER 4

A COMPACT AND FULLY RECONFIGURABLE RF-PHOTONIC FILTER ON SOI

4.1. Introduction

With the growing demand for wideband services such as wireless communication and ranging, RF signal carriers used in these applications have been pushed to higher and higher frequencies in the quest for higher bandwidths. However, the speed and precision of wideband signal processing in the electronic domain is usually limited by the available sampling frequency (up to a few GHz, as mentioned earlier), and the resolution of the analog-to-digital converters (ADCs) [44,45]. In addition, the tuning range of electronic RF filters is limited by the RF carrier frequency [3]. Reconfigurable optical systems offer a solution to this challenge by providing low-loss and high-bandwidth filters that can be tuned over a wide frequency range [3]. In a basic RF-photonic system such as the one shown in Figure 4.1, an optical carrier is modulated by the RF signal, and the modulated signal is then processed in the optical domain. Subsequently, the processed signal is converted back to the electronic domain with a photodetector and then digitized. Such RF-photonic systems improve our ability to process wideband RF signals [3].

There have been several reports on the development of such filters on different platforms including SOI [46,47] and InP substrates [48]. However, most of these filters are implemented by using long waveguides to achieve the required delay, which results in a relatively large footprint on the chip and small free spectral range (FSR) for the filter response. In this chapter, we present a fully reconfigurable filter unit cell on a CMOS-compatible SOI platform using compact and low-loss delay-line elements that are based

on high-*Q* microdisk resonators [29]. The use of this resonator-based filter architecture results in a dramatic reduction in the size of the unit cell, and thus, the possibility of cascading a large number of these unit cells on a very small footprint to achieve the desired filtering response. We use the thermo-optic effect in Si to reconfigure the filter by thermal tuning, as opposed to tuning by free-carrier injection/depletion. As discussed earlier, the latter method is faster but has a high and phase-dependent insertion loss caused by free-carrier absorption. Thermo-optic tuning is a more suitable option for cases where the desired reconfiguration speed is not too high, especially when the number of reconfigurable elements is large enough to make the cumulative insertion loss of free-carrier-based phase shifters intolerable. The proposed filter architecture is presented in Section 3.2, and its implementation is discussed in Section 3.3. Experimental results are demonstrated in Section 3.4, and additional details are discussed in Section 3.5.

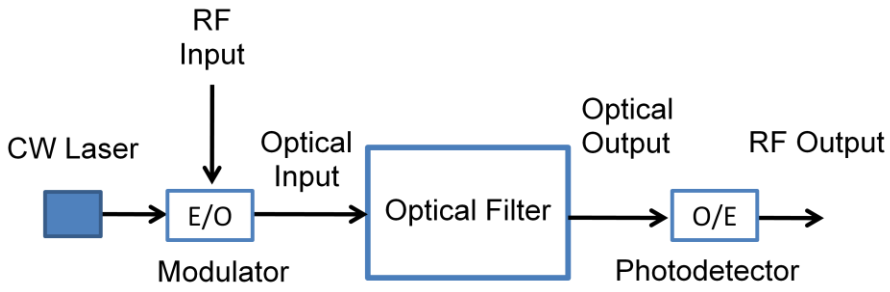

Figure 4.1. Schematic of an RF-photonic filter system.

4.2. Filter Architecture

Our filter-design technique is based on developing a fully reconfigurable unit cell as a basic low-order filter, and then combining multiple unit cells to implement higher-order filters. Each unit cell is a Mach-Zehnder interferometer (MZI) with a tunable single-pole, single-zero all-pass filter (APF) on each arm, and a tunable phase term (β) on one of the arms [49]. The filter unit cell has two poles and two zeros. A schematic of the

unit cell is depicted in Figure 4.2, and an optical micrograph of the APF is shown in Figure 4.3(a). The APF consists of a feedback loop (in this case, a racetrack resonator) that is coupled to the MZI arm using a tunable coupler. The tunable coupler itself is an MZI with a tunable phase shifter on one of its arms. The microdisk-based delay line is located on the feedback path. The thermally tunable phase shifters highlighted in Figure 4.3(a) (i.e., ϕ_{MZI} and ϕ_{FB}) are metallic microheaters optimally designed to locally heat a segment of a waveguide or a resonator [50]. The pole and zero of the APF are located at reciprocal locations with respect to the unit circle ($z = e^{j\omega T}$, with T being the unit delay) in the complex plane, as shown in Figure 4.3(b). The phase (angle) of the APF pole is adjusted by changing the feedback phase shift (ϕ_{FB}), while its magnitude is determined by the coupling coefficient of the tunable coupler through ϕ_{MZI} [49], as described by

$$\phi_{MZI} = 2\arcsin\left(\frac{|pole|}{\gamma}\right), \quad \phi_{FB} = -\angle pole \tag{4.1}$$

where γ is the amplitude response of the feedback loop (determined by the waveguide loss and the delay-line loss), and the APF pole is described in the complex plane by $|pole|\exp(j\angle pole)$. The maximum achievable pole radius is therefore equal to γ. The transfer function of the unit cell, when the input and output couplers are both 3-dB, is given by

$$G = -j[A_U + \exp(-j\beta)A_L]/2, \tag{4.2}$$

and

$$H = [A_U - \exp(-j\beta)A_L]/2, \tag{4.3}$$

where A_U and A_L are respectively the transfer functions of the upper and lower APFs. The unit cell poles are identical to the poles of the two APFs; however, the locations of its

zeros can be tuned independently by adjusting the input and output coupling ratios, as well as β. This gives us full control over the placement of the unit cell poles and zeros, and therefore, full control over the bandwidth and the center frequency of the filter. The filter can be configured as band-stop or band-pass. For the filter response to be symmetric around the center frequency, the poles have to be complex conjugates of each other, and so do the zeros. Figure 4.4(a) shows the simulated response of a lossless band-pass unit-cell filter with $|pole| = 0.98$, $\angle pole = \pm 0.026$, and $\beta = \pi$. The effect of adding loss to the simulation is also demonstrated in this figure. Figure 4.4(b) is the corresponding pole-zero diagram for the lossless case. Changing β from π to 0 changes the locations of the zeros, and the same unit cell will now behave as a band-stop filter, as shown in Figure 4.4(c). The corresponding pole-zero diagram for the lossless case is shown in Figure 4.4(d).

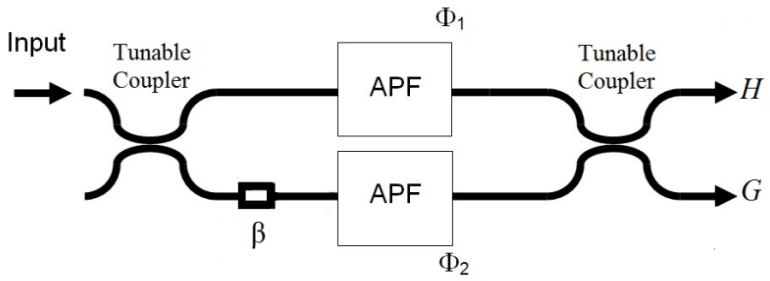

Figure 4.2. Schematic of the filter unit cell. Each APF has one pole and one zero. β is a tunable phase shift. H and G are the transfer functions of the unit cell in the upper and lower outputs, respectively.

(a) (b)

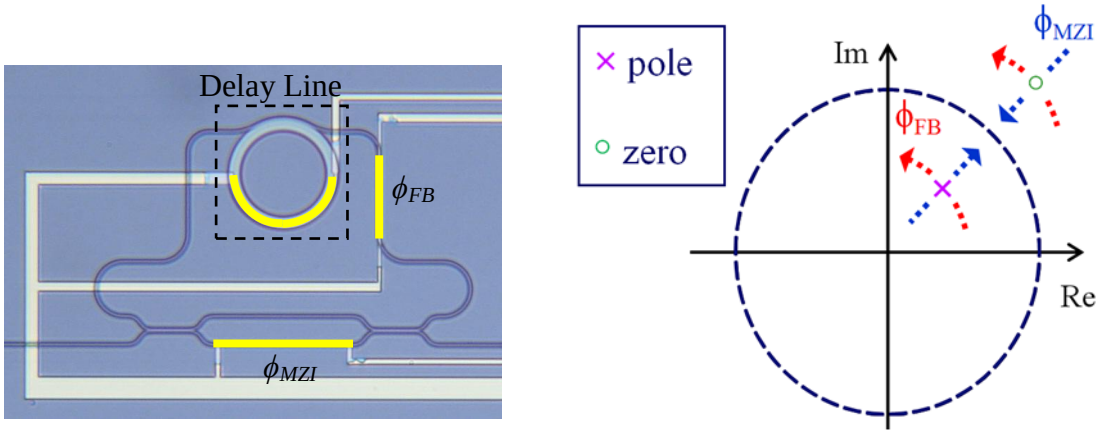

Figure 4.3. (a) Optical micrograph of the APF located on each MZI arm in the filter unit cell shown in Figure 4.2. The highlighted areas show the metallic microheaters that are used to adjust the center frequency of the filter, the feedback phase shift (ϕ_{FB}), and the tunable coupler phase shift (ϕ_{MZI}). (b) The corresponding pole-zero diagram showing the simultaneous movements of the pole and zero as the phase shifters are tuned. The phase (angle) of the pole is adjusted by changing the feedback phase shift (ϕ_{FB}), while its magnitude is determined by the coupling ratio of the tunable coupler (through ϕ_{MZI}).

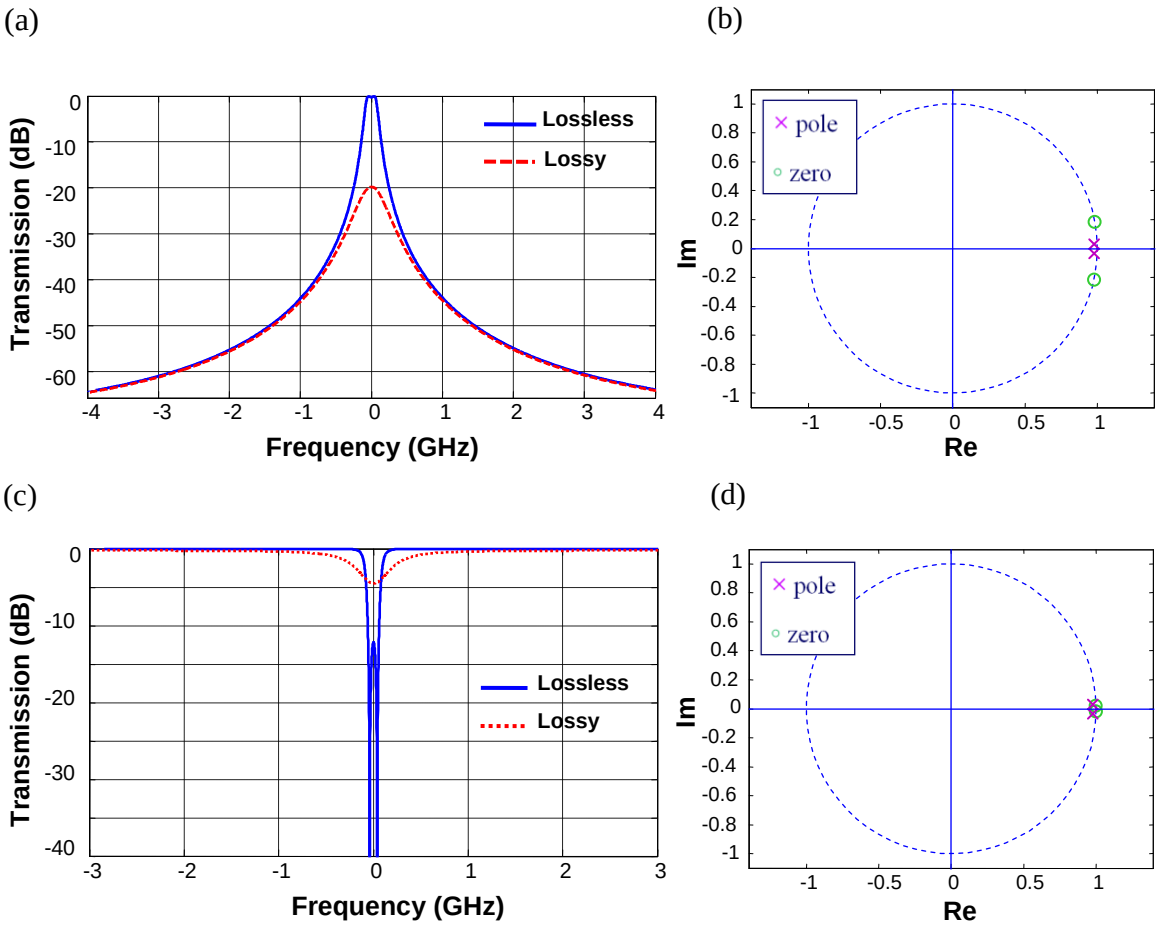

Figure 4.4. (a) The blue (solid) curve is the simulated response of a lossless band-pass unit-cell filter with $|pole| = 0.98$, $\angle pole = \pm 0.026$, and $\beta = \pi$. It has a 3-dB bandwidth of 175 MHz. The red (dashed) curve is the response of the same filter when loss is added to the simulation. The added losses are 4.9 dB/cm for the waveguides and 0.7 dB/cm for the microdisk-based delay lines (see Section 4.3), reducing $|pole|$ to 0.9. The new 3-dB bandwidth is 325 MHz. (b) Pole-zero diagram for the lossless case discussed in (a). (c) The blue (solid) curve is the simulated response of a lossless band-stop unit-cell filter with $|pole| = 0.98$, $\angle pole = \pm 0.026$, and $\beta = 0$. It has a 3-dB bandwidth of 175 MHz. The red (dotted) curve shows the response of the same filter when loss is added to the simulation, reducing $|pole|$ to 0.9. The new 3-dB bandwidth is 300 MHz. (d) Pole-zero diagram for the lossless case discussed in (c).

Higher-order filters can be implemented by combining these unit cells in different configurations, including baseline, cascade, and lattice architectures whose schematics are shown in Figure 4.5. The baseline architecture has the lowest number of tunable elements. The cascade architecture is the easiest to design and characterize (since each stage can be designed and calibrated independently) and has the largest out-of-band rejection. It is also the least sensitive to fabrication imperfections [49]. The lattice architecture has the smallest achievable bandwidth for a given upper limit on the pole magnitude [49]; however, it is the most complex one in terms of design, characterization and reconfiguration. Considering all these factors, we believe that the cascade architecture is preferable to the other two. A fourth-order (i.e., four pole, four zero) filter can be realized by cascading two unit cells.

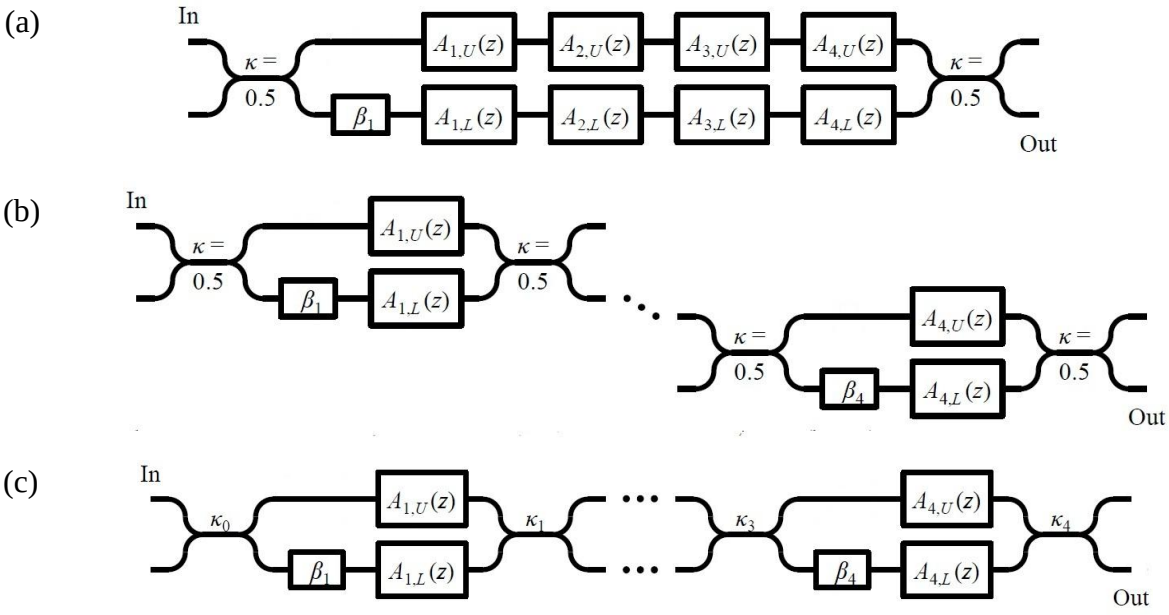

Figure 4.5. Schematic of 8th-order (a) baseline, (b) cascade, and (c) lattice filter architectures. The smaller boxes represent tunable phase shifters with phase shifts given by β_i. The larger boxes represent APFs with transfer functions given by $A_{i,U}(z)$ or $A_{i,L}(z)$. κ_i in (c) represents the power coupling coefficient of the i-th input/output coupler.

4.3. Implementation

The filters were fabricated on an SOI wafer with a 230-nm-thick Si device layer and a 1-μm-thick BOX layer. Such thin SOI platforms enable devices that are more compact than their conventional rib-waveguide-based counterparts, which need to be fabricated on thicker SOIs [51]. Compactness leads to a smaller heat capacity, and therefore, faster reconfiguration with lower power consumption. However, waveguides fabricated on thin SOI have considerably higher propagation losses than rib waveguides do (e.g., 4–5 dB/cm for a 450×230 nm^2 waveguide, compared to less than 1 dB/cm reported for rib waveguides [52]). We break this trade-off between the device size and the insertion loss by using high-Q microdisk resonators (intrinsic Q ~ 1,000,000 corresponding to 0.7 dB/cm of propagation loss) [29] to implement the optical delay elements. Delay lines are extensively used components in our filter architecture and can introduce a great deal of insertion loss if implemented in the form of long, lossy waveguides. Our delay line is a 20-μm-radius microdisk that is strongly over-coupled to a bus waveguide [53], as shown in Figure 4.6(a). Strong single-mode coupling between the waveguide and the microdisk is achieved by using a pulley (or concentric) coupling scheme [54]. From Equation (2.23), the delay created by an strongly over-coupled resonator in the vicinity of resonance can be approximated as

$$T = -\frac{d\Phi}{d\omega} \approx \frac{4Q_c}{\omega_0}, \tag{4.4}$$

which means the coupling Q must equal 30,000 in order to obtain a peak delay of 100 ps at the 1.55 μm wavelength [53]. The addition of this microdisk-based delay line increases the effective propagation length of the racetrack from ~ 300 μm to ~ 7.8 mm. Delay as a

function of frequency detuning (from the center of resonance) is shown in Figure 4.6(b). A detuning of ±1 GHz around the resonance frequency results in a 10% reduction in the magnitude of the delay; therefore, the maximum filter bandwidth is limited by the bandwidth of the delay line. Single-mode coupling means that the filter FSR can be as large as the FSR of the microdisk (~ 650 GHz, or 5.3 nm at the 1550 nm wavelength), which results in a broad spurious-free spectrum and also a large out-of-band rejection for band-pass filters. The above values for the propagation loss and the coupling *Q* result in a maximum pole radius of ~ 0.92 for the filter unit cell.

(a)

(b)

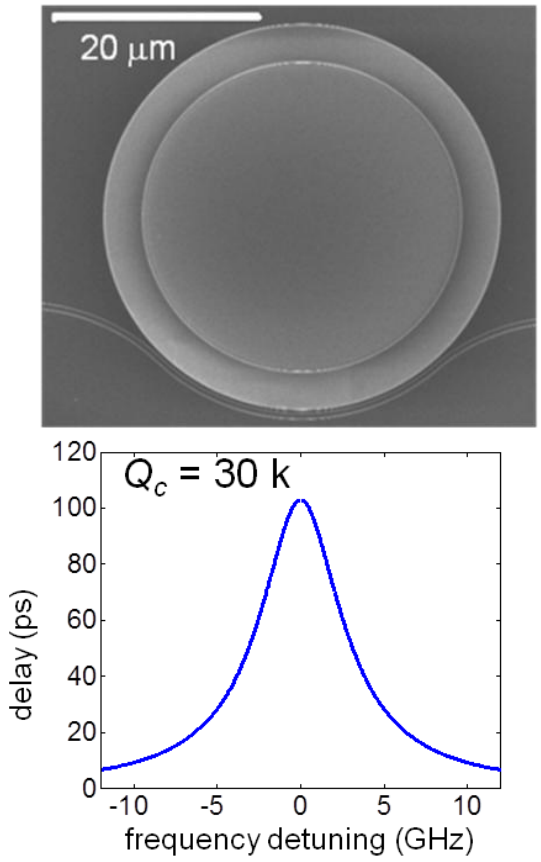

Figure 4.6. (a) SEM image of the low-loss delay line composed of a 20-μm-radius microdisk resonator coupled to a 515×230 nm^2 waveguide in a pulley-coupling configuration. The gap between the waveguide and the resonator in the coupling region is 250 nm. (b) Delay as a function of frequency detuning (from the center of resonance) for the delay line shown in part (a) [53].

The patterns were written on a layer of hydrogen silsesquioxane (HSQ) e-beam resist using a JBX-9300FS EBL system. They were then transferred to the Si layer through dry etching with chlorine plasma in an ICP etching system. Next, the devices were coated with a 1-μm-thick layer of spin-on flowable oxide (FOx®) from Dow Corning, Inc., which has superior uniformity and gap-filling properties compared to deposited oxide films [55]. The FOx layer was fully converted to SiO_2 after 1 hour of annealing at 800˚C in a furnace with O_2 flow [55]. The patterns for the metallic elements were subsequently written on a layer of ZEP-520 e-beam resist that was spin-coated on top of the oxide cladding. After developing the exposed resist, the sample was placed in an e-beam evaporation system and coated with a thin layer of titanium for surface adhesion, followed by layers of nichrome (NiCr alloy) and gold. Nichrome is chosen because of its high resistivity and resistance to oxidation at high temperatures. Lift-off process was then used to complete this step. A third step of EBL with ZEP was performed to define the microheater locations. After development, the sample was immersed in a liquid gold etchant to selectively remove the top gold layer. The high-resistance parts without the top gold layer act as microheaters, while the low-resistance parts form the connections and the contact pads. The fabricated microheaters are 1 μm wide and 30–60 μm long. Figures 4.7(a) and 4.7(b) respectively show a cross-sectional schematic of the fabricated structure and an optical micrograph of a fourth-order cascade filter.

(a)

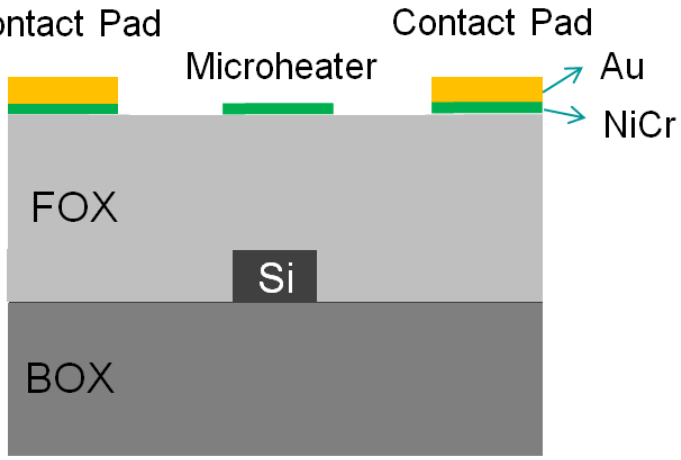

(b)

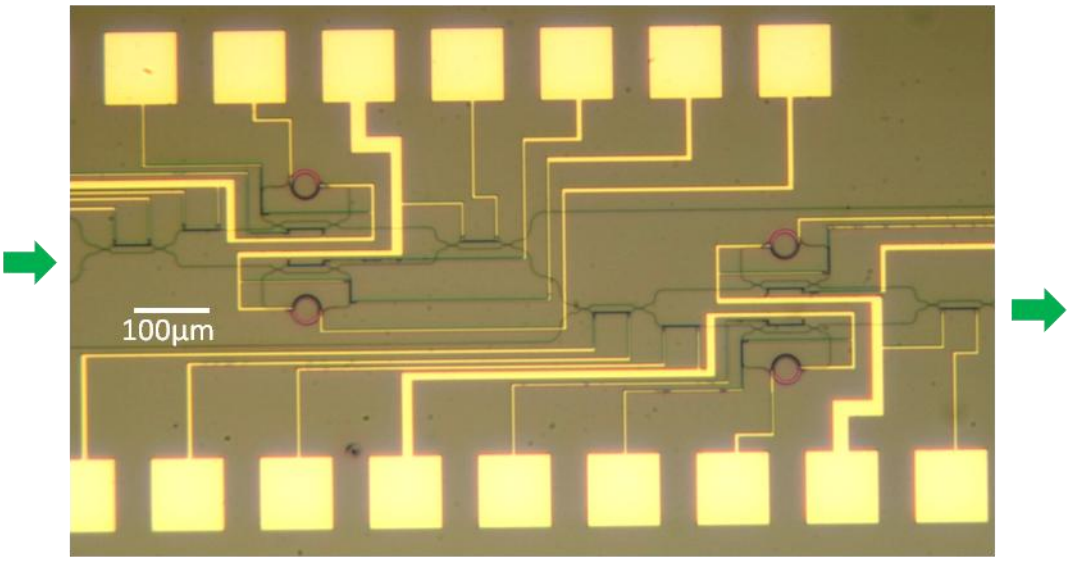

Figure 4.7. (a) Cross-sectional schematic of the fabricated structure for a thermally reconfigurable device. (b) Optical micrograph of the fourth-order cascade filter implemented by cascading two second-order unit cells. The total area of the filter is about 0.25 mm^2.

4.4. Experimental Results

To characterize the fabricated filters, the sample is placed on a thermally stabilized (0.01˚C accuracy) stage. Light is coupled into and out of the sample using tapered lensed fibers, and multi-contact probes are used to apply the tuning currents/voltages to the contact pads on the sample. The power consumption of each microheater is measured to be 20–30 mW per π phase shift. Figure 4.8(a) is the spectral response of the fourth-order cascade filter (see Figure 4.7(b)) in the band-pass configuration, with an FSR of ~ 650 GHz, a 3-dB bandwidth of 4–5 GHz, and an optical out-of-band rejection greater than 38 dB (76 dB after O/E conversion). Figure 4.8(b) is a close-up view of the area within the dashed rectangle in Figure 4.8(a), showing a flat-top response whose bandwidth can be fine-tuned without affecting the other parameters of the response. A different band-pass response is shown in Figure 4.8(c), with two different sets of filter parameters that result in 3-dB bandwidths of 4 GHz and 0.9 GHz. The insertion loss of the filter depends on the filter bandwidth: reducing the bandwidth from 4 GHz to 0.9 GHz increases the two-stage insertion loss from 2.5 dB to 7.5 dB (corresponding to 1.25 dB and 3.75 dB per stage, respectively). This additional 5-dB loss is a result of the increased photon travel time in the APF as the coupling to the racetrack is reduced. Figure 4.8(d) shows that the same device can be reconfigured as a notch filter. Simultaneous tuning of center frequency and bandwidth is also demonstrated in this figure.

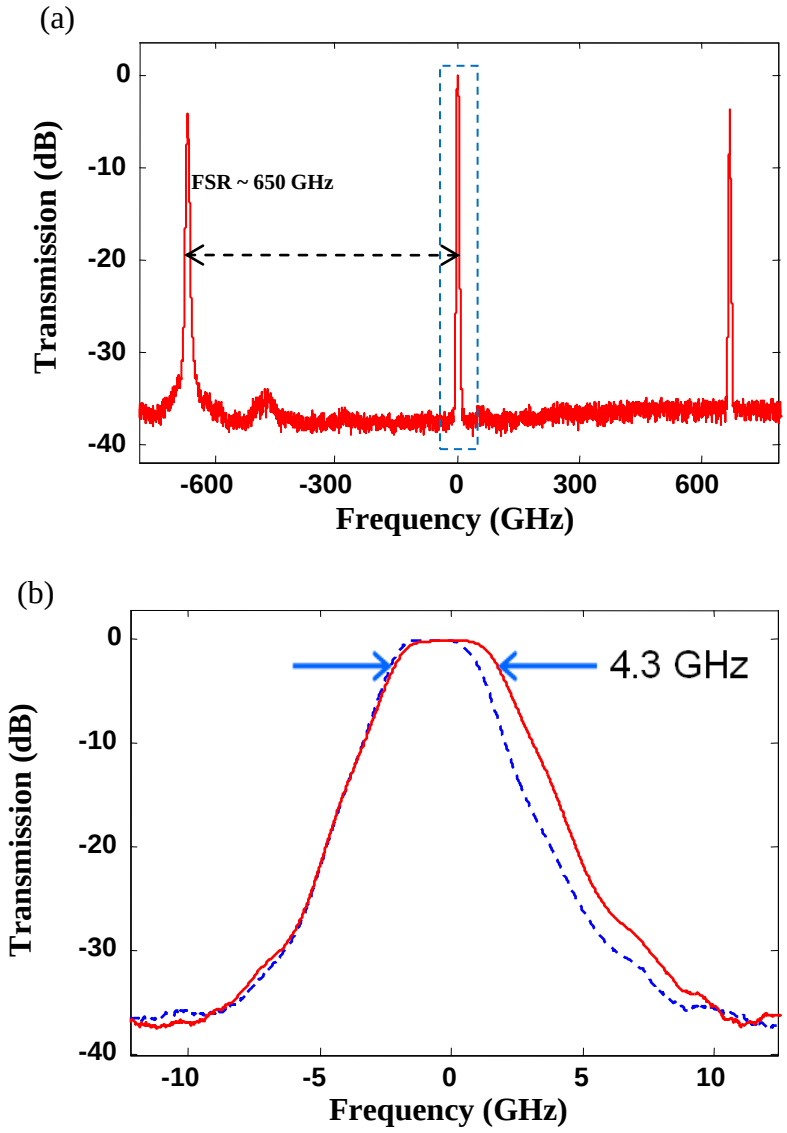

Figure 4.8. (a) Band-pass filter response with an FSR of ~ 650 GHz and out-of-band rejection > 38 dB. (b) Close-up view of the area within the dashed rectangle in (a). The 3-dB bandwidth of the red (solid) curve is 4.3 GHz. The blue (dashed) curve shows that the bandwidth can be fine-tuned without affecting the other parameters of the response.

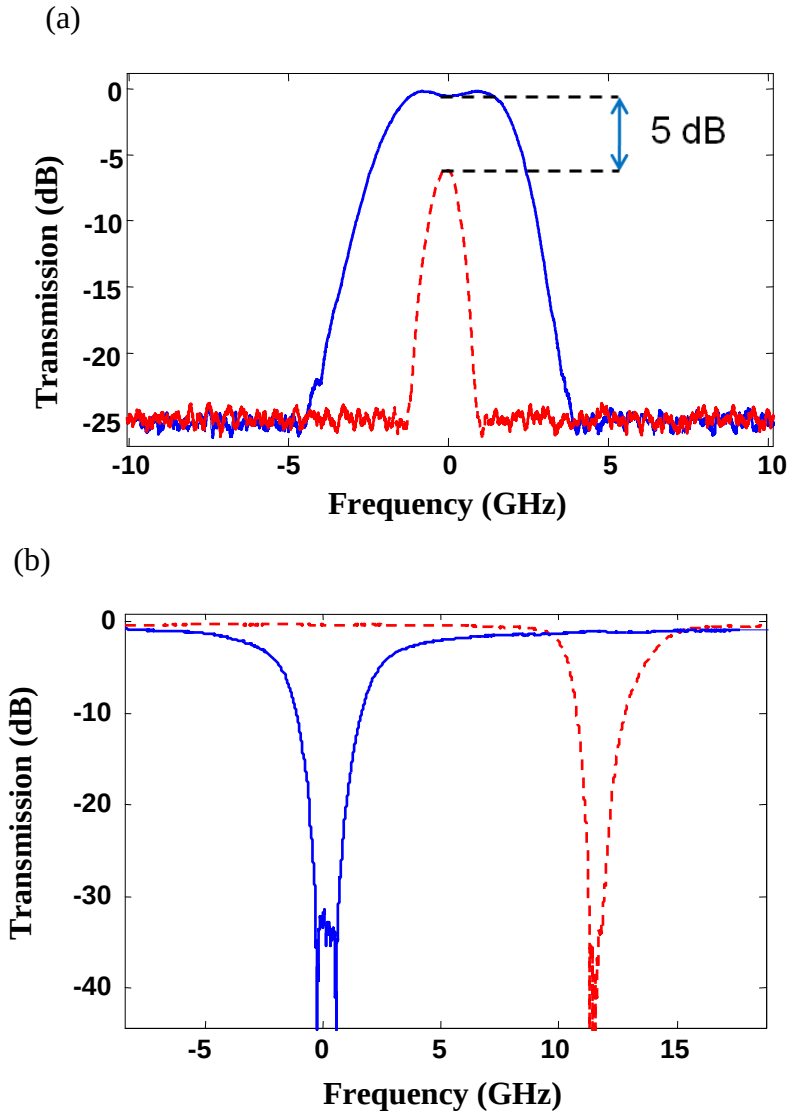

Figure 4.9. (a) Band-pass response with a configuration different from that of Figure 4.8. The 3-dB bandwidth is changed from 4 GHz (blue, solid curve) to 0.9 GHz (red, dashed curve). This change results in an additional 5-dB insertion loss. (b) Notch response with a null depth > 35 dB, obtained by reconfiguring the same filter. Comparison of the blue (solid) and red (dashed) curves shows that the center frequency and the bandwidth of the filter can be simultaneously tuned. The center frequency is tuned by shifting the resonance frequency of the delay-line microdisk.

4.5. Discussion

The maximum achievable bandwidth for this filter is limited by the delay line bandwidth (10% reduction in the delay for a detuning of ±1 GHz), while the minimum achievable bandwidth is limited by the delay line loss. Therefore, spectral resolution can be increased by reducing the resonator and waveguide losses through improving the fabrication quality. An intrinsic microdisk Q of 5,000,000 would provide a spectral resolution better than 100 MHz for a single unit cell. These measures will also reduce the filter insertion loss. The total fiber-to-fiber insertion loss mainly results from the non-optimized coupling at the cleaved facets of the input and output waveguides and can be greatly reduced by improving the fiber-to-waveguide mode matching.

There are nine microheaters per unit cell and each of them has a power consumption of 20–30 mW per π phase shift. However, the required phase shifts are typically much smaller than π. Hence, the average total tuning power per unit cell is usually below 100 mW. The response time of the microheaters is about 4 μs and can be reduced to less than 1 μs using a pre-emphasis driver [50]. Both the speed and the power consumption of reconfiguration can be further improved by one order of magnitude through using resonator-based phase shifters implemented with miniaturized microdisks (e.g., 2 μm radius) [21]. The observed thermal crosstalk between the closest microheaters is less than 5%. The effect of crosstalk can be compensated by measuring the crosstalk coefficients and considering them in the reconfiguration algorithm in order to adjust the applied current/voltage for each microheater accordingly. The crosstalk can be considerably reduced by etching deep micro-trenches around the heaters in order to thermally isolate them [56].

CHAPTER 5

A THERMALLY RECONFIGURABLE DEVICE FOR ADAPTIVE REFLECTION SUPPRESSION ON SOI PLATFORM

5.1. Introduction

Elimination of unwanted feedback can be a necessary function in optical networks for various reasons. For example, the back-reflection of light into a laser cavity can cause laser instability. This function has traditionally been performed by optical isolators. Conventional isolators consist of a Faraday rotator and a pair of polarizers. With the emergence of silicon photonics, the need for a functional, integrated isolator on a CMOS-compatible platform is increasingly felt. To this date, most of the efforts on achieving on-chip optical isolation have focused on the integration of magneto-optic (MO) materials to Si substrates. In the presence of an external magnetic field, MO materials can create a variety of non-reciprocal effects that can be exploited to realize the isolation functionality [57,58]. However, the realization of monolithically integrated isolators on Si has been challenging because of lattice and thermal incompatibilities between Si and MO materials, which necessitate the use of wafer bonding [59]. Furthermore, many of the demonstrated devices have had footprints of several millimeters [59]. The footprint of MO-based on-chip optical isolators can be reduced, at the expense of isolation bandwidth, by utilizing microring resonators that have different resonance wavelengths for clockwise- (CW-) and counterclockwise- (CCW-) propagating modes [59,60]. The problem of monolithic integration was recently addressed in Ref. [59] by depositing an MO cladding material on top of a racetrack resonator, which showed a maximum isolation ratio of 19.5 dB and a 10-dB isolation bandwidth of 1.6 GHz over a footprint of

290 μm in length. In addition to having a limited bandwidth, resonator-based devices also suffer from excess insertion loss that results from an insufficiently large non-reciprocal optical path length achievable by using common magnets. The examples demonstrated in Refs. [59,60] showed insertion losses of 18–19 dB, and even with fully optimized fabrication, a 5–6 dB loss is still expected by the authors of Ref. [59]. Optical isolation has also been demonstrated using nonlinear optical processes [61] and electro-absorption modulation [62]. These devices, however, operate only in specific power ranges, or have modulation-induced frequency sidebands.

5.2. Design and Simulation

In this chapter, we demonstrate a thermally reconfigurable device for adaptive reflection suppression on silicon-on-insulator (SOI) platform without reliance on MO or nonlinear properties. This device is not a true optical isolator as it is not a non-reciprocal device with unidirectional transmission [63]. However, complete unidirectional transmission is not always a necessary condition for achieving reflection suppression. Therefore, devices such as the one demonstrated here that can cancel out the back reflection going into the input port can be used in place of an isolator for reflection suppression purposes. We will show that in applications requiring a high level of reflection suppression and/or low loss, with limited bandwidth and limited variability of reflection, this device has a better performance compared to the existing alternatives.

The device operates by generating a tunable reflection that can destructively interfere with the feedback generated by the source of reflection at the device output. A schematic of the device is shown in Figure 5.1(a). It is composed of a tunable coupler whose ends are connected in order to form a tunable loop mirror. A second tunable phase

shifter is placed after the loop to change the phase of the reflected signal. The tunable loop mirror acts as a perfect mirror if the tunable coupler is set at its 3-dB point, and as a plain waveguide without any reflection if the tunable coupler is set to zero. Therefore, by controlling the coupling coefficient of the coupler, the overall reflectance of the loop mirror can be tuned from 0 to 100%. This full control over the reflectance of the loop mirror and the round-trip phase between the loop mirror and the reflection source (through the phase shifter) enables us to destructively combine these two sources of reflection in the system. If the output reflection coefficient is represented by the complex number $r = |r|\exp(j\phi_r)$, the input reflection coefficient can be derived similarly to that of an asymmetric Fabry-Perot cavity (with one facet being the tunable loop mirror and the other being the source of reflection; see Figure 5.1(b)) and will be given by

$$r' = e^{j\phi_{loop}}\left[-2j\kappa t + \frac{r\left(t^2-\kappa^2\right)^2 e^{j\left(2\phi+\phi_{RT}+\phi_{loop}\right)}}{1+2j\kappa t r e^{j\left(2\phi+\phi_{RT}+\phi_{loop}\right)}}\right], \tag{5.1}$$

where κ^2 and t^2 are, respectively, the power coupling ratio and the power transmission ratio of the tunable coupler, ϕ is the tunable phase shift at the output port, ϕ_{RT} is the phase shift experienced by the signal during a round-trip propagation from the reflection suppressor to the source of reflection and back, and ϕ_{loop} is the phase shift experienced by the signal while propagating through the loop mirror. Under the assumption that the coupler is lossless (i.e., $t^2 + \kappa^2 = 1$), the condition for the left-hand side of Eq. (1) to be equal to zero is

$$r = 2j\kappa\sqrt{1-\kappa^2}\,e^{-j\left(2\phi+\phi_{RT}+\phi_{loop}\right)}, \tag{5.2}$$

which requires the satisfaction of a magnitude condition and a phase condition. Using the two tunable elements, we can achieve this by setting the coupling coefficient and the output phase shift as

$$2\kappa\sqrt{1-\kappa^2} = |r|, \tag{5.3}$$

and

$$\phi = m\pi + \frac{\pi}{4} - \frac{\phi_{loop}+\phi_{RT}+\phi_r}{2}, \tag{5.4}$$

with m being an integer. As can be seen from the above equations, the optimal value of ϕ is periodic with π. Also, for any level of $|r|$, there are two possible values for κ^2, which are symmetric around 0.5. Figure 5.1(c) shows the simulated level of reflection at the input port as a function of ϕ and κ^2, for an illustrative case where 10% of the output power is reflected with $\phi_{loop} + \phi_{RT} + \phi_r = -\pi/2$. The results show the possibility of achieving any level of reflection from 100% down to zero at the input.

(a)

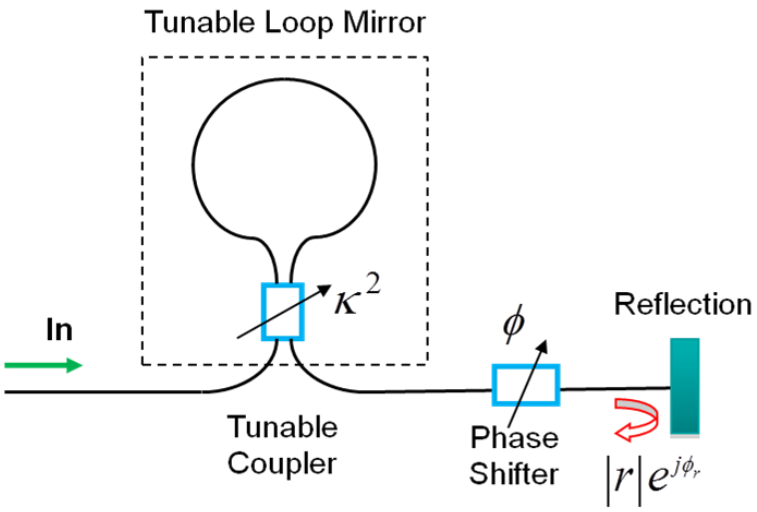

(b)

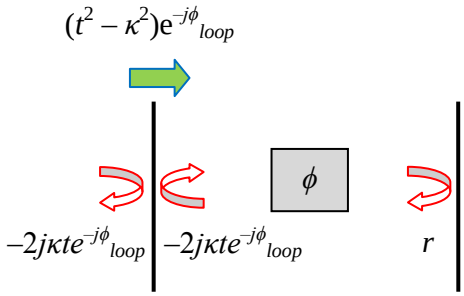

(c)

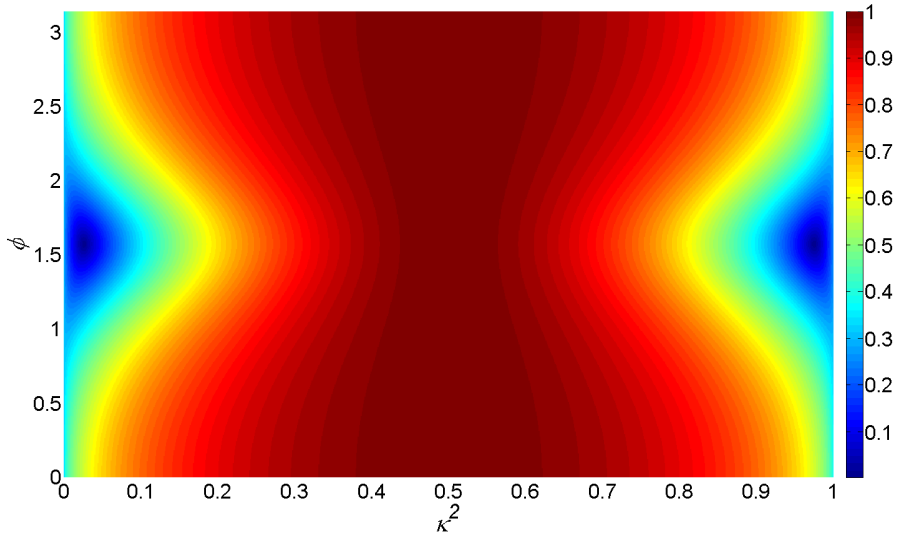

Figure 5.1. (a) Schematic of the proposed reflection suppressor. (b) Equivalent Fabry-Perot etalon for the structure proposed in (a). (c) Simulation results for the magnitude of the input port reflection coefficient as a function of ϕ and κ^2, when 10% of the output power is reflected with $\phi_{loop} + \phi_{RT} + \phi_r = -\pi/2$.

5.3. Fabrication and Characterization

A scanning electron microscopy (SEM) image of the fabricated tunable loop mirror is shown in Figure 5.2(a). The fabrication is performed using electron-beam lithography and dry etching on an SOI substrate with a 220-nm-thick Si device layer and a 1-μm-thick buried oxide (BOX) layer. The waveguide used to form this structure is 450 nm wide. A layer of flowable oxide (FOx®-16) is spin-coated on the device and then converted to a 1-μm-thick SiO_2 cladding layer after one hour of annealing at 800 ˚C in an oxygen ambient. Metallic microheaters based on Ref. [50] (seen in Figure 5.2(b)) are later fabricated on top of the oxide cladding to form phase shifters using the strong thermo-optic property of Si. The power consumption of the fabricated microheaters is ~ 9–10 mW per π phase shift. It can be seen that the tunable coupler is a Mach-Zehnder interferometer (MZI) consisting of two fixed couplers and a tunable phase difference between the two arms (ϕ_{MZI}). The tunable coupling ratio κ^2 is given by

$$\kappa^2 = 4\gamma^2\left(1-\gamma^2\right)\cos^2\left(\frac{\phi_{MZI}}{2}\right), \tag{5.5}$$

where γ^2 is the power coupling ratio of each fixed coupler. The maximum of this term is 1, which only occurs at γ^2 = 0.5 and ϕ_{MZI} = 0. In practice, because of fabrication imperfections, it is difficult to reach this exact point. However, because of the symmetry in Eq. (3), we only need to cover the κ^2 range from 0 to 0.5. Limiting the available range to 0.5 instead of 1 also improves the accuracy of our device for a given voltage/current resolution at the driving circuit. We design the tunable coupler to have a coupling ratio slightly above 0.5 (i.e., 0.59) at ϕ_{MZI} = 0 using γ^2 = 0.82 (at the 1550 nm wavelength). The rationale behind this choice is that, with $4\gamma^2(1 - \gamma^2)$ being the maximum achievable coupling ratio and fabrication imperfections being present, it is safer to leave a margin of

error on the upside, which can be later corrected by applying the proper value of ϕ_{MZI}, rather than erring on the downside, which will make the $\kappa^2 = 0.5$ point unreachable.

Another coupler, functioning as an optical tap, is placed at the input to monitor the level of reflection, and the unused port of this coupler is terminated with a slow taper to minimize the level of extra reflection that the tap itself might produce. Figure 5.3(a) shows the power measured at the tap output (proportional to the reflected power at the input) as a function of the voltages applied to the tunable coupler and the phase shifter (denoted by V_κ and V_ϕ, respectively). The reflection hits the noise level (–40 dB) when $V_\kappa = 2.16$ V and $V_\phi = 1.4$ V. The laser wavelength is fixed at 1550 nm. Figure 5.3(a) clearly shows that a high degree of reflection suppression can be achieved using the proposed structure. By using other combinations of the control voltages, we can readjust the device to compensate for any changes in the output reflection. The device can also be used as a reconfigurable reflection controller with the ability to control both the amplitude and the phase of the reflection seen at the input port by using the proper combination of the control voltages.

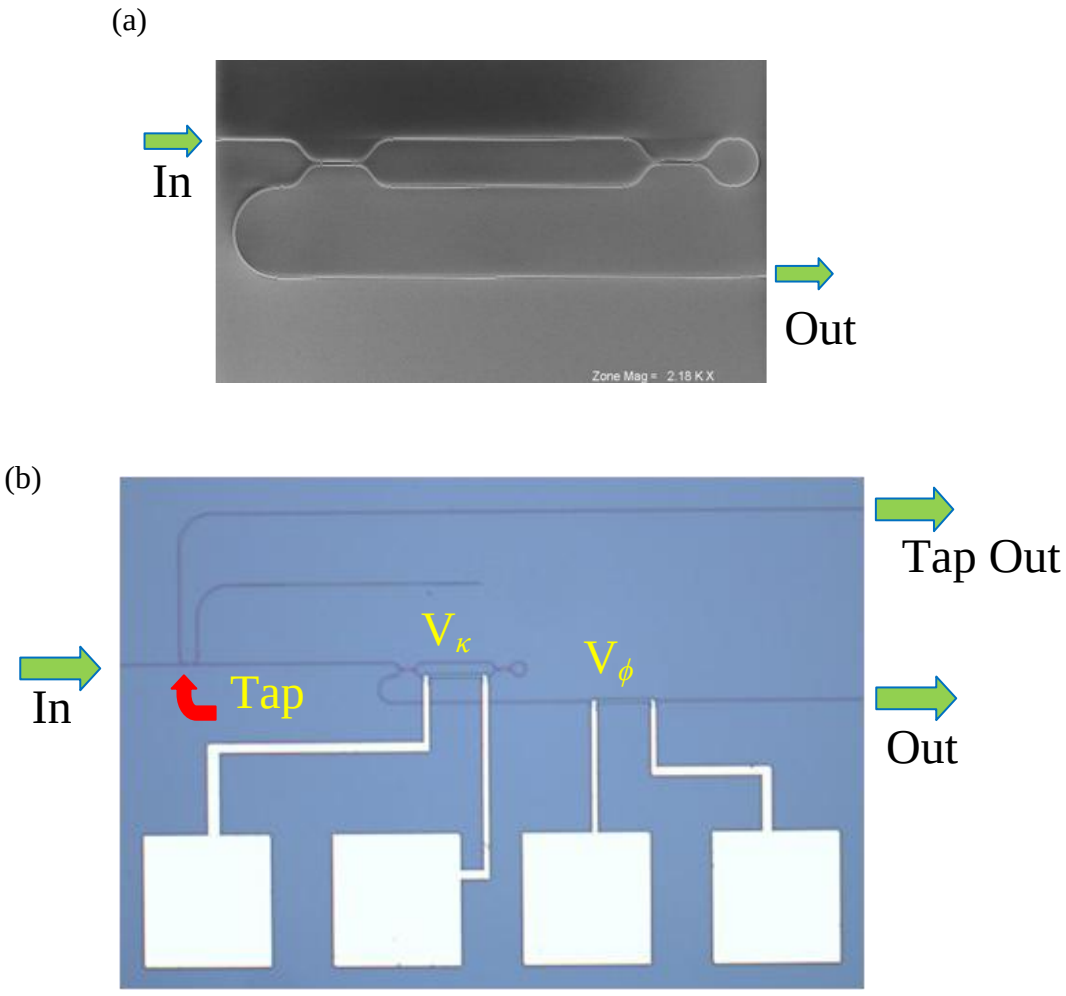

Figure 5.2. (a) SEM image of the tunable loop mirror. The device is 105 μm long. (b) Optical micrograph of the fabricated device with microheaters and contact pads.

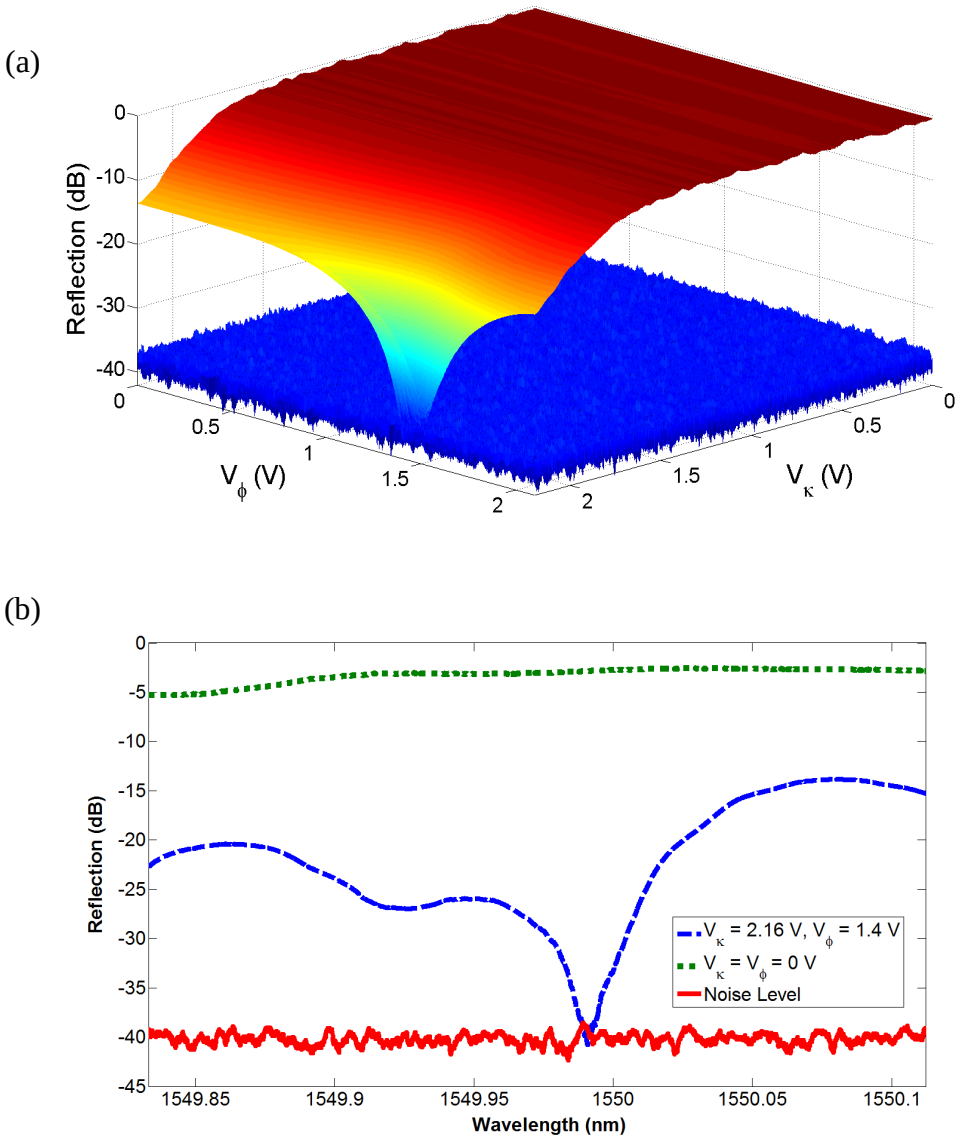

Figure 5.3. (a) Measured power at the tap output at 1550 nm as a function of the voltages applied to the tunable coupler and the phase shifter. The reflection hits the noise level (-40 dB) at V_κ = 2.16 V and V_ϕ = 1.4 V. (b) Blue, dashed curve: Measured power at the tap output versus the laser wavelength when V_κ = 2.16 V and V_ϕ = 1.4 V. The 20-dB suppression bandwidth is ~ 20.7 GHz. The red (full) curve is the noise level, and the green (dotted) curve is the power at the tap output when both voltages are zero.

5.4. Discussion

Figure 5.3(b) shows the power measured at the tap output as a function of wavelength (around 1550 nm) with V_κ = 2.16 V and V_ϕ = 1.4 V, and the same power when both voltages are zero. Similar to resonator-based devices, our device has a limited operation bandwidth, but for different reasons. One potential source of this limitation is the wavelength dependence of reflection, since the device must be reconfigured for each specific pair of $|r|$ and ϕ_r. If the reflected signal has a fairly wavelength-independent profile at the source of reflection, the limiting factor will be the wavelength-dependence of ϕ_{RT}. In this case, the x-dB reflection suppression bandwidth will be given by

$$\Delta f_{x-dB} = \frac{c}{4\pi L N_g}\Delta\phi_{x-dB}$$

$$= \frac{c}{\pi L N_g}\sin^{-1}\left(\frac{1-R}{2\sqrt{R}}\sqrt{\frac{10^{-x/10}}{1-10^{-x/10}}}\right), \tag{5.6}$$

where $\Delta\phi_{x-dB}$ is the (full-width) variation in ϕ_{RT} that will still keep the input reflection level below x dB, N_g is the effective group index of the waveguide connecting the reflection suppressor to the source of reflection, c is the speed of light, L is the distance between the reflection suppressor and the source of reflection, and $R = |r|^2$. The waveguide propagation loss is assumed to be negligible over the distance $2L$. As expected, the level of tolerance for frequency variation is inversely proportional to L. $\Delta\phi_{x-dB}$ is derived from Eq. (1) and depends on the magnitude of the reflection coefficient (but not its phase). With N_g = 4.2 (for a 450×220 nm^2 SOI waveguide) and L = 0.5 mm, Figure 5.4(a) shows the simulation results for the 20-dB reflection suppression bandwidth as a function of the power reflection coefficient at the output port. It can be seen that the

achievable bandwidth is larger for smaller values of the reflection coefficient. Figure 5.4(b) shows the simulation results for the 20-dB reflection suppression bandwidth as a function of *L*, when 30% of the output power is reflected (corresponding to the maximum reflection from a silicon-air termination). For lower levels of reflection, the curve shifts upward, thereby allowing for larger reflection suppression bandwidths for any given distance *L*, or alternatively, longer coverable distances at any given reflection suppression bandwidth.

In conclusion, we have demonstrated a compact, thermally reconfigurable reflection suppressor on SOI without reliance on non-reciprocal mechanisms. A reflection suppression ratio of 40 dB is achieved with a device footprint of 105 μm in length. This small footprint, in conjunction with a waveguide propagation loss of 5 dB/cm and the absence of excess loss, results in a total insertion loss below 0.15 dB. The operation bandwidth depends on the frequency dependence of the back reflection going into the suppressor, which is predominantly determined by the distance between the device and the source of reflection. A 20-dB reflection suppression bandwidth of 20.7 GHz was achieved in this work. The total power consumption for the two microheater elements is below 20 mW.

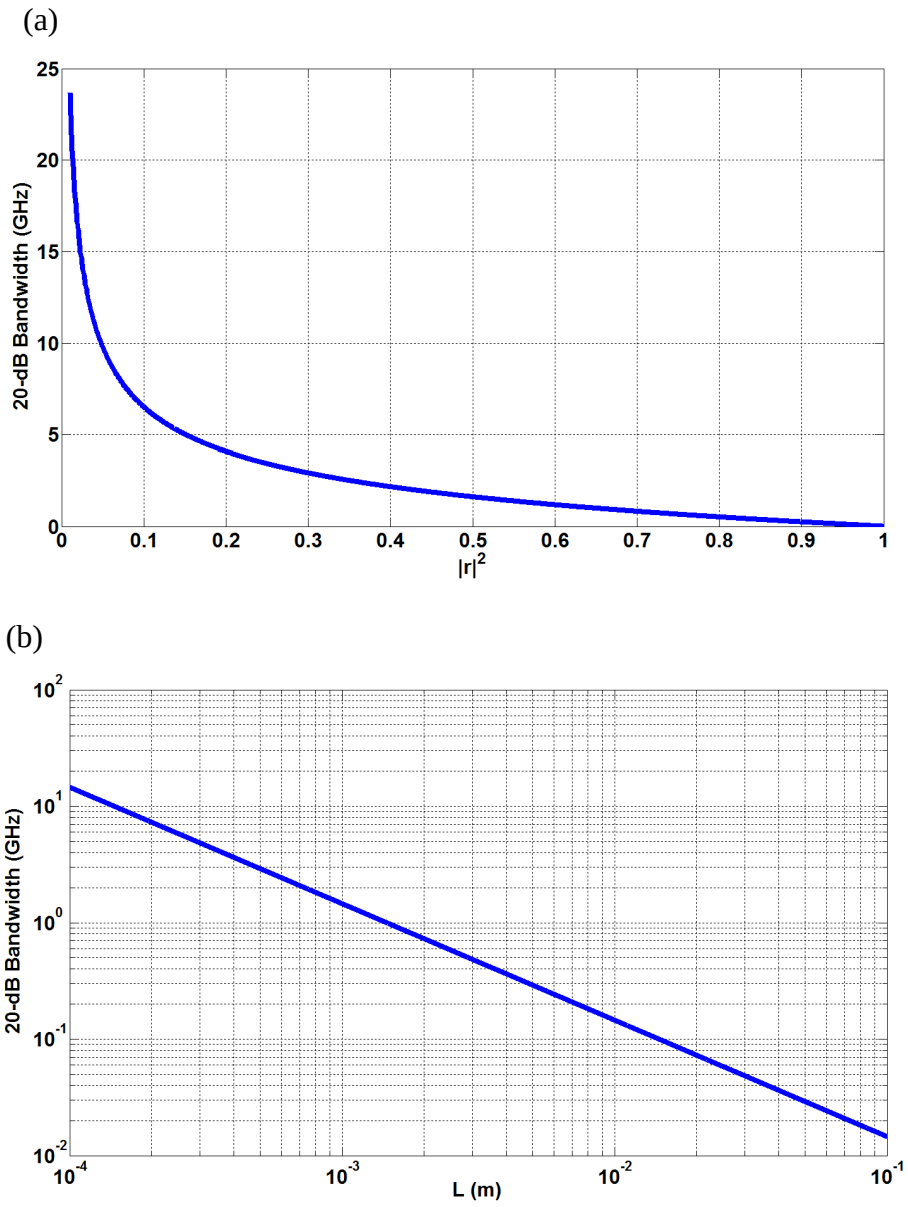

Figure 5.4. (a) Simulation results for the 20-dB suppression bandwidth as a function of the power reflection coefficient at the output port with N_g = 4.2 and L = 0.5 mm. (b) Simulation results for the 20-dB suppression bandwidth as a function of L, when 30% of the output power is reflected. The curve shifts upward for lower levels of reflection. Both axes are in logarithmic scale.

CHAPTER 6

AN INTEGRATED POLARIZATION CONTROLLER USING A RECONFIGURABLE 2×2 CELL ON SOI

In this chapter, we demonstrate an on-chip fiber-polarization controller (FPC) on SOI that is based on a fully reconfigurable 2×2 cell used in conjunction with a pair of identical, two-dimensional grating couplers for input and output coupling. This device can be used for the compensation of polarization rotation in fibers for polarization-mode multiplexing systems, as well as on-chip ellipsometry solutions.

The 2D grating coupler at the input performs the function of a polarization splitter by capturing the incoming light from a vertically coupled single-mode fiber (SMF), dividing it into its components along two perpendicular polarization axes, and coupling them into the TE modes of two identical 450×220 nm^2 SOI waveguides. A schematic of this process is shown in Figure 6.1(a) [64]. When used in a reverse configuration, the 2D grating coupler can act as a polarization combiner by collecting two inputs from the TE modes of two waveguides and coupling them into a fiber in the form of two perpendicularly polarized components [64]. The fully reconfigurable (amplitude and phase) 2×2 cell is capable of receiving two inputs from the input-side waveguides and generating a coherent, linear combination of them at a selected output with tunable, complex weighting coefficients. This allows us to realize any desired combination of relative phase and amplitude ratios for the two outputs going into the output grating coupler. Since any arbitrary elliptical polarization can be described by the relative phase and amplitude ratios of its two orthogonally polarized components [65], the combination

of the cell's two outputs inside the output fiber can have any desired elliptical polarization. Therefore, the device as a whole can convert any arbitrary input polarization to any desired polarization at the output.

The design and implementation of the building blocks will be discussed in Section 6.1, followed by the simulations and experimental results related to the device as a whole, which will be presented in Section 6.2.

6.1. Design, Simulation, and Characterization of the Building Blocks

6.1.1. Grating Couplers

The design of the 2D grating couplers was based on Ref. [66], and their fabrication was performed with an HSQ-based process similar to the one used in the previous chapters. The only difference was the need for a two-step plasma etching procedure, which results from the fact that the 2D photonic-crystal structure at the core of the coupler has a hole depth of 90 nm, while the etch depth for fabricating the ridge waveguides is equal to the SOI device layer thickness (i.e., 220 nm). This was accomplished by using the SPR 220-7.0 positive photoresist for masking the photonic-crystal structure during the second step of Si etching. Figures 6.1(b) and (c) respectively show a close-up and a zoom-out SEM of the 2D grating coupler with the attached waveguides. Light that is polarized along the 45/–45 ° axis will be coupled into the lower/upper input waveguide, which results in

$$\tilde{\mathbf{E}}_{i1} = (\tilde{\mathbf{E}}_y - \tilde{\mathbf{E}}_x)/\sqrt{2}, \tag{6.1}$$

and

$$\tilde{\mathbf{E}}_{i2} = (\tilde{\mathbf{E}}_y + \tilde{\mathbf{E}}_x)/\sqrt{2}, \tag{6.2}$$

where the positive *y* direction is the reference for determining the sign of the electric field inside the waveguides. Similarly, at the output:

$$\tilde{\mathbf{E}}_x = (\tilde{\mathbf{E}}_{o1} - \tilde{\mathbf{E}}_{o2}) \Big/ \sqrt{2}\,, \tag{6.3}$$

and

$$\tilde{\mathbf{E}}_y = (\tilde{\mathbf{E}}_{o1} + \tilde{\mathbf{E}}_{o2}) \Big/ \sqrt{2}\,. \tag{6.4}$$

We also developed a one-dimensional grating coupler based on Ref. [67] in order to be able to test a single input or output channel independently. This was necessary for the characterization of the building blocks before fabricating the final FPC device. An SEM of this 1D grating coupler is shown in Figure 6.1(d). The grating is capable of coupling the TE mode of the waveguide into the *y*-polarized mode of an SMF, and vice versa.

Our measurements showed a maximum extinction ratio of ~ 30 dB between the two arms of the 2D grating coupler. The results of this measurement can be seen in Figure 6.1(e).

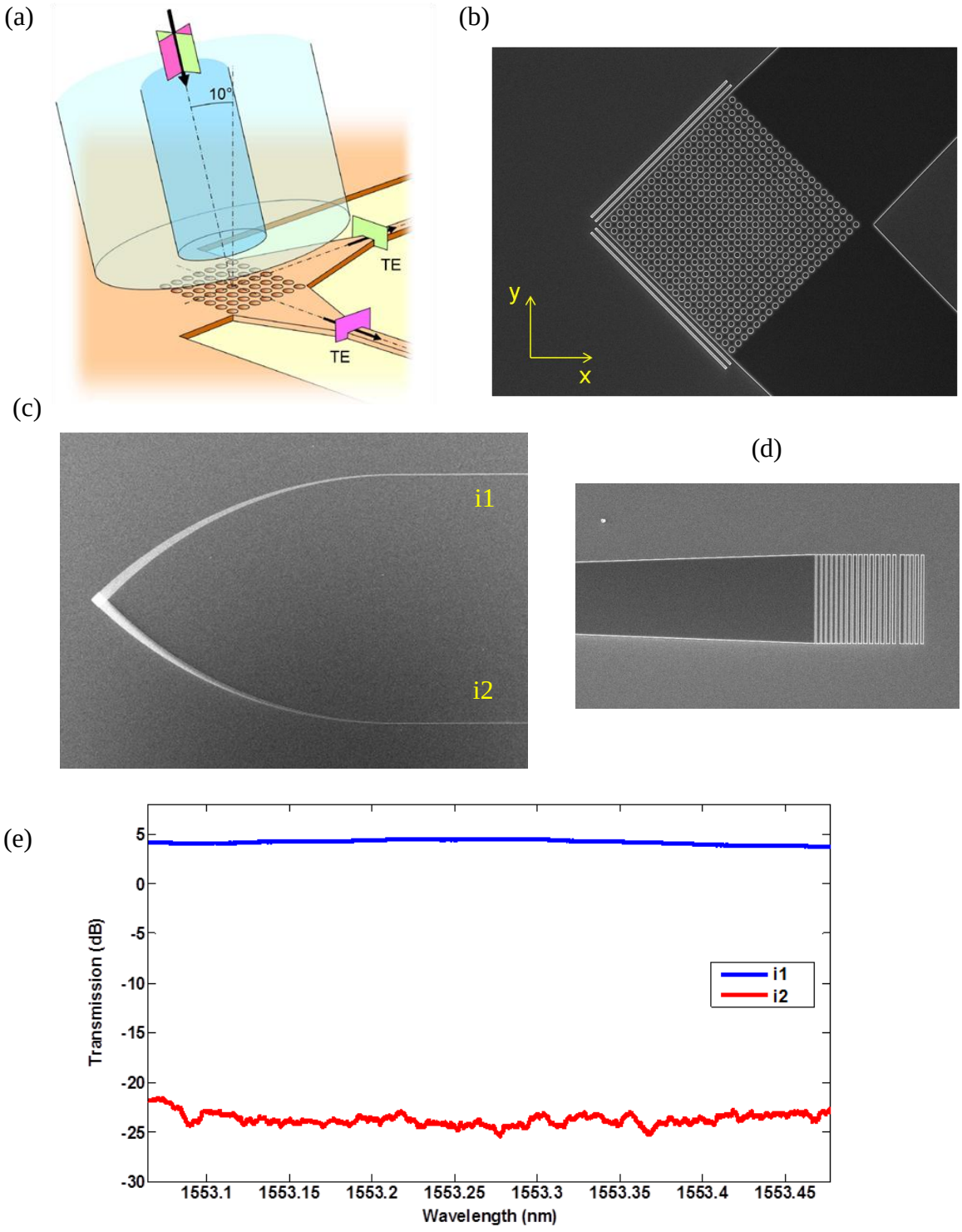

Figure 6.1. (a) Schematic of the polarization splitting process using the 2D SOI grating coupler (from Ref. [64]). (b) Close-up, and (c) Zoom-out SEMs of the 2D grating coupler. (d) SEM of the 1D grating coupler. (e) Measurement results showing an extinction ratio of ~ 30 dB between the two arms of the 2D grating coupler

6.1.2. Reconfigurable 2×2 Cell

Figure 6.2(a) shows a zoom-out SEM of the reconfigurable 2×2 cell. It also shows how the cell is used in conjunction with the 2D grating couplers in order to form a polarization converter. Figure 6.2(b) shows a close-up SEM of the cell along with the positions of the microheaters that will later be fabricated on top of the cladding covering the device. The cell consists of a racetrack resonator that is coupled on each side to one of the two input waveguides. The coupling is achieved through a thermally tunable MZI coupler similar to the one discussed in Section 5.3, with the difference that γ^2 is designed to be 0.5 so that the tunable coupler will have a 100% coupling ratio when $\phi_{MZI} = 0$. H2 and H4 are used to set the coupling ratio through changing ϕ_{MZI}. The racetrack resonator, with a wavelength-domain FSR of 4.5 nm (~ 570 GHz) at 1.55 μm, enables us to use the device on a frequency-selective basis. The microheater labeled H3 enables us to shift the resonance of the racetrack to the desired frequency, and also to compensate the unwanted shifts in resonance resulting from the phase effects of the tunable couplers. H1 can be used to adjust the initial phase difference between the two inputs, while H5 is used to set the relative phase of the two outputs.

Figures 6.3(a) and (b) respectively show the simulated power transmission of the cell at o1 and o2 as a function of the phase shifts applied to H2 and H4, when the two inputs are in-phase and have equal power (both $1/\sqrt{2}$), and the racetrack is at resonance (with $m = 195$) when no current is applied H2 or H4 (i.e., at the origin of the plot). The simulations are performed with the assumption that the waveguides and couplers are all lossless. The addition of loss does not alter the operation principle of the device in any

significant manner. Choosing an even *m* instead of an odd one will result in the swapping of the transmission characteristics between o1 and o2.

Figure 6.4(a) shows the difference in the simulated power transmissions of o1 and o2 from Figure 6.3. Since the sum of the power transmissions in the lossless case always equals 1, the fact that the difference in transmissions shown in Figure 6.4(a) covers the full range from –1 to 1 demonstrates that any desired amplitude ratio between the two outputs can be realized by applying the proper combination of phase shifts (between 0 and π) to H2 and H4. However, applying these phase shifts will alter the relative phase of the two outputs, as seen in Figure 6.4(b). This resulting phase difference can be changed to the target value (based on the desired output polarization) by using H5.

It must be noted that if the inputs to the cell are not in-phase, the 0–π range for H2 and H4 will not suffice for achieving any desired amplitude ratio between the two outputs, as shown in Figure 6.5(a) for the case of an initial relative phase of $\pi/2$ between the inputs. However, as noted earlier, H1 can be used to compensate for any such differences in phase.

Another noteworthy point is that the ability to cover the full range of amplitude ratios between the two outputs is not limited to the case when the inputs have equal power. For example, Figure 6.5(b) is the equivalent of Figure 6.4(a) for the case when the input power is divided between i1 and i2 at 10% and 90%, and shows a similar full range from –1 to 1 on its *z* axis.

(a)

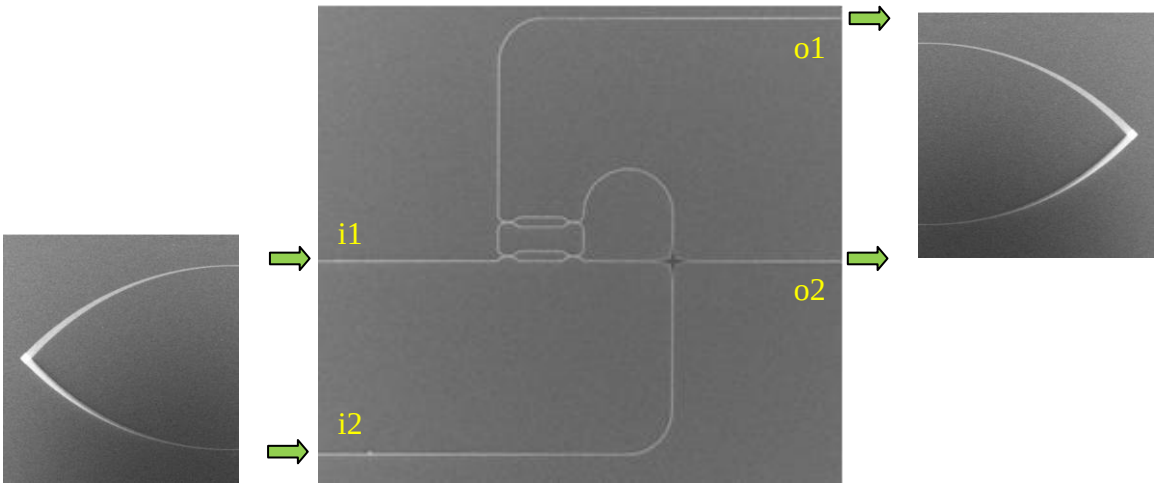

(b)

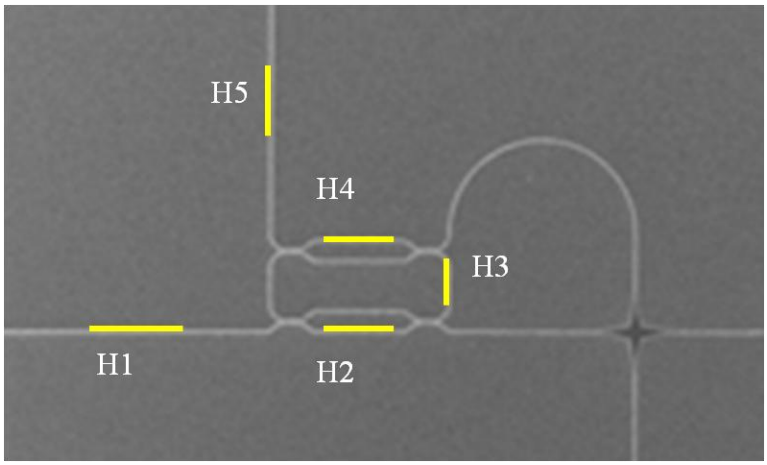

Figure 6.2. (a) Close-up, and (b) Zoom-out SEMs of the reconfigurable 2×2 cell. (a) also shows how the cell is used in conjunction with the 2D grating couplers in order to form a polarization converter. (b) also shows the positions of the microheaters (H1–H5) that will later be fabricated on top of the cladding covering the device.

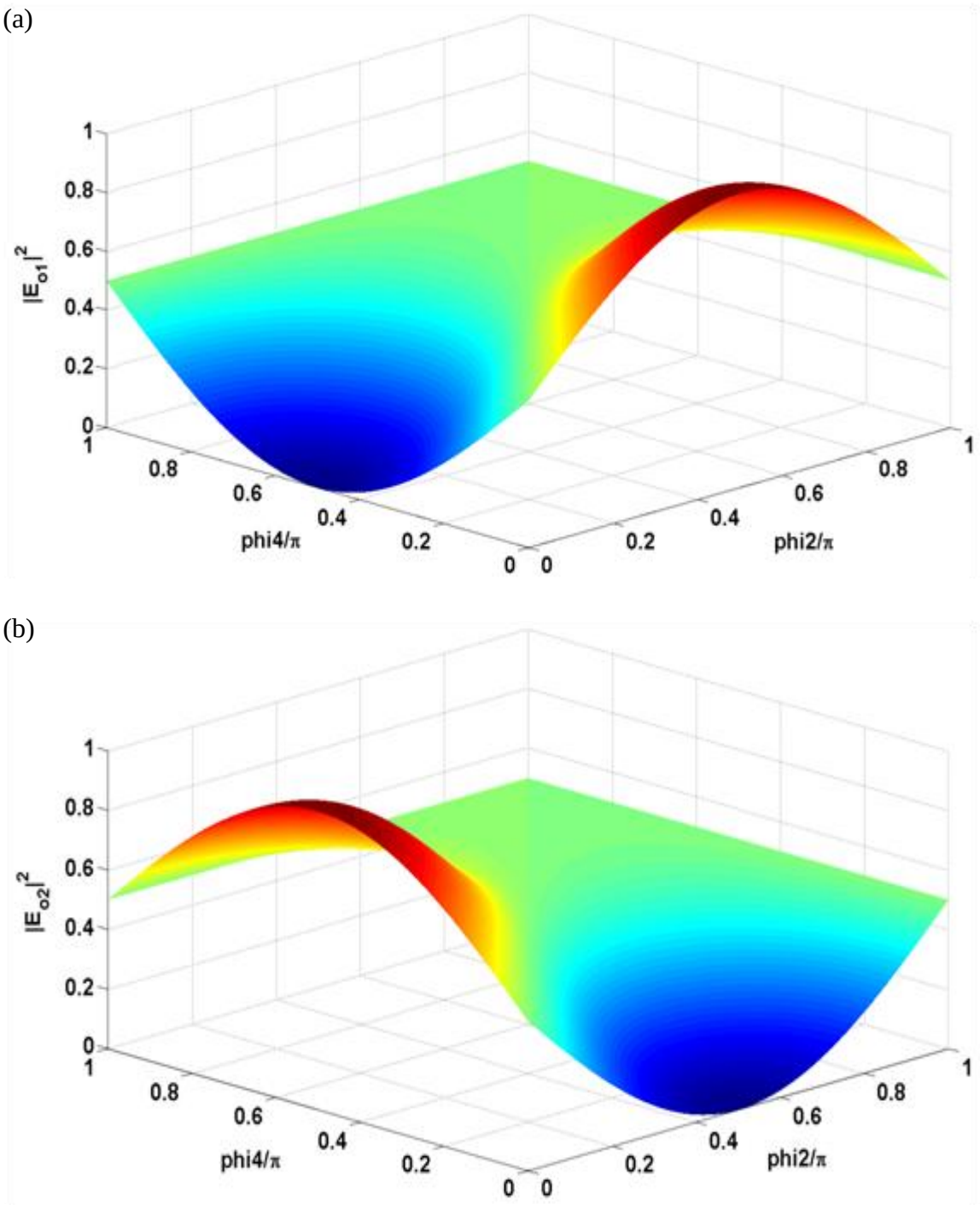

Figure 6.3. Simulated power transmission of the 2×2 cell at (a) o1, and (b) o2 as a function of the phase shifts applied to H2 and H4, when the two inputs are in-phase and have equal power (both $1/\sqrt{2}$), and the racetrack is at resonance (with m = 195) at (0,0). The device is assumed to be lossless.

(a)

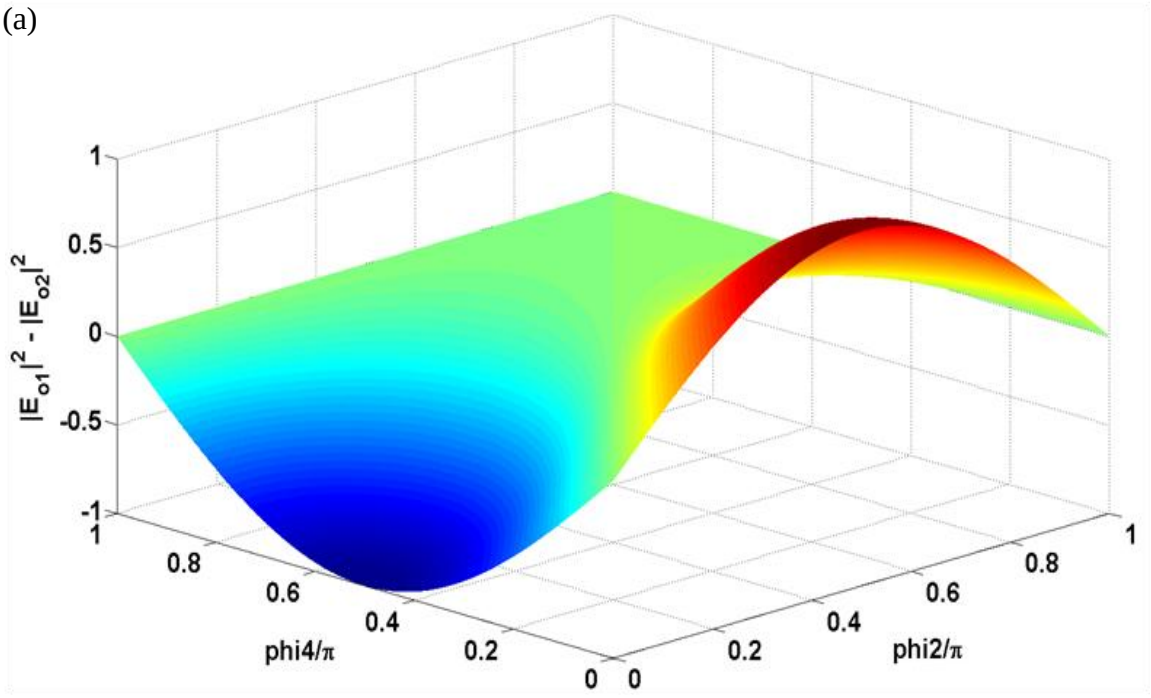

(b)

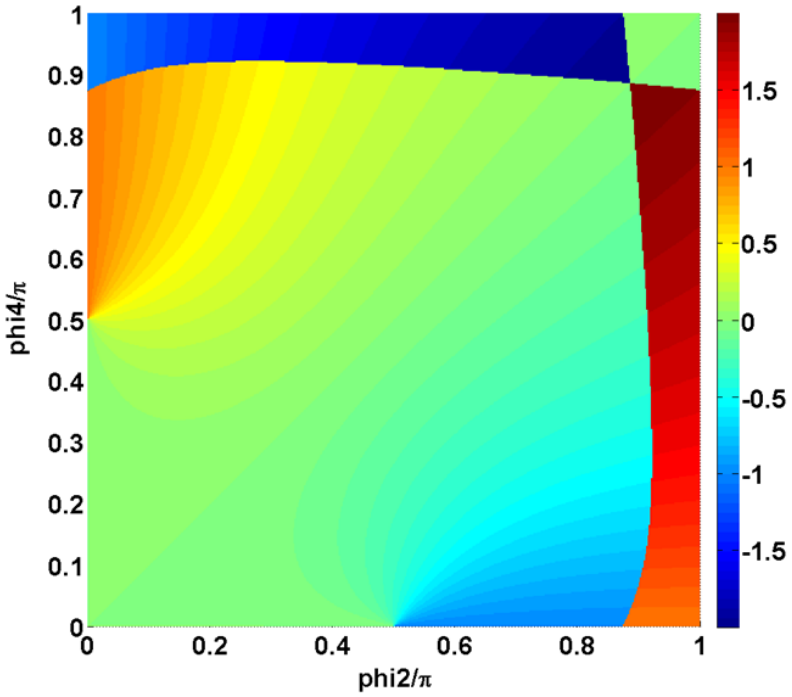

Figure 6.4. Differences in (a) power transmission, and (b) phase (divided by π) between o1 and o2 as a function of the phase shifts applied to H2 and H4, when the two inputs are in-phase and have equal power (both $1/\sqrt{2}$), and the racetrack is at resonance (with m = 195) at (0,0). The device is assumed to be lossless.

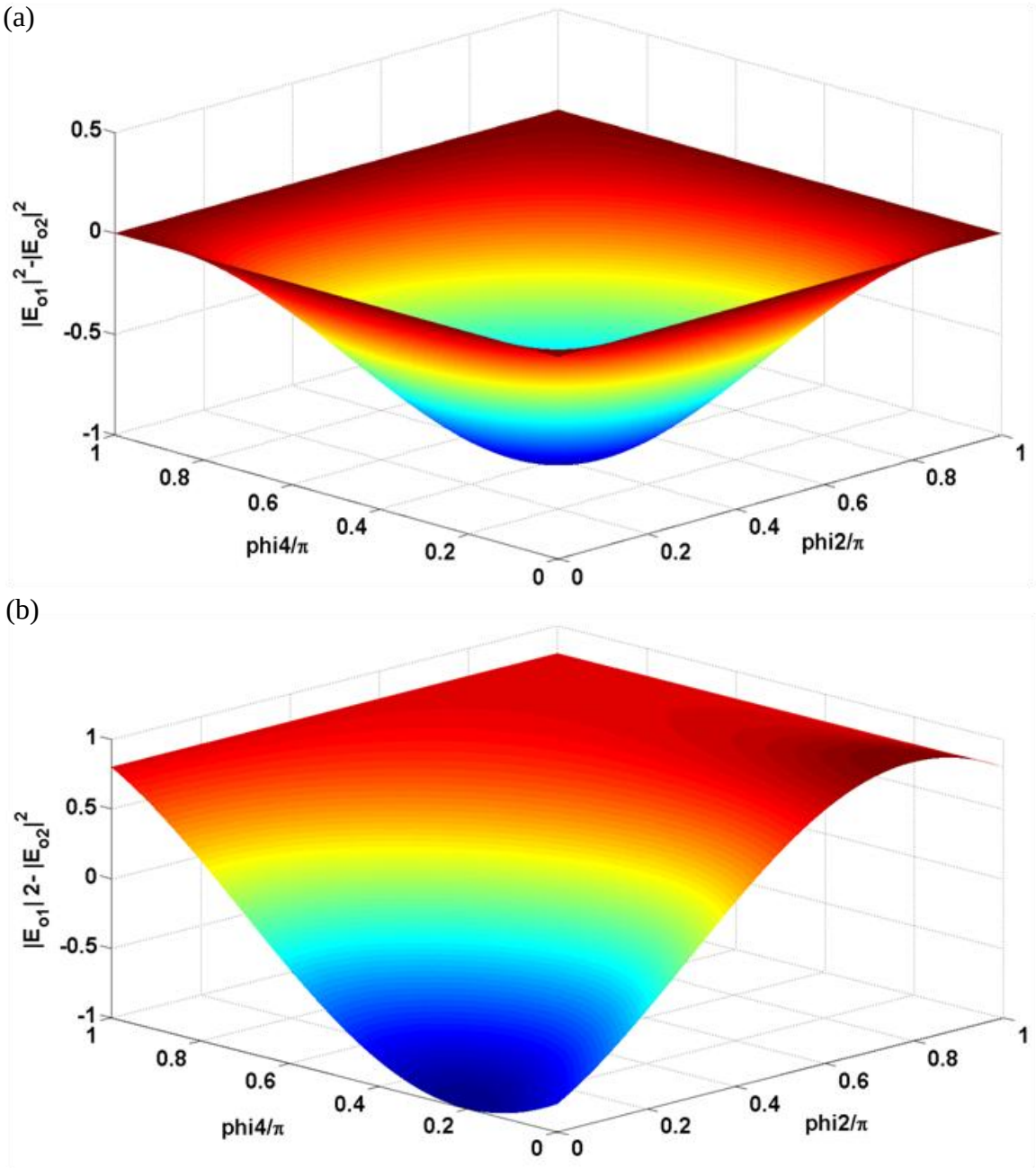

Figure 6.5. (a) Difference in power transmission between o1 and o2 as a function of the phase shifts applied to H2 and H4, when the two inputs have equal power (both $1/\sqrt{2}$), and the i1 input has a phase delay of $\pi/2$ with respect to the i2 input. (b) Difference in power transmission between o1 and o2 as a function of the phase shifts applied to H2 and H4, when the two inputs are in-phase, and the total input power is divided between them at 10% and 90%. For both (a) and (b), the racetrack is at resonance (with m = 195) at (0,0), and the device is assumed to be lossless.

If only one of the two inputs is active, it must be possible to route this input to its cross output by leaving both tunable couplers at 100%, or direct it to the through output by setting at least one of the coupling ratios to zero (i.e., $\phi_{MZI} = \pi$). Figures 6.6 and 6.7 show measurement results that confirm this conclusion. Figure 6.6 shows the power measured at the o2 output as a function of the voltages applied to H2 and H4, when the power in the i2 input is zero. As expected, the result is very similar to Figure 6.5(b).

Figure 6.7(a) shows the measured power transmission of port o2 as a function of wavelength, when the power in the i2 input is zero, and the tunable couplers are set to either 0 or 100% by using the proper combination of V2 and V4 derived from Figure 6.6. The measurement points correspond with the four corners of Figure 6.6. Figure 6.7(b) shows the results of a similar measurement performed at the opposite port (o1).

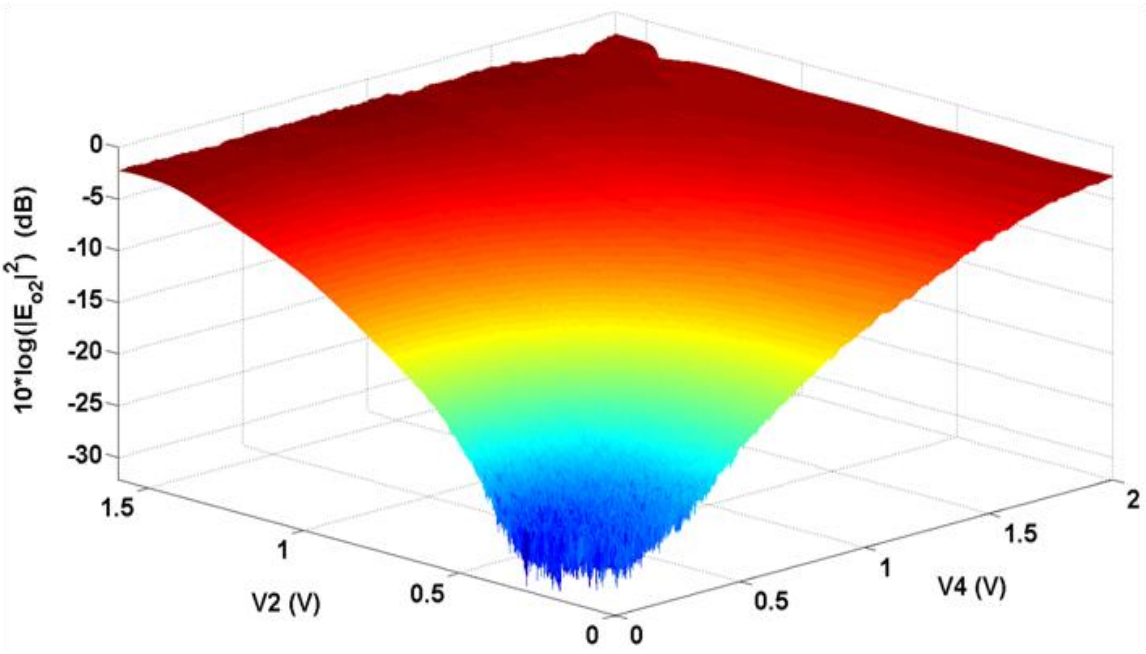

Figure 6.6. Optical power measured at the o2 output as a function of the voltages applied to H2 and H4, when the power in the i2 input is zero.

(a)

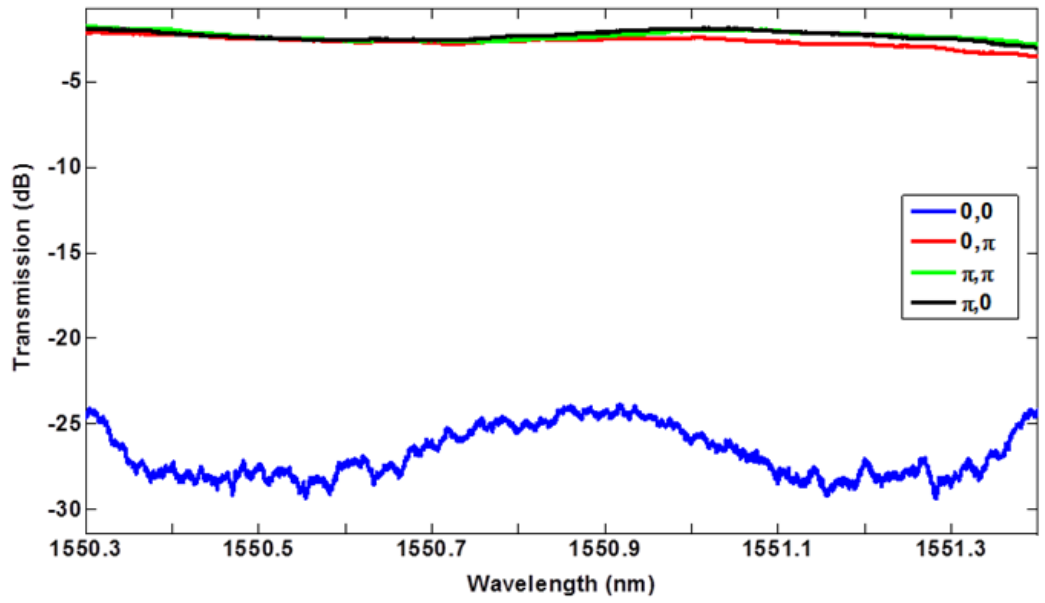

(b)

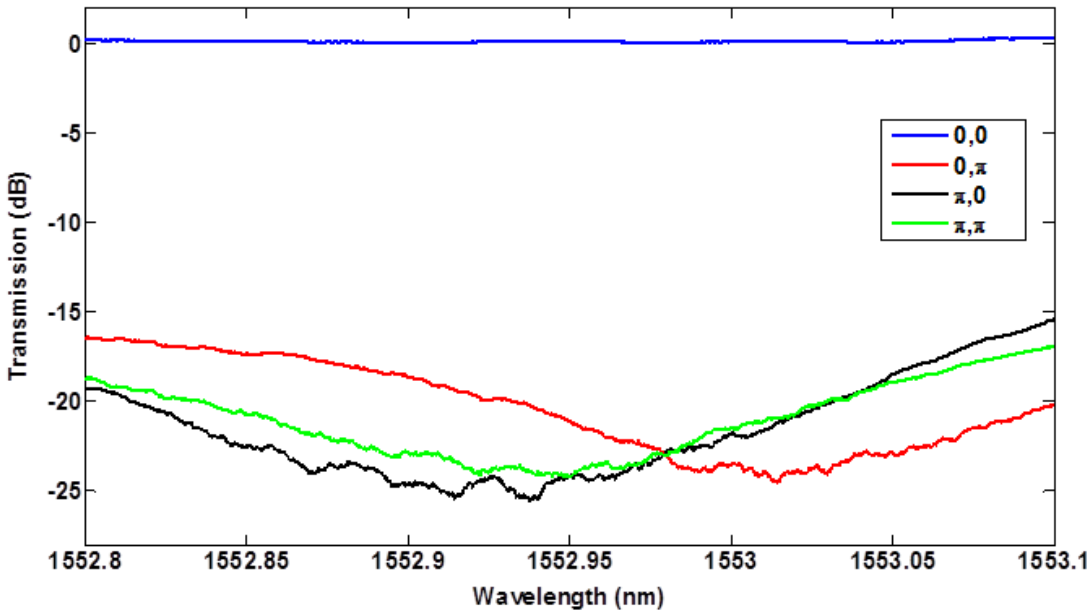

Figure 6.7. (a) i1–o2, and (b) i1–o1 power transmission measured as a function of wavelength, when the power in the i2 input is zero, and the tunable couplers are set to either 0 (ϕ_{MZI} = π) or 100% (ϕ_{MZI} = 0) by using the proper combination of (phi2,phi4). The measurement points correspond with the four corners of Figure 6.6.

6.2. Integrated Polarization Controller

6.2.1. Simulation

We developed a constrained optimization code to calculate the required phase shifts for any polarization conversion from a specified input state to a desired output state. The results for a few select cases are shown in Table 6.1. The reference axes for the depicted polarizations are all in accordance with Figure 6.1 (b). The presented results are not the sole possible solutions, but rather those that are derived with the procedure described in Subsection 6.1.2.

Input Polarization State	phi1	phi2	phi4	phi5	Output Polarization State
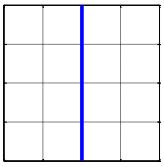	0	0	0	π	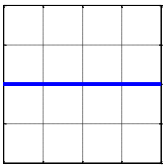
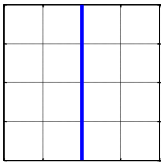	0	π/2	0	0	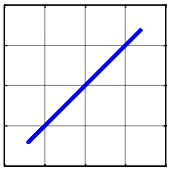
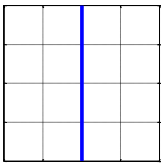	0	0	0	π/2	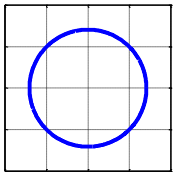

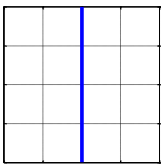	0	3π/4	0	3π/2	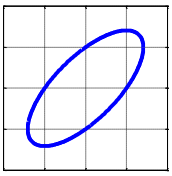
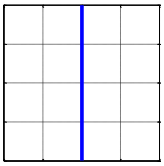	0	0	0	π/4	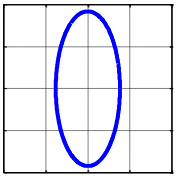
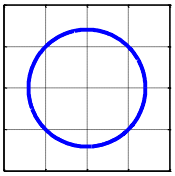	π/2	π/2	0	0	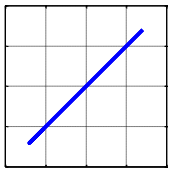
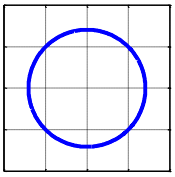	π/2	0	π/4	π/2	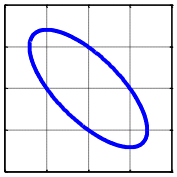
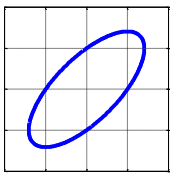	π/2	0	π/2	3π/2	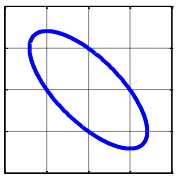
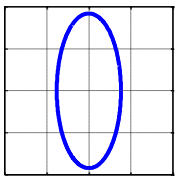	π/4	0	3π/4	3π/2	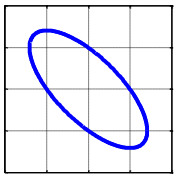

Table 6.1. Required phase shifts (from H1, H2, H4, and H5) for select cases of polarization conversion. The nonlinear polarizations considered are all CCW. The reference axes for the depicted polarizations are all in accordance with Figure 6.1 (b).

6.2.2. Experimental Results

For polarization-state measurements, the output from the device is fed into a fiber collimator, followed by a manually rotatable free-space polarizer and a free-space detector. The collimator converts the SMF mode into a free-space beam that is filtered by the polarizer. Three consecutive intensity measurements are made at three polarizer angles (0 ˚, 45 ˚, and 90 ˚) in order to determine the output polarization state. The input polarization state is assumed to be the polarization of the input fiber on the chip with respect to the *x*–*y* axes shown in Figure 6.1(b) and is determined by studying its coupling to a 1D or 2D grating coupler on the chip. The output polarization is also defined with respect to the same axes. Polarization measurement results with the corresponding heater signals are shown in Table 6.2.

Input Polarization State	I1	I2	I4	I5	Output Polarization State
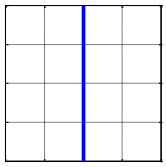	6 mA	0	0	0	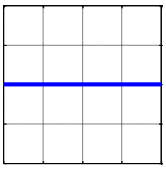
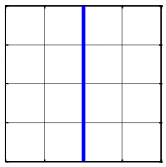	0	0	0	6 mA	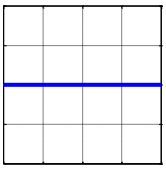
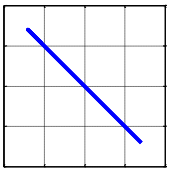	0	0	0	0	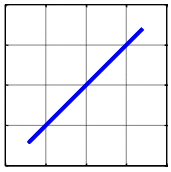
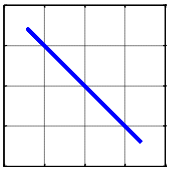	0	12.8 mA	0	0	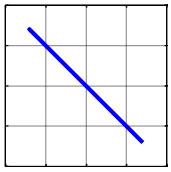
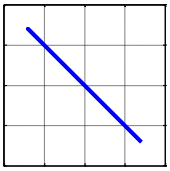	0	0	12.8 mA	0	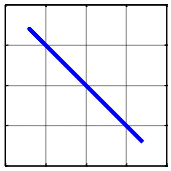

Table 6.2. Experimental polarization conversion results. I1–5 are the currents applied to the microheaters H1–5.

CHAPTER 7

TOPICS IN SOI INTEGRATED PHOTONICS IMPLEMENTATION

In this chapter, we present solutions to several practical challenges that are faced in the design and fabrication of SOI PLCs. Each of these solutions is discussed in a separate section.

7.1. Wideband TM Suppression with Metallic Absorbers

Undesired polarization conversion is a potentially problematic issue in practical PLCs. For example, the presence of roughness on the sidewalls of waveguides can couple the TE mode into TM in a PLC that is designed for TE light, and vice versa. If an SOI PLC is designed for operation in the TE mode, the underlying Si substrate below the BOX layer can act as a natural suppressor of the TM mode without any need for modifying the bus waveguide geometry, and therefore help preserve the polarization purity of light throughout the PLC to a certain degree. The reason for this phenomenon is that for the standard 450×220 nm^2 SOI bus waveguide, the TM mode is less confined in the vertical direction than the TE mode, and therefore experiences a stronger coupling to the radiation modes of the Si substrate. It can be expected that the thinner the BOX layer, the stronger this radiation loss will be. We use the COMSOL 4.3b Wave Optics Module with built-in PML to derive the numerical values of this loss for TE and TM modes under various circumstances. The simulation window for the 1-μm-BOX, 1-μm-cladding case is shown in Figure 7.1(a), and the electric field norm for the TE and TM solutions is shown, respectively, in Figures 7.1(b) and (c). The imaginary component of the effective index determines the propagation loss. The loss values for the TE and TM modes are, in order,

0.0168 dB/cm and 20.8 dB/cm for the 1-μm-BOX case, and 0.0001 dB/cm and 0.237 dB/cm for the 3-μm-BOX case (both cases with a 1-μm-thick oxide cladding).

(a)

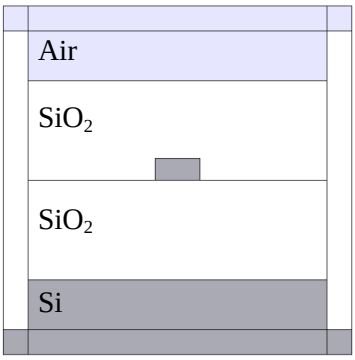

(b)

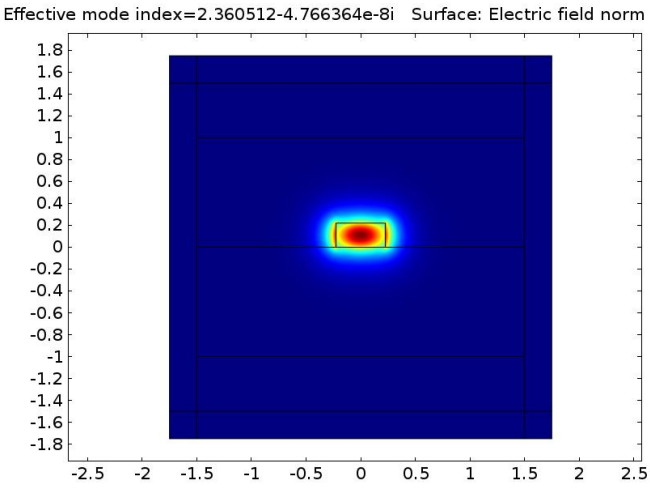

(c)

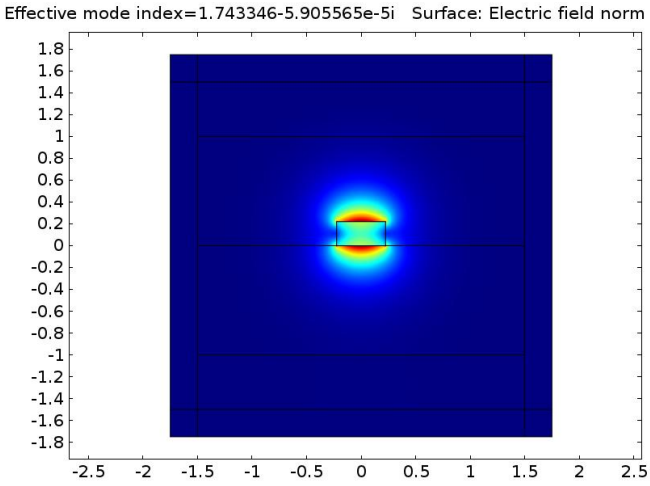

Figure 7.1. (a) Schematic of the simulation window for a 1-μm-BOX, 1-μm-cladding SOI waveguide with PML. Cross-sectional profiles of the electric field norm are shown for (b) the fundamental TE, and (c) the fundamental TM solution of a 450×220 nm^2 waveguide.

TM suppression can also be achieved by placing a lossy metallic layer on top of the protective cladding layer that is deposited on the device after patterning and etching. The TM mode will be more strongly affected by the presence of the metal than the TE mode, for the same reason that it is more strongly affected by the underlying Si substrate. This configuration can result in a much higher degree of suppression, and unlike the wafer BOX thickness, the metal and cladding thicknesses can be controlled through the fabrication process. The metallic film can be grown selectively (through a deposition and lift-off process) at specific spots on the chip in order to polarize the light as desired. The final benefit provided by this type of polarizer is its wideband operation.

Table 7.1 shows the refractive indices, as well as permittivities and skin depths of 10 commonly deposited metals at the 1.55 μm wavelength (data from Refs. [68,69]). From this data, we can divide these metals into three broad categories: those with a large n_i and a small n_r (such as Au, Ag, Cu, and Al), which result in a small skin depth and a large (negative) ε_r; those with moderate n_i and n_r values that are close in value (such as Ti, Cr, and W), which result in a larger skin depth and a small negative ε_r; and those that can be considered to lie in between (such as Ni, Pt, and Pd). It is noteworthy that Au, Ag, and Cu are all from an identical chemical group; the same is true of Ni, Pt, and Pd; as well as Cr and W. The simulated TE and TM loss values for each group are shown as a function of the metal layer thickness in separate plots in Figures 7.2 – 7.4 (all cases simulated with a 3-μm BOX).

Metal	Refractive Index at 1.55 μm	ε_r	ε_i	$\varepsilon_i/\varepsilon_r$	Skin Depth (nm)
Au	$0.38 - j10.75$	–115.4	8.17	0.071	22.9
Ag	$0.47 - j9.32$	–86.6	8.76	0.101	26.5
Cu	$0.757 - j10.365$	–106.9	15.7	0.147	23.8
Al	$1.44 - j16.0$	–253.9	46.1	0.182	15.4
Pd	$2.958 - j8.356$	–61.1	49.4	0.809	29.5
Ni	$3.10 - j7.74$	–50.3	48.0	0.954	31.9
Pt	$5.31 - j7.04$	–21.4	74.8	3.495	35.0
Ti	$3.685 - j4.618$	–7.75	34.0	4.39	53.4
Cr	$3.667 - j4.193$	–4.13	30.8	7.46	58.8
W	$2.22 - j4.85$	–18.6	21.5	1.156	50.9

Table 7.1. Refractive index, permittivity, and skin depth data at 1.55 μm for 10 commonly deposited metals.

(a)

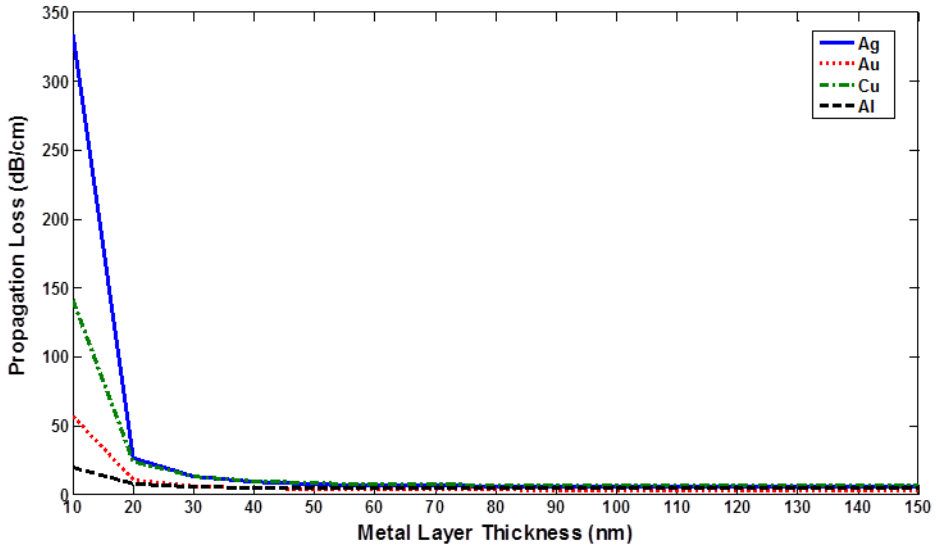

(b)

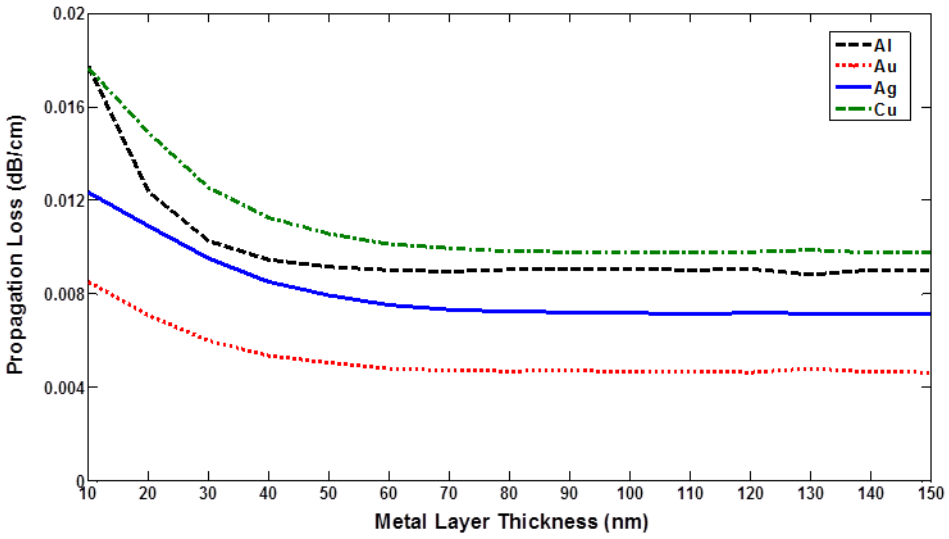

Figure 7.2. Simulation results for (a) TM, and (b) TE propagation loss as a function of the metal layer thickness at the 1.55 μm wavelength for Au, Ag, Cu, and Al.

(a)

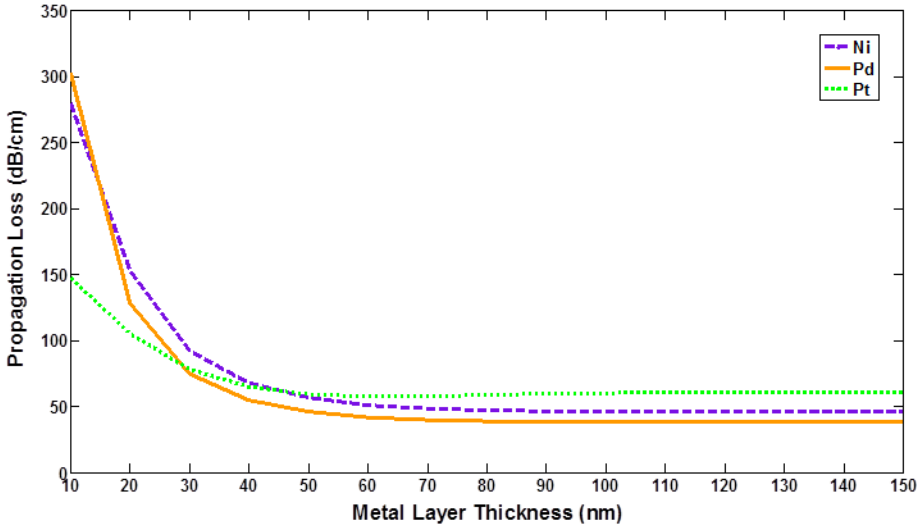

(b)

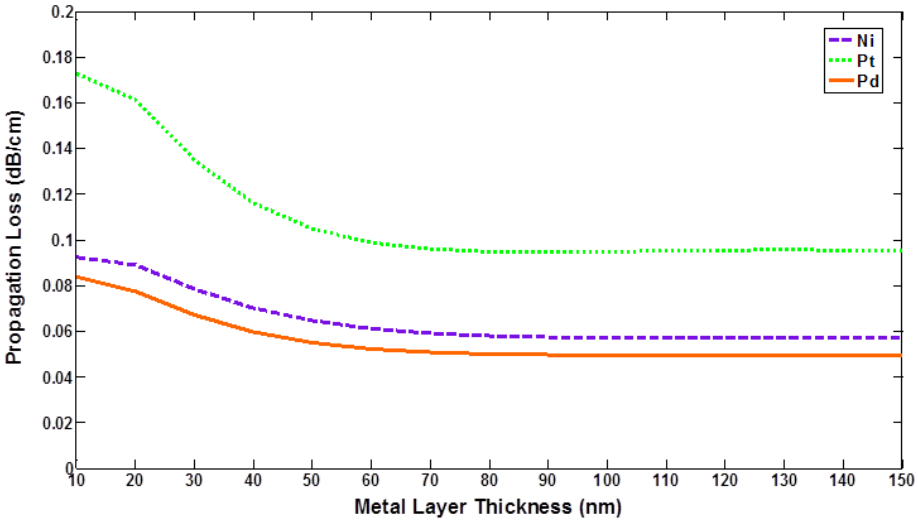

Figure 7.3. Simulation results for (a) TM, and (b) TE propagation loss as a function of the metal layer thickness at the 1.55 μm wavelength for Ni, Pt, and Pd.

(a)

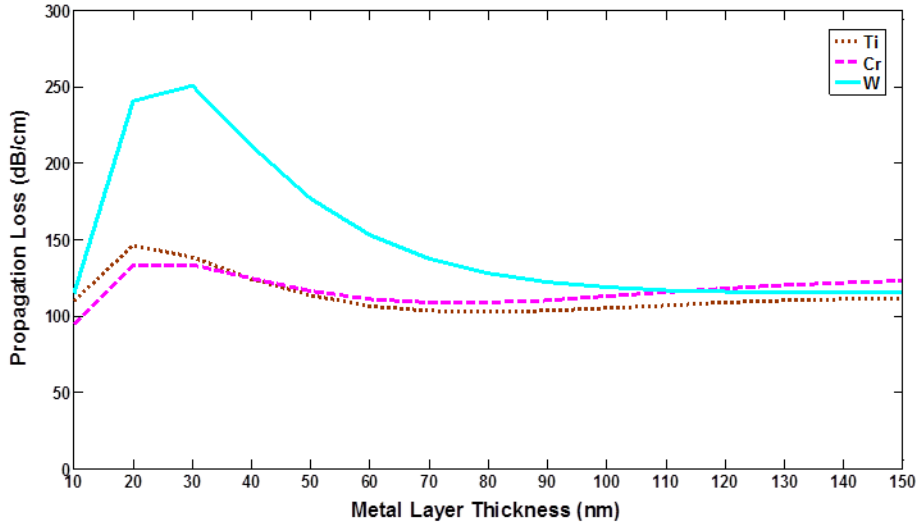

(b)

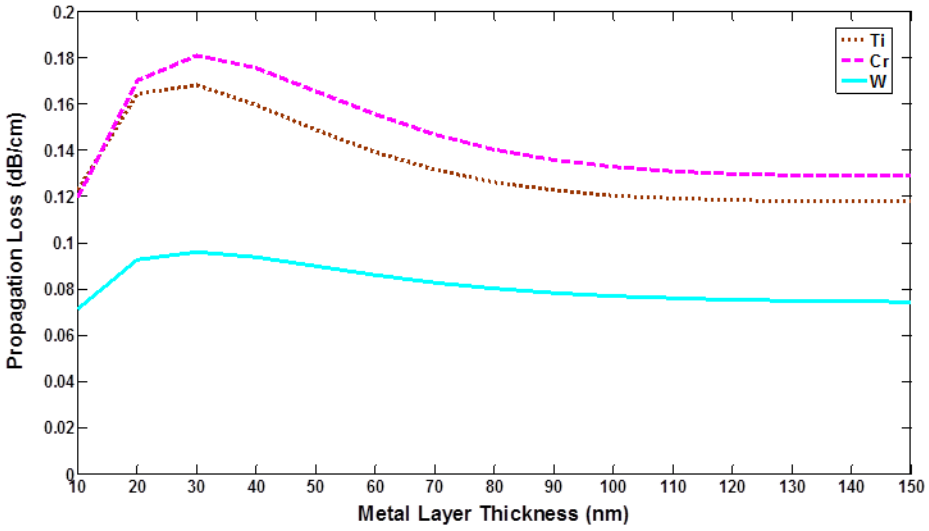

Figure 7.4. Simulation results for (a) TM, and (b) TE propagation loss as a function of the metal layer thickness at the 1.55 μm wavelength for Ti, Cr, and W.

As it is evident from Figures 7.2 – 7.4, the TE loss values for all metals at all thicknesses are very low and quite close to each other, while the TM loss shows a distinct behavior for each group. The first group show low TM loss values for thicknesses above the skin depth, followed by a very sharp increase in loss for thicknesses below the skin depth. The reason behind this phenomenon is an abrupt increase in the field confinement inside the metallic region when the metal is sufficiently thin to allow the field to "tunnel through". The second group show a roughly similar behavior, but the plasmonic transition is much more smooth, and the loss values at higher thicknesses are considerable. Finally, the third group show very high TM loss values at all thicknesses, with the peak occurring at around half the skin depth. Since the goal is to achieve a high TM loss while having as little an effect as possible on the TE mode, Tungsten clearly shows the best performance for most thicknesses among the latter group.

The logarithmic ratio of the guided TE mode power to that of the TM mode after any propagation length can be derived by subtracting the TE propagation loss from the TM propagation loss (in dB). The results of this calculation for all studied metals are shown in Figure 7.5. Since the TE loss values are small, the conclusions derived from this figure are not different from those arrived at by looking at the preceding TM plots only.

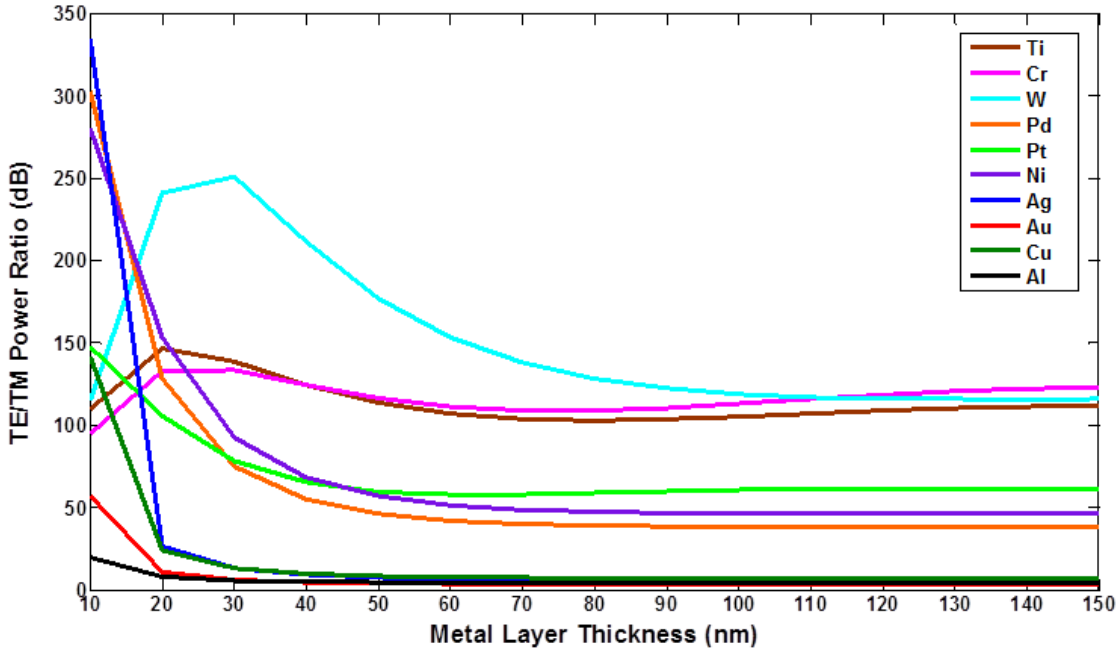

Figure 7.5. Simulated ratio of the guided TE mode power to that of the TM mode after any propagation length for all studied metals.

7.2. High-*Q* Microresonator Fabrication Using Low-Current E-Beam Lithography

As mentioned earlier, the major source of loss in our TWRs is surface scattering loss. Studies show that EBL with lower currents results in lower sidewall roughness [70]. Therefore, we can take advantage of this technique to increase the intrinsic *Q*s of fabricated TWRs. In order to confirm the effect on sidewall roughness, we fabricated a waveguide with an abrupt transition in the lithography current from 2 nA to 100 pA. Since this was done during a single lithography run, and all of the other fabrication steps were the same, any differences in sidewall roughness must be the result of the change in the lithography current. Figure 7.6(a) shows an SEM of the abrupt transition, and the change in sidewall roughness is clearly visible in this figure. We fabricated two sets of 20-μm-radius microdisks with identical processes except for the lithography current, which was 2 nA for one set and 100 pA for the other. The results of *Q* characterization for these two sets are shown in Figures 7.6(b) and (c), respectively. The comparison of extinction in high- and low-power characterizations determines the coupling regime, which is found to be over-coupling in both cases. The feature in Figure 7.6(b) has an intrinsic *Q* of ~ 700,000, while the feature in Figure 7.6(c) demonstrates an intrinsic *Q* of ~ 1.1 million. This corresponds to an increase of ~ 60% achieved by lowering the lithography current by a factor of 20. Lowering the lithography current has the disadvantage of increasing the write time; however, microresonators usually occupy a small fraction of the total pattern area, and it is not necessary to write the entire pattern with a low current. Thus, the problem of write time can be resolved by employing a dual-current lithography technique, as in Figure 7.6(a).

(a)

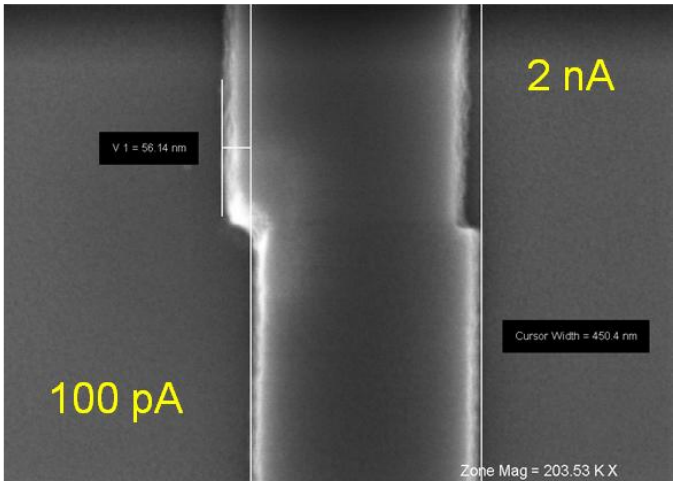

(b)

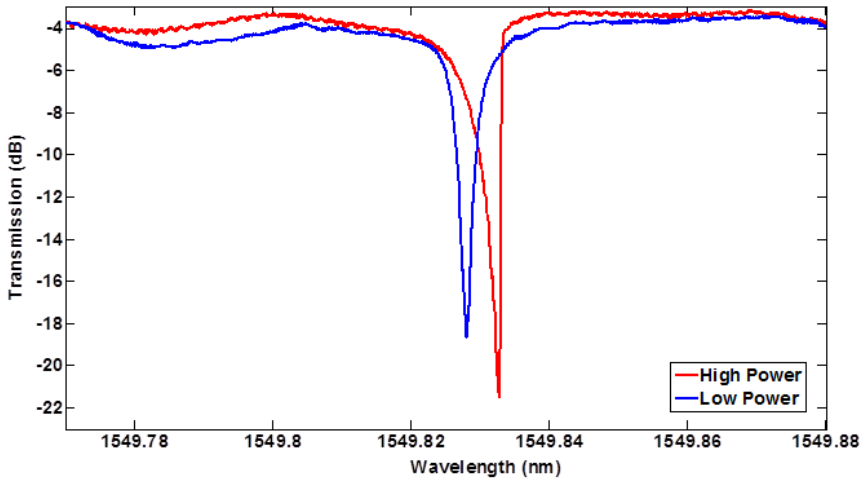

(c)

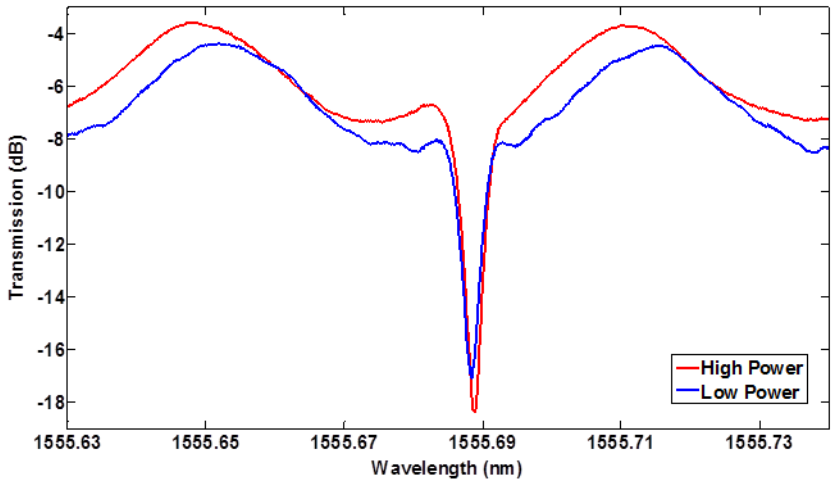

Figure 7.6. (a) SEM showing the transition from patterning with 100 pA EBL to 2 nA. It is clear that sidewall roughness increases with EBL current. 2nd-radial-order mode resonance in a 20-μm-radius microdisk patterned with (b) 2 nA EBL, resulting in Q_i of ~ 700,000, and (c) 100 pA EBL, resulting in Q_i of ~ 1.1 million.

Discontinuities in the transition regions, such as the one seen in Figure 7.6(a), may occur because the EBL machine will likely need recalibration after changing its current. These transitions can be smoothed by using overlapping taper patterns in the CAD input file, such as those shown in Figure 7.7.

(a)

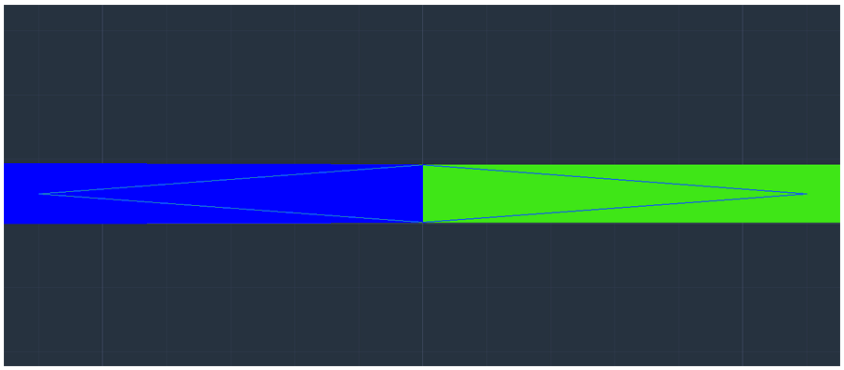

(b)

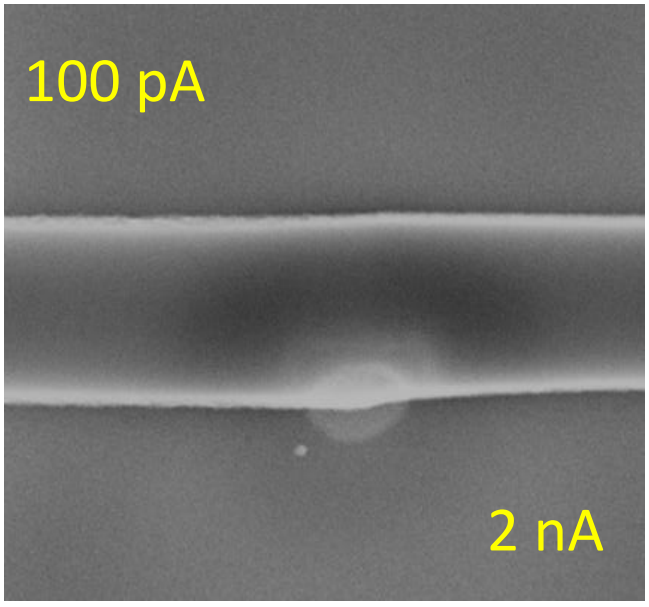

Figure 7.7. (a) AutoCAD pattern with overlapping tapers used for smoothing the transition between regions that are patterned with different EBL currents. (b) Fabrication result using the pattern in part (a).

7.3. Improving the Fiber-to-Waveguide Coupling Efficiency by Using Bosch Process for Creating Plasma-Cleaved Facets

A major source of insertion loss in SOI PLCs is the low coupling efficiency between the input/output fibers and the bus waveguides fabricated on the chip. This low coupling efficiency results from mode-size and effective-index mismatches between the fiber mode and the waveguide mode, which induce coupling to radiation and back-reflection modes [71]. One way of dealing with mode-size mismatch is to taper the waveguide up to fiber dimensions at the input and output facets. However, these inverse tapers still suffer from effective-index mismatch with the fiber, which causes strong back reflections from the facets that lead to unwanted Fabry-Perot effects. In addition, up tapers can significantly increase the write time if the patterning is done with EBL.

Another way of addressing the mode-size mismatch issue is through the use of regular tapers. As the dimensions of the waveguide are reduced, the optical mode gradually becomes delocalized from the Si core, and its effective size increases. Since most of the optical mode in this case will reside in the BOX and oxide cladding layers, its effective index will be very close to that of the silica fiber, which provides the additional benefit of alleviating the effective-index mismatch. The effective mode field diameter (MFD) for the tapered lensed fibers used throughout this work is 2.5 μm. We used the COMSOL 4.3b Wave Optics Module to derive the TE-mode diameter of a 220-nm-thick SOI waveguide with a width varying from 450 nm to 50 nm. The two-dimensional equivalent of Equation (2.15) was used for calculating the mode diameter. The BOX thickness was assumed to be 3 μm, and the oxide cladding thickness to be 1 μm. A minimum width of 50 nm was chosen because it was the lowest width that we could

reliably achieve with the EBL machine. The results of the simulation are shown in Figure 7.8(a). It can be seen that mode diameter increases from 280 nm for a 450-nm-wide waveguide to 1.84 μm for a 50-nm-wide waveguide. The coupling loss resulting from mode-size mismatch can be approximated from [72]

$$L_{Mode\ Size}\left(dB\right) = 20\log\left(\frac{1}{2}\left(\frac{MFD_1}{MFD_2} + \frac{MFD_2}{MFD_1}\right)\right), \tag{7.1}$$

where MFD_1 and MFD_2 are the mode field diameters of the two optical modes, which are assumed to have Gaussian profiles. The results of this calculation are also shown in Figure 7.8(a). As the MFD increases, the coupling loss is reduced from 13.1 dB for the 450-nm-wide waveguide to 0.4 dB for the 50-nm-wide waveguide. The profile of the simulated TE mode for the 50-nm-wide waveguide is shown in Figure 7.8(b).

The loss resulting from back reflection caused by effective index mismatch can be calculated from

$$L_{Effective\ Index}\left(dB\right) = -10\log\left(1 - \left(\frac{\beta_{Fiber} - \beta_{WG}}{\beta_{Fiber} + \beta_{WG}}\right)^2\right), \tag{7.2}$$

which is based on Fresnel equations under normal incidence. This loss ranges from a low of 0.0006 dB per facet for the 50-nm-wide waveguide to a high of 0.24 dB per facet for the 450-nm-wide waveguide. These numbers are much smaller than those resulting from mode-size mismatch, and therefore, are fairly inconsequential in this particular case.

(a)

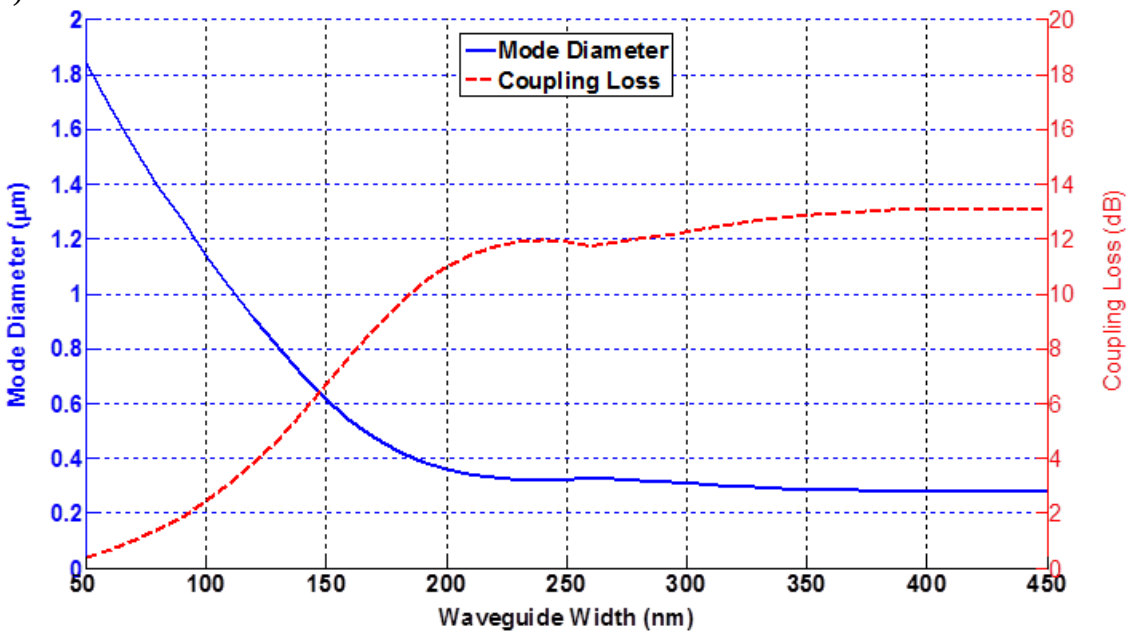

(b)

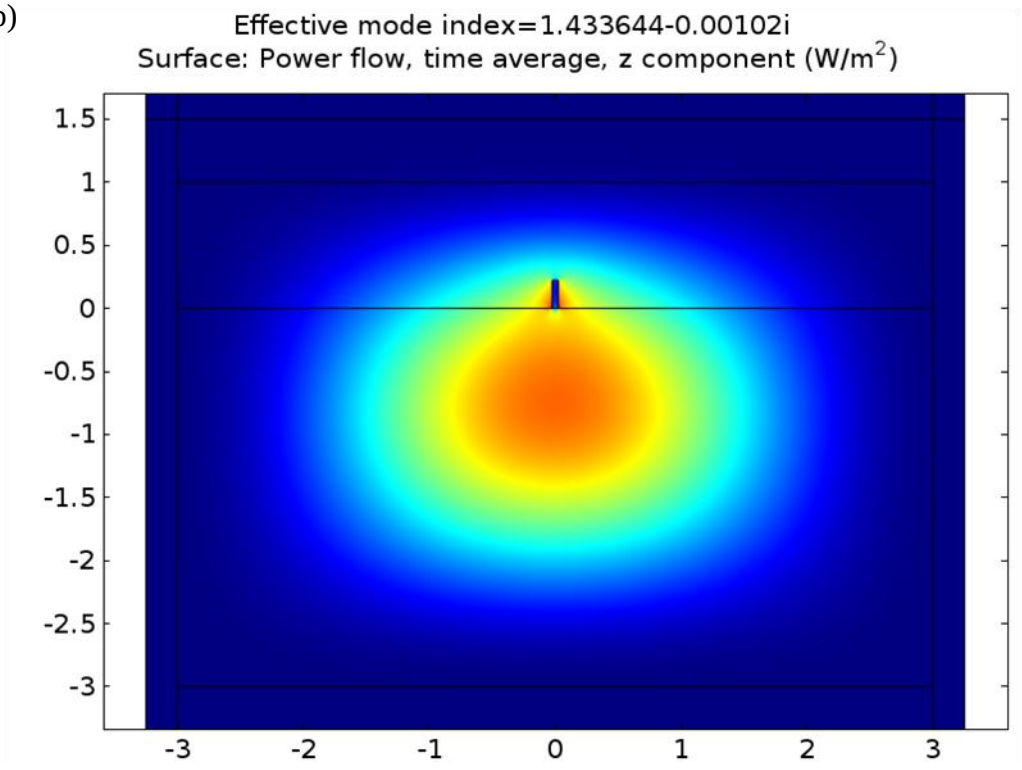

Figure 7.8. (a) Simulation results for mode diameter and mode-size-mismatch fiber-to-waveguide loss as a function of width for a 220-nm-tall SOI waveguide. (b) Poynting-vector profile of the TE mode for a 50×220 nm^2 waveguide with a 1-μm-cladding and 3-μm-BOX.

An important factor to consider when designing tapers, whether regular or inverse, is the tapering length. If this length is too short, there will be too much loss from coupling to radiation modes as a result of tapering. This creates a trade-off in the design of regular tapers since at lower widths, the waveguide itself is highly lossy. Therefore, using a very smooth taper may inadvertently result in high loss. A 40-μm-long taper with a total insertion loss of ~ 6 dB (for the TE mode) was demonstrated in [71].

With taper lengths that are below 500 μm and the mode size changing rapidly over this length, the physical cleaving of input and output facets at the right location can prove to be extremely difficult. To address this problem, we developed a method for creating the input and output facets by plasma etching. A schematic of the desired end result is shown in Figure 7.9(a). The facets need to be etched at the point where the taper has the right mode size. This can be accomplished accurately by using a patterned photoresist as the etch mask. The underlying Si substrate needs to be etched at least as deep as about the radius of the tapered lensed fiber (i.e., 62.5 μm) in order to allow for the fiber to be brought as close as possible to the waveguide facet. The standard process for this type of deep Si etching is the Bosch process. The SiO_2 cladding and BOX layers also need to be etched, which can be done using a process such as C_4F_8. It is preferable that both etching steps are performed with the same mask, and therefore, a relatively thick layer of photoresist must be used the etch mask. In this work, we used the SPR 220-7.0 positive photoresist which can be coated in 8-μm-thick layers with a spin speed of 2000 RPM, has an etch resistance of more than 100 times that of Si in the Bosch process, and a 1:1 resistance to C_4F_8 compared to SiO_2. Therefore, an 8-μm-thick layer of SPR

220-7.0 will more than suffice to etch 4 μm (1 μm cladding + 3 μm BOX) of SiO_2 with C_4F_8, in addition to 100 μm of Si with the Bosch process.

Figure 7.9(b) shows a top-view schematic of the process described above. A set of 4-mm-long waveguides are fabricated on a 220-nm-thick, 3-μm-BOX wafer and covered with a 1-μm-thick PECVD oxide cladding. The fabrication is performed by HSQ-based EBL and Cl_2 plasma etching. Some of these waveguides have a fixed width of 450 nm for their entire lengths. Another group have 200-μm-long, linear tapers from 450 nm to 50 nm at their input and output. There is a distance of ~ 3 μm between the tip of the taper and the cleaving boundary at the input and output, as was done in [71]. There is yet another group with identical tapers but with the cleaving boundary cutting through them at a waveguide width of 80 nm. An 8-μm-thick layer of SPR 220-7.0 is coated on top of the oxide cladding. Optical lithography is then performed to define a photoresist mask that exposes the waveguide tips beyond the cleaving boundary but covers the rest of the device. Plasma etching with C_4F_8 and the Bosch process is performed next, and in the end, the remaining photoresist is removed in the solvent. Figure 7.10 shows two SEMs of the plasma-cleaved edge of the sample. SEMs depicting the plasma-cleaved facets of each aforementioned group of waveguides are shown in Figure 7.11.

Table 7.2 shows the results of our insertion loss measurements for each group of waveguides at the 1.55 μm wavelength. As expected, the best results (16.8 dB reduction in the total insertion loss) are achieved with the 50-nm-wide facets. The per-facet loss numbers are derived after accounting for the 5 dB/cm normal waveguide propagation loss, and therefore include the radiation loss of the tapered waveguides. As a result, they are larger than the numbers derived in Figure 7.8(a), which only included the mode-size

mismatch loss. However, the 1.2 dB increase in loss per facet from 3.7 dB for 50 nm to 4.9 dB for 80 nm is very close to the 1 dB increase that can be expected from Figure 7.8(a). The residual difference can be explained by the fact that the waveguide mode does not have a perfectly Gaussian profile. The difference in losses resulting from effective-index mismatch is below 0.0001 dB per facet.

Figure 7.12 shows the normalized power transmission of the waveguide with 50-nm-wide input and output facets as a function of wavelength. It can be seen that, as expected, the Fabry-Perot effects resulting from back reflection at the facets have been practically eliminated.

Waveguide Width @ Facet (nm)	Total Insertion Loss (dB)	Loss per Facet (dB)
450	26.2	12.1
80	11.8	4.9
50	9.4	3.7

Table 7.2. Insertion loss measurement results for each group of waveguides at 1.55 μm. The per-facet loss numbers are derived after accounting for the 5 dB/cm normal waveguide propagation loss.

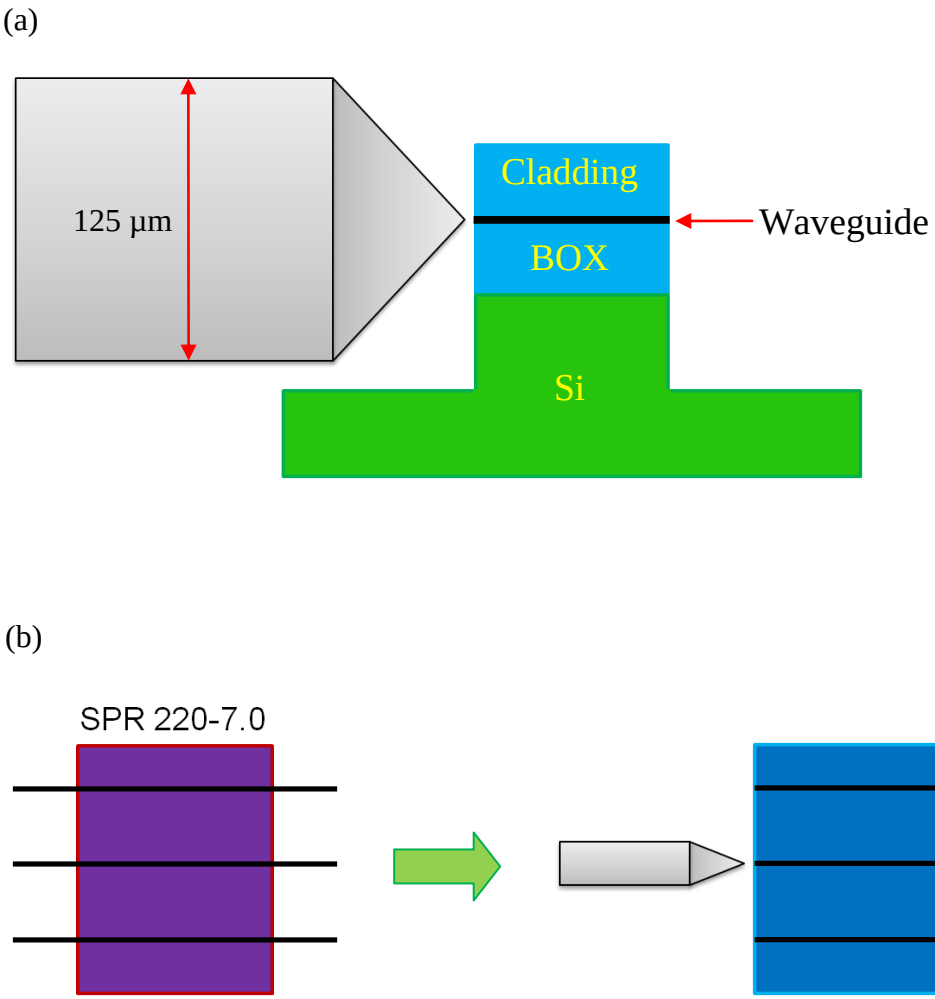

Figure 7.9. (a) Side-view schematic of a plasma-cleaved SOI waveguide coupled to a tapered lensed fiber. (b) Top-view schematic showing the fabrication process that leads to the result depicted in part (a).

(a)

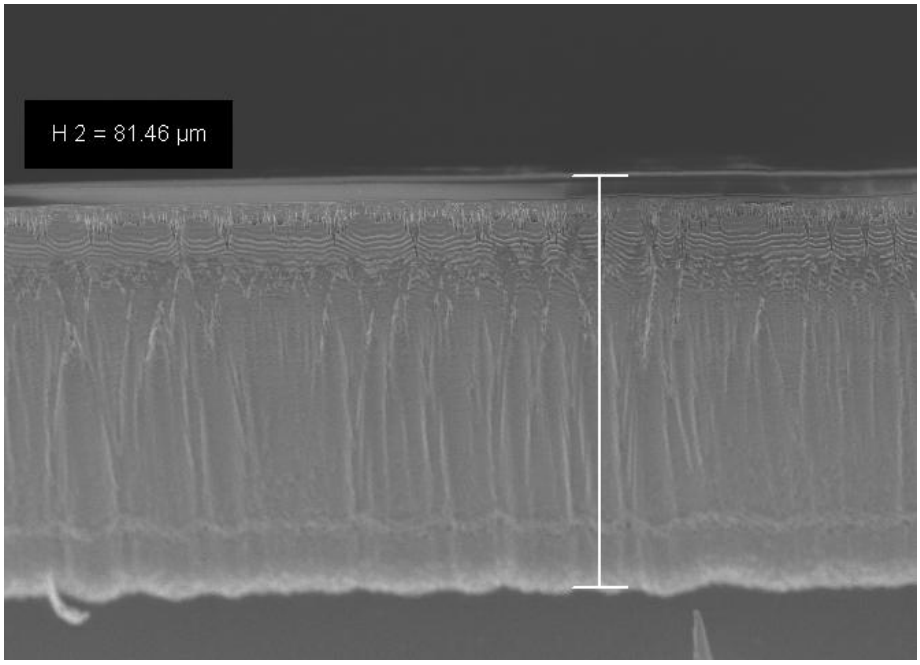

(b)

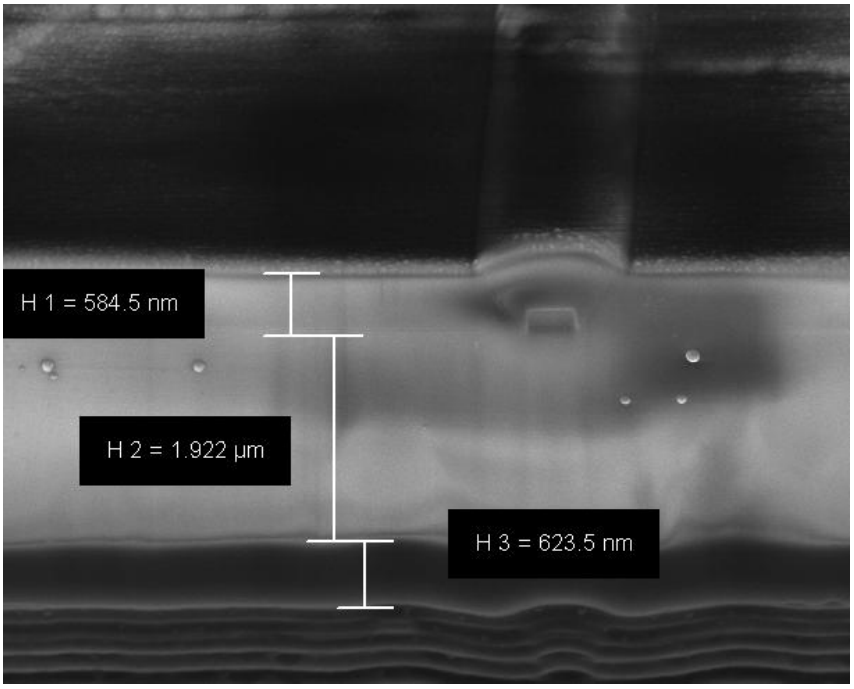

Figure 7.10. (a) Slant (45˚) SEM of the plasma-cleaved edge of the SOI wafer. (b) Close-up slant SEM showing the waveguide facet, cladding and BOX layers that are etched with C_4F_8, and the underlying Si substrate that is etched in the Bosch process.

(a)

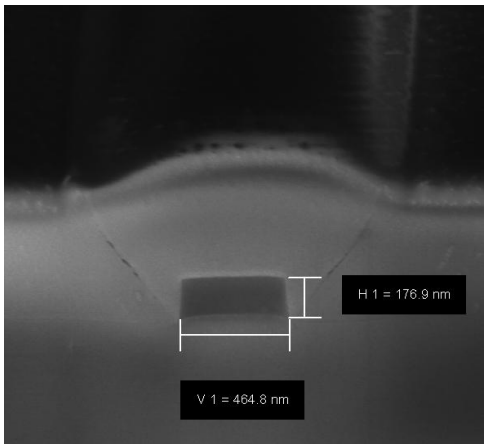

(b)

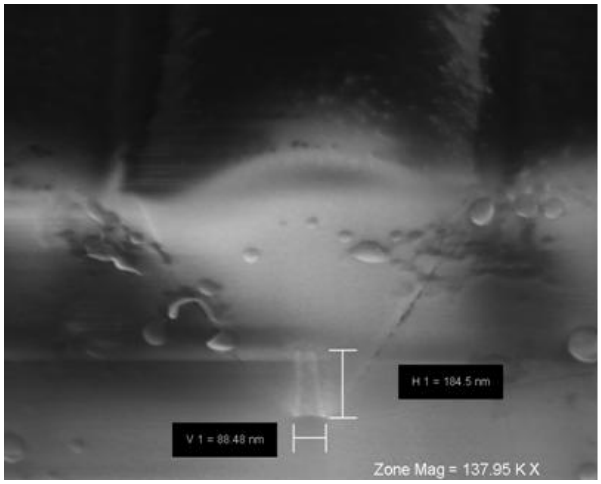

(c)

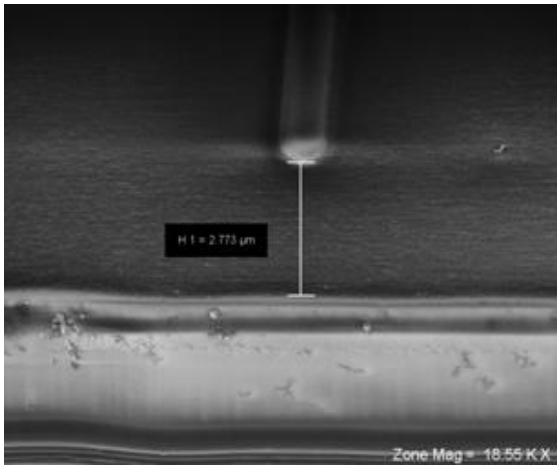

Figure 7.11. Slant (45˚) SEMs of the plasma-cleaved facets of (a) a 450-nm-wide waveguide, (b) a tapered waveguide cleaved at its 80-nm-wide point, (c) a tapered waveguide with a 50-nm-wide tip that is ~ 3 µm away from the edge. Si thickness is 220 nm for all cases.

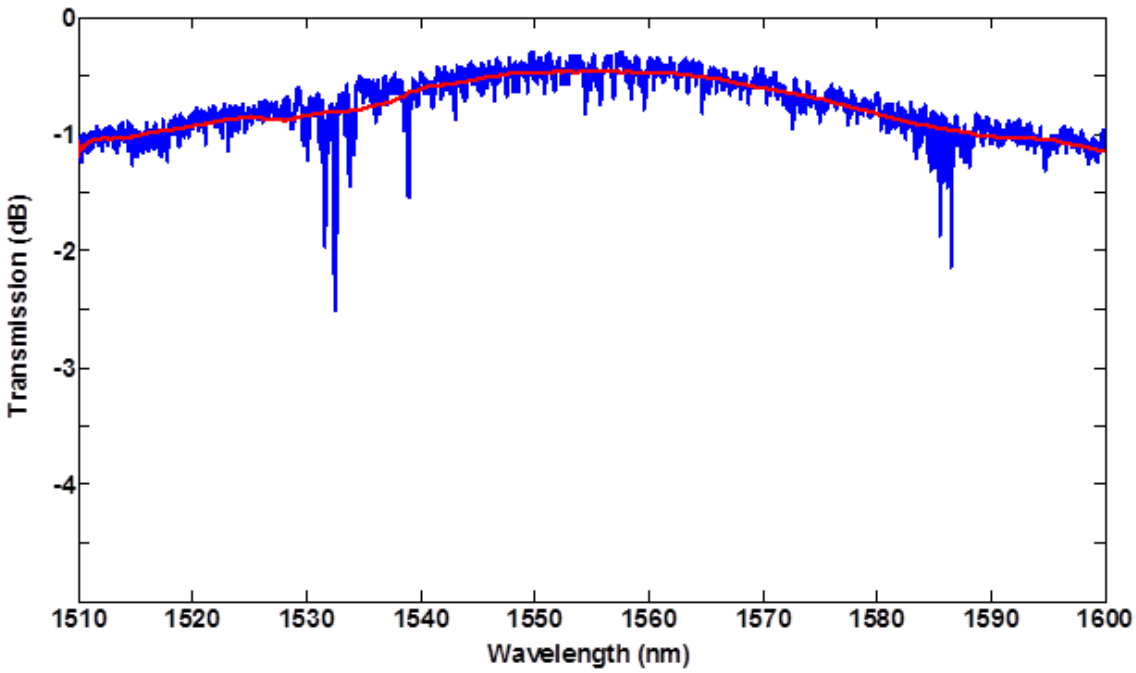

Figure 7.12. Normalized power transmission of the waveguide with 50-nm-wide input and output facets as a function of wavelength. Fabry-Perot effects resulting from back reflection at the facets have been reduced to ~ 0.5 dB. The red curve shows the same data after smoothing.

CHAPTER 8

CONCLUSION AND FUTURE DIRECTIONS

The main thrust of this thesis has been the demonstration of several important optical signal processing and networking functionalities by using thermally reconfigurable integrated photonic devices on SOI, having in mind the ultimate goal of realizing monolithic systems-on-a-chip on the aforementioned platform.

The first of these devices was a fully reconfigurable and ultra-compact filter that can be used for both RF-photonic and purely optical signal processing purposes. We used a filter architecture based on cascading any desired number of two-pole, two-zero unit cells with full control over the placement of poles and zeros. The cascade architecture was used because it is the easiest to design and characterize (since each stage can be designed and calibrated independently), is the least sensitive to fabrication imperfections, and also has the largest out-of-band rejection with minimal sacrifices in terms of the minimum achievable bandwidth. We demonstrated a two-stage (i.e., four-pole, four-zero) filter with a footprint of 0.25 mm^2 and a tunable bandwidth of 0.9–4.3 GHz over an FSR of 650 GHz. Optical out-of-band rejections up to 38 dB were achieved, and both band-pass and band-stop responses were demonstrated. Higher-order filters with more complex responses, higher out-of-band rejections, or narrower bandwidths can be built by cascading a larger number of the demonstrated unit cells.

The second demonstrated device was an adaptive reflection suppressor for feedback elimination that did not rely on non-reciprocal mechanisms such as magneto-optics or nonlinear optics. Feedback elimination can be critical for mitigating spurious

interferences and protecting lasers from disturbance. A reflection suppression ratio of 40 dB was achieved with a device footprint of 105 μm in length. This small footprint, in conjunction with a waveguide propagation loss of 5 dB/cm and the absence of excess loss, results in a total insertion loss below 0.15 dB. The operation bandwidth depends on the frequency dependence of the back reflection going into the suppressor, which is predominantly determined by the distance between the device and the source of reflection. A theoretical study of the resulting distance-bandwidth trade-off was performed, and a 20-dB reflection suppression bandwidth of 20.7 GHz was experimentally demonstrated. While not a true optical isolator in the sense of being a non-reciprocal device with complete unidirectional transmission, this device has nevertheless a better performance than the existing alternatives in terms of suppression ratio, insertion loss, and bandwidth. In addition, it does not require the presence of an external magnetic field, has a relatively straightforward fabrication process, and is not limited to specific power ranges.

The final reconfigurable device demonstrated in this work was a novel on-chip fiber-polarization controller based on a fully reconfigurable (amplitude and phase) 2×2 cell used in conjunction with a pair of two-dimensional grating couplers at the input/output for polarization splitting/combining. The 2×2 cell is capable of receiving two inputs from the polarization splitter and generating a coherent, linear combination of them at a selected output with tunable, complex weighting coefficients. This allows us to realize any desired combination of relative phase and amplitude ratios for the two outputs going into the output grating coupler (polarization combiner). Since any arbitrary elliptical polarization can be described by the relative phase and amplitude ratios of its

two orthogonally polarized components, the combination of the cell's two outputs inside the output fiber can have any desired elliptical polarization. Therefore, the device as a whole can convert any arbitrary input polarization to any desired polarization at the output. This device can be used for the compensation of polarization rotation in fibers for polarization-mode multiplexing systems, as well as on-chip ellipsometry solutions.

We also addressed a range of different challenges that arise in the implementation of SOI devices in general, including the thermal instability of resonators, undesired on-chip polarization-mode conversion, high scattering loss, and high coupling loss.

As for thermal instability resulting from the strong thermo-optic property of Si, the first inherently athermal high-*Q* microdisk resonator on SOI was demonstrated through a combination of mode engineering and using the proper polymer as the cladding material. The passive athermalization approach utilized here is preferable to active temperature stabilization from the angle of minimizing power consumption and complexity. The traditional polymer-based version of this approach has implementation problems resulting from the limited heat resistance of polymers, which inhibits their use in CMOS-compatible fabrication processes. In this dissertation, we also laid the groundwork for CMOS-compatible athermal microresonators on SOI by utilizing, for the first time, the negative TOC of TiO_2 films to reduce the temperature sensitivity of TiO_2-clad Si devices.

Scattering in SOI waveguides can lead to undesired polarization-mode conversion throughout the photonic chip. We studied the potential of metallic films deposited on top of the protective cladding layer to suppress TM propagation by inducing highly disproportionate absorption losses in the TM and TE modes of a standard waveguide, and

concluded that, contrary to intuition, metals with a large imaginary component of the refractive index are not necessarily the best choice for this purpose, and also that increasing the metal thickness does not necessarily result in a higher loss value. A TM propagation loss as high as 250 dB/cm was shown to be achievable with Tungsten, while the TE propagation loss in the same configuration amounted to no more than 0.1 dB/cm.

The high index contrast between Si and its surrounding materials, and the consequent reduction in the optical mode size result in high values for both the scattering loss and the input/output coupling loss for SOI PLCs. We showed that by reducing the level of sidewall roughness, and therefore, reducing the scattering loss, low-current e-beam lithography can improve resonator *Q* factors by at least 60%. We also devised a novel fabrication technique that greatly facilitates the implementation of tapers at the input/output facets, and demonstrated a per-facet coupling loss as low as 3.7 dB (compared with 12.1 dB without tapers).

Finally, below are a list of possible extensions of the work presented in this thesis for the future:

- Improving the quality of deposited TiO_2 films in order to enable the realization of high-*Q* and fully athermal microresonators.
- A full investigation of the relation between deposition parameters and the TOC of the resulting TiO_2 films, with the potential of tailoring the TORS for Si-photonic devices without the need for geometry modification.
- Building up on the work presented in Chapter 4 to realize higher-order filters, as well as performing system demonstrations using the already available devices.

- Cascading multiple units of the reflection suppressor demonstrated in Chapter 5 in order to achieve a wider operation bandwidth.
- Obtaining more data points for a quantitative analysis of the relation between lithography current, sidewall roughness, and resonator *Q*.
- An experimental investigation of the TM-suppression concept presented in Section 7.1.

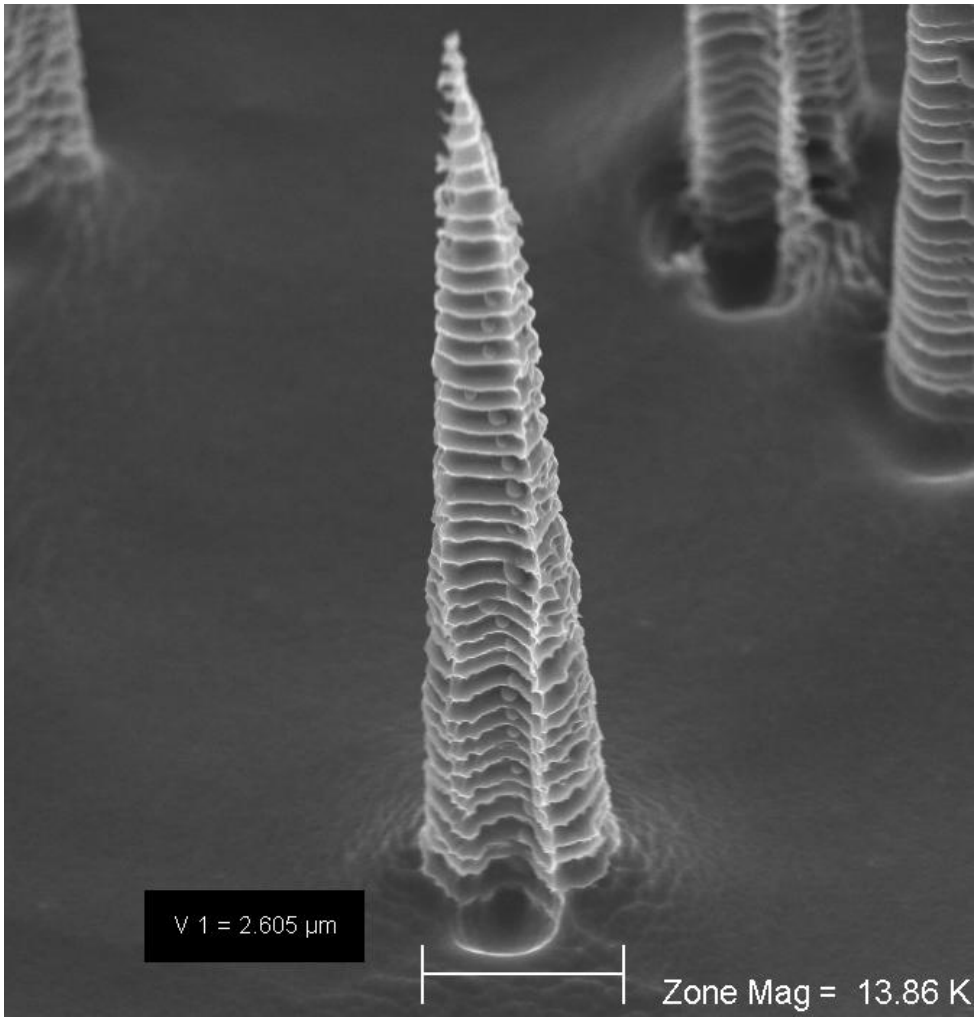

Figure 8.1. “Micro-stalagmite” on a silicon floor, formed during a Bosch process.

REFERENCES

[1] http://en.wikipedia.org/wiki/Moore's_law

[2] D. A. B. Miller, "Rationale and challenges for optical interconnects to electronic chips," Proc. IEEE **88**, 728 (2000).

[3] D. Marpaung, C. Roeloffzen, R. Heideman, A. Leinse, S. Sales, and J. Capmany, "Integrated microwave photonics," Laser Photon. Rev. **7**, 506 (2013).

[4] B. Little, S. Chu, P. Absil, J. Hryniewicz, F. Johnson, F. Seiferth, D. Gill, V. Van, O. King, and M. Trakalo, "Very high-order microring resonator filters for WDM applications," IEEE Photon. Tech. Lett. **16**, 2263 (2004).

[5] G. T. Reed and A. P. Knights, *Silicon Photonics: An Introduction* (Wiley, 2004).

[6] R. A. Soref, "The past, present, and future of silicon photonics," IEEE J. Sel. Top. Quantum Electron. **12**, 1678 (2006).

[7] Y. Okawachi, K. Saha, J. S. Levy, Y. H. Wen, M. Lipson, and A. L. Gaeta, "Octave-spanning frequency comb generation in a silicon nitride chip, " Opt. Lett. **36**, 3398 (2011).

[8] M. Masanovic, V. Lal, J. Summers, J. Barton, E. Skogen, L. Rau, L. Coldren, and D. Blumenthal, "Widely tunable monolithically integrated all-optical wavelength converters in InP," J. Lightwave Technol. **23**, 1350 (2005).

[9] T. Barwicz and H. Haus, "Three-dimensional analysis of scattering losses due to sidewall roughness in microphotonic waveguides," J. Lightwave Technol. **23**, 2719 (2005).

[10] http://newsroom.intel.com/docs/DOC-2032

[11] K. K. Lee, D. R. Lim, L. C. Kimerling, J. Shin, and F. Cerrina, "Fabrication of ultralow-loss Si/SiO_2 waveguides by roughness reduction," Opt. Lett. **26**, 1888 (2001).

[12] M. Borselli, T. J. Johnson, and O. Painter, "Beyond the Rayleigh scattering limit in high-*Q* silicon microdisks: theory and experiment," Opt. Express **13**, 1515 (2005).

[13] J. Cardenas, C. B. Poitras, J. T. Robinson, K. Preston, L. Chen, and M. Lipson, "Low loss etchless silicon photonic waveguides," Opt. Express **17**, 4752 (2009).

[14] A. W. Fang, H. Park, R. Jones, O. Cohen, M. J. Paniccia, and J. E. Bowers, "A continuous-wave hybrid AlGaInAs-silicon evanescent laser," IEEE Photon. Tech. Lett. **18**, 1143 (2006).

[15] R. A. Soref and B. R. Bennett, "Electrooptical effects in silicon," IEEE J. Quantum Electron. **23**, 123 (1987).

[16] G. Gosh, *Handbook of Thermo-Optic Coefficients of Optical Materials with Applications* (Academic Press, 1998).

[17] Q. Xu, B. Schmidt, S. Pradhan, and M. Lipson, "Micrometre-scale silicon electro-optic modulator," Nature **435**, 325 (2005).

[18] A. Liu, L. Liao, D. Rubin, H. Nguyen, B. Ciftcioglu, Y. Chetrit, N. Izhaky, and M. J. Paniccia, "High-speed optical modulation based on carrier depletion in a silicon waveguide," Opt. Express **15**, 660 (2007).

[19] B. G. Lee, A. Biberman, N. Sherwood-Droz, C. B. Poitras, M. Lipson, and K. Bergman, "High-speed 2×2 switch for multiwavelength silicon-photonic networks–on-chip," J. Lightwave Technol. **27**, 2900 (2009).

[20] A. Liu, L. Liao, D. Rubin, J. Basak, Y. Chetrit, H. Nguyen, R. Cohen, N. Izhaky, and M. J. Paniccia, "Recent development in a high-speed silicon optical modulator based on reverse-biased pn diode in a silicon waveguide," Semicond. Sci. Technol. **23**, 064001 (2008).

[21] A. H. Atabaki, A. A. Eftekhar, S. Yegnanarayanan, and A. Adibi, "Sub-100-nanosecond thermal reconfiguration of silicon photonic devices," Opt. Express **21**, 15706 (2013).

[22] H. Rong, R. Jones, A. Liu, O. Cohen, D. Hak, A. W. Fang, and M. J. Paniccia, "A continuous-wave Raman silicon laser," Nature **433**, 725 (2005).

[23] L. Vivien, J. Osmond, J.-M. Fedeli, D. Marris-Morini, P. Crozat, J.-F. Damlencourt, E. Cassan, Y. Lecunff, and S. Laval, "42 GHz p.i.n Germanium photodetector integrated in a silicon-on-insulator waveguide," Opt. Express **17**, 6252 (2009).

[24] L. Schares, J. A. Kash, F. E. Doany, C. L. Schow, C. Schuster, D. M. Kuchta, P. K. Pepeljugoski, J. M. Trewhella, C. W. Baks, R. A. John, L. Shan, Y. H. Kwark, R. A. Budd, P. Chiniwalla, F. R. Libsch, J. Rosner, C. K. Tsang, C. S. Patel, J. D. Schaub, R. Dangel, F. Horst, B. J. Offrein, D. Kucharski, D. Guckenberger, S. Hegde, H. Nyikal, C.-K. Lin, A. Tandon, G. R. Trott, M. Nystrom, D. P. Bour, M. R. T. Tan, and D. W. Dolfi, "Terabus: Terabit/second-class card-level optical interconnect technologies," IEEE J. Sel. Top. Quantum Electron. **12**, 1032 (2006).

[25] A. Shacham, K. Bergman, and L. P. Carloni, "Photonic networks-on-chip for future generations of chip multiprocessors," IEEE Trans. Comput. **57**, 1246 (2008).

[26] P. Alipour, E. Shah Hosseini, A. A. Eftekhar, B. Momeni, and A. Adibi, "Athermal performance in high-Q polymer-clad silicon microdisk resonators," Opt. Lett. **35**, 3462 (2010).

[27] P. Alipour, A. A. Eftekhar, A. H. Atabaki, Q. Li, S. Yegnanarayanan, C. K. Madsen, and A. Adibi, "Fully reconfigurable compact RF photonic filters using high-Q silicon microdisk resonators," Opt. Express **19**, 15899 (2011).

[28] H. Kogelnik, "Theory of optical waveguides," in *Guided-wave optoelectronics*, T. Tamir, ed., (Springer-Verlag, 1988), pp. 7–88.

[29] M. Soltani, S. Yegnanarayanan, and A. Adibi, "Ultra-high *Q* planar silicon microdisk resonators for chip-scale silicon photonics," Opt. Express **15**, 4694 (2007).

[30] S. Xiao, M. H. Khan, H. Shen, and M. Qi, "Compact silicon microring resonators with ultra-low propagation loss in the C band," Opt. Express **15**, 14467-14475 (2007).

[31] S. Manipatruni, R. K. Dokania, B. Schmidt, N. Sherwood-Droz, C. B. Poitras, A. B. Apsel, and M. Lipson, "Wide temperature range operation of micrometer-scale silicon electro-optic modulators," Opt. Lett. **33**, 2185 (2008).

[32] Z. Zhang, P. Zhao, P. Lin, and F. Sun, "Thermo-optic coefficients of polymers for optical waveguide applications," Polymer **47**, 4893 (2006).

[33] Y. Kokuban, N. Funato, and M. Takizawa, "Athermal waveguides for temperature-independent lightwave devices," IEEE Photon. Tech. Lett. **5**, 1297 (1993).

[34] J. M. Lee, D. J. Kim, H. Ahn, S. H. Park, and G. Kim, "Temperature dependence of silicon nanophotonic ring resonator with a polymeric overlayer," J. Lightwave Technol. **25**, 2236 (2007).

[35] W. N. Ye, J. Michel, and L. C. Kimerling, "Athermal high-index-contrast waveguide design," IEEE Photon. Tech. Lett. **20**, 885 (2008).

[36] J. Teng, P. Dumon, W. Bogaerts, H. Zhang, X. Jian, X. Han, M. Zhao, G. Morthier, and R. Baets, "Athermal silicon-on-insulator ring resonators by overlaying a polymer cladding on narrowed waveguides," Opt. Express **17**, 14627 (2009).

[37] V. Raghunathan, W. N. Ye, J. Hu, T. Izuhara, J. Michel, and L. C. Kimerling, "Athermal operation of Silicon waveguides: spectral, second order and footprint dependencies," Opt. Express **18**, 17631-17639 (2010).

[38] G. Gulsen and M. Naci Inci, "Thermal optical properties of TiO_2 films," Opt. Mater. **18**, 373 (2002).

[39] H. Xie, F. L. Ng, and X. T. Zeng, "Spectroscopic ellipsometry study of thin film thermo-optical properties," Thin Solid Films **517**, 5066-5069 (2009).

[40] M. R. Saleem, R. Ali, S. Honkanen, and J. Turunen, "Thermal properties of thin Al_2O_3 films and their barrier layer effect on thermo-optic properties of TiO_2 films grown by atomic layer deposition," Thin Solid Films, Available online 21 June 2013, http://dx.doi.org/10.1016/j.tsf.2013.06.030.

[41] N. Martin, C. Rousselot, D. Rondot, F. Palmino, and R. Mercier, "Microstructure modification of amorphous titanium oxide thin films during annealing treatment," Thin Solid Films **300**, 113-121 (1997).

[42] V. Mikhelashvili and G. Eisenstein, "Effects of annealing conditions on optical and electrical characteristics of titanium dioxide films deposited by electron beam evaporation," J. Appl. Phys. **89**, 3256-3269 (2001).

[43] T. Alasaarela, T. Saastamoinen, J. Hiltunen, A. Säynätjoki, A. Tervonen, P. Stenberg, M. Kuittinen, and S. Honkanen, "Atomic layer deposited titanium dioxide

and its application in resonant waveguide grating," Appl. Optics **49**, 4321-4325 (2010).

[44] G. C. Valley, "Photonic analog-to-digital converters," Opt. Express **15**, 1955 (2007).

[45] J. Kim, M. J. Park, M. H. Perrott, and F. X. Kärtner, "Photonic subsampling analog-to-digital conversion of microwave signals at 40-GHz with higher than 7-ENOB resolution," Opt. Express **16**, 16509-16515 (2008).

[46] M. S. Rasras, K.-Y. Tu, D. M. Gill, Y.-K. Chen, A. E. White, S. S. Patel, A. Pomerene, D. Carothers, J. Beattie, M. Beals, J. Michel, and L. C. Kimerling, "Demonstration of a tunable microwave-photonic notch filter using low-loss silicon ring resonators," J. Lightwave Technol. **27**, 2105 (2009).

[47] S. S. Djordjevic, L. W. Luo, S. Ibrahim, N. K. Fontaine, C. B. Poitras, B. Guan, L. Zhou, K. Okamoto, Z. Ding, M. Lipson, and S. J. B. Yoo, "Fully reconfigurable silicon photonic lattice filters with four cascaded unit cells," IEEE Photon. Tech. Lett. **23**, 42 (2011).

[48] E.J. Norberg, R.S. Guzzon, S.C. Nicholes, J.S. Parker, and L.A. Coldren, "Programmable photonic lattice filters in InGaAsP/InP," IEEE Photon. Tech. Lett. **22**, 109 (2010).

[49] R. Patnaik, V. Vandrasi , C. K. Madsen, A. A. Eftekhar, and A. Adibi, "Comparison of cascade, lattice, and parallel filter architectures," J. Lightwave Technol. **28**, 3463 (2010).

[50] A. H. Atabaki, E. Shah Hosseini, A. A. Eftekhar, S. Yegnanarayanan, and A. Adibi, "Optimization of metallic microheaters for high-speed reconfigurable silicon photonics," Opt. Express **18**, 18312 (2010).

[51] S. Yegnanarayanan, P. D. Trinh, F. Coppinger, and B. Jalali, "Compact silicon-based integrated optic time delays," IEEE Photon. Tech. Lett. **9**, 634 (1997).

[52] U. Fischer, T. Zinke, J.-R. Kropp, F. Arndt, and K. Petermann, "0.1 dB/cm waveguide loss in single-mode SOI rib waveguides," IEEE Photon. Tech. Lett. **8**, 647 (1996).

[53] Q. Li, A. A. Eftekhar, P. Alipour, A. H. Atabaki, S. Yegnanarayanan, and A. Adibi, "Low-loss microdisk-based delay lines for narrowband optical filters," IEEE Photon. Tech. Lett. **24**, 1276 (2012).

[54] E. Shah Hosseini, S. Yegnanarayanan, A. H. Atabaki, M. Soltani, and A. Adibi, "Systematic design and fabrication of high-*Q* single-mode pulley-coupled planar silicon nitride microdisk resonators at visible wavelengths," Opt. Express **18**, 2127 (2010).

[55] C. W. Holzwarth, T. Barwicz, and H. I. Smith, "Optimization of hydrogen silsesquioxane for photonic applications," J. Vac. Sci. Technol. B **25**, 2658 (2007).

[56] P. Dong, W. Qian, H. Liang, R. Shafiiha, N.-N. Feng, D. Feng, X. Zheng, A. V. Krishnamoorthy, and M. Asghari, "Low power and compact reconfigurable multiplexing devices based on silicon microring resonators," Opt. Express **18**, 9852 (2010).

[57] T. Shintaku, "Integrated optical isolator based on efficient nonreciprocal radiation mode conversion," Appl. Phys. Lett. **73**, 1946 (1998).

[58] J. Fujita, M. Levy, R. M. Osgood, Jr., L. Wilkens, and H. Dotsch, "Waveguide optical isolator based on Mach-Zehnder interferometer," Appl. Phys. Lett. **76**, 2158 (2000).

[59] L. Bi, J. Hu, P. Jiang, D. H. Kim, G. F. Dionne, L. C. Kimerling, and C. A. Ross, "On-chip optical isolation in monolithically integrated non-reciprocal optical resonators," Nat. Photon. **5**, 758 (2011).

[60] M. Tien, T. Mizumoto, P. Pintus, H. Kromer, and J. E. Bowers, "Silicon ring isolators with bonded nonreciprocal magneto-optical garnets," Opt. Express **19**, 11740 (2011).

[61] L. Fan, J. Wang, L. T. Varghese, H. Shen, B. Niu, Y. Xuan, A. M. Weiner, and M. Qi, "An all-silicon passive optical diode," Science **335**, 447 (2012).

[62] S. K. Ibrahim, S. Bhandare, D. Sandel, H. Zhang, and R. Noe, "Non-magnetic 30 dB integrated optical isolator in III/V material," Electron. Lett. **40**, 1293 (2004).

[63] D. Jalas, A. Petrov, M. Eich, W. Freude, S. Fan, Z. Yu, R. Baets, M. Popovic, A. Melloni, J. D. Joannopoulos, M. Vanwolleghem, C. R. Doerr, and H. Renner, "What is — and what is not — an optical isolator," Nat. Photon. **7**, 579 (2013).

[64] W. Bogaerts, D. Taillaert, P. Dumon, D. Van Thourhout, R. Baets, and E. Pluk, "A polarization-diversity wavelength duplexer circuit in silicon-on-insulator photonic wires," Opt. Express **15**, 1567 (2007).

[65] G. S. Smith, *An Introduction to Classical Electromagnetic Radiation* (Cambridge University Press, 1997).

[66] D. Taillaert, H. Chong, P. Borel, L. Frandsen, R. De La Rue, and R. Baets, "A compact two-dimensional grating coupler used as a polarization splitter," IEEE Photon Technol. Lett. **15**, 1249 (2003).

[67] M. Antelius, K. Gylfason, and H. Sohlström, "An apodized SOI waveguide-to-fiber surface grating coupler for single lithography silicon photonics," Opt. Express **19**, 3592 (2011).

[68] http://www.luxpop.com/

[69] http://refractiveindex.info/

[70] R. J. Bojko, J. Li, L. He, T. Baehr-Jones, M. Hochberg, and Y. Aida, "Electron beam lithography writing strategies for low loss, high confinement silicon optical waveguides," J. Vac. Sci. Technol. B **29**, 06F309 (2011).

[71] V. R. Almeida, R. R. Panepucci, and M. Lipson, "Nanotaper for compact mode conversion," Opt. Lett. **28**, 1302 (2003).

[72] S. Yuan and N. A. Riza, "General formula for coupling-loss characterization of single-mode fiber collimators by use of gradient-index rod lenses," Appl. Opt. **38**, 3214 (1999).